Charles University in Prague

Faculty of Mathematics and Physics

DOCTORAL THESIS

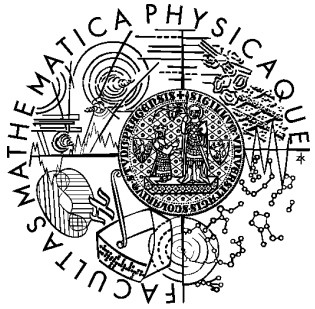

Peter Cendula

Theoretical studies of rolled-up and wrinkled nanomembranes

Department of Condensed Matter Physics

Supervisors: Prof. Dr. Oliver G. Schmidt

Prof. RNDr. Václav Holý, CSc.

Graduate programme: Physics of nanostructures

Graduate school: Physics

Prague 2011

I declare that I carried out this doctoral thesis independently, and only with the cited sources, literature and other professional sources. I understand that my work relates to the rights and obligations under the Act No.121-2000 Coll., the Copyright Act, as amended, in particular the fact that the Charles University in Prague has the right to conclude a license agreement on the use of this work as a school work pursuant to Section 60 paragraph 1 of the Copyright Act.

Prague ..... Signature .....

Názov práce: Teoretické štúdie rolovaných a zvlnených nanomembrán

Autor: Mgr. Peter Cendula

Katedra: Katedra fyziky kondenzovaných látok

Vedúci dizertačnej práce: Prof. Dr. Oliver G. Schmidt, Prof. RNDr. Václav Holý, CSc.

Abstrakt: Táto dizertačná práca sa zaoberá tromi blízkymi témami z oblasti rolovaných a zvlnených nanomembrán. Najprv zhrnieme klasické poznatky z mechanickej teórie tenkých dosiek, ktoré budeme používať pri popise nanomembrán. V prvej časti študujeme relaxáciu vnútorného napätia membrány po jej uvoľnení od substrátu pomocou odleptania pomocnej medzivrstvy. Súperenie medzi rolovaním do trubičky alebo zvlnením je kvalitatívne vysvetlené energetickou úvahou. Podobný model je použitý aj na určenie maximálneho počtu otáčok rolovanej trubičky. V druhej časti teoreticky a experimentálne ukážeme ako rolovanie zvlnenej obdĺžnikovej vrstvy zvýhodňuje formovanie trubičiek na plochej hrane zvlnenej vrstvy. To umožňuje precíznu kontrolu pozície trubičky na substráte. V tretej časti študujeme rozdelenie energie optického prechodu kvantovej jamy pozdĺž zvlnenej membrány ako následok meniacej sa ohybovej deformácie. Tento efekt môže byť vhodný pre optické detektory a žiariče citlivé na deformáciu. Dôsledkom ohybovej deformácie je tiež lokalizácia stavu elektrónu a diery v rôznych miestach pozdĺž membrány.

Kĺúčové slová: rolovanie, nanotrubička, ohyb, vlnka, nanomembrána, kvantová jama

Title: Theoretical studies of rolled-up and wrinkled nanomembranes

Author: Mgr. Peter Cendula

Department: Department of Condensed Matter Physics

Thesis Supervisors: Prof. Dr. Oliver G. Schmidt, Prof. RNDr. Václav Holý, CSc.

Abstract : The thesis is devoted to three similar topics from the field of rolled-up and wrinkled nanomembranes. We start by recalling classical theory of thin plates, which will be used to describe deformation of nanomembranes. In the first topic, relaxation of internal strain is studied when a flat film is partially released from the substrate by etching the sacrificial layer underneath. Energetic competition of the tube and wrinkle shape is quantitatively investigated. Similar model is used to investigate the limiting maximum value of tube rotations. In the second topic, roll-up of initially wrinkled film is shown to favor tubes forming on the flat edge of rectangular wrinkled pattern, enabling precise control of tube position. Experiment is provided to justify our theoretical predictions. In the third topic, quantum well is assumed inside a wrinkled nanomembrane. Shift of transition energy induced by lateral modulation due to bending strain is quantified, being of interest for strain-sensitive optical detectors and emitters. In addition, lateral localization of electron and hole due to strain is also studied.

Keywords: rolled-up, nanotube, bending, wrinkling, nanomembrane, quantum well

Contents

Introduction

Thin films are cornerstone of modern microelectronic and photonic products. Interconnect layers in computer chips are from conducting films and electrical insulation is provided by dielectric films. Strained silicon provides higher mobility of carriers and thus faster transistor switching. Current integrated circuits are mainly planar, contrary to most macroscale objects and devices which are three-dimensional (3D). The reason stems from the fact that formation of 3D micro- and nanostructures is very demanding in terms of conventional optical lithography, micromilling or electron beam lithography [1]. Therefore, formation of 3D microstructures from two-dimensional (2D) layers has been intensively studied in the last two decades [2, 3].

When looking at the nature, different kinds of self-assembly seem to be the best solution for 3D fabrication. One of them is self-folding of layers caused by various driving forces, i.e. thermal expansion, capillary forces, electric and magnetic actuation [3]. Self-folding into 3D structures is more a bottom-up approach and it is advantageous over the top-down approaches in terms of speed, cost and parallel fabrication.

Since self-folding uses deformation of thin 2D layers (plates), theory of plates has also revived recently [4]. Buckling is often used to produce 3D structures [5] and large deformations of the structures are common [6, 7]. The equilibrium shape of structures can be diverse - tube [8, 6], ring [9], helix [8], wrinkle [10, 7] and toroid [11], to name a few. Understanding and control of parameters which lead to various structures and strain distribution inside the structures is of utmost importance.

In this thesis, we focus on three similar but standalone topics from the field of rolled-up and wrinkled nanomembranes, which are both 3D structures. Every chapter will be motivated, introduced, and concluded separately.

In the first chapter, we review theory of plates under small and large deformation, which will be used in all subsequent chapters. Basic properties of bending and stretching strains are explained. Mechanical equilibrium of plate is formulated in terms of minimum of elastic energy of Föppl-von Kármán equations.

In the second chapter, we study the competition of the rolled-up tube and wrinkle

shape for the initial relaxation of free-hanging flat films. Preferable shape is determined by comparing their elastic energy. We also investigate the maximum number of rotations, which a rolled-up can tube ultimately perform.

In the third chapter, roll-up of initially wrinkled film instead of flat film is studied. By calculating the elastic energy during release of wrinkled film, it is shown that tubes forming on the flat edge of rectangular wrinkled pattern are favored over tubes formed on wrinkled edge of the pattern. Precise control of tube position on the pattern is therefore enabled. Experiment is provided to qualitatively justify our theoretical predictions.

In the fourth chapter, a wrinkled nanomembrane with embedded quantum well is investigated. Due to the alternating bending strain along the nanomembrane, large lateral modulation of the optical transition energy was found. Lateral strain modulation also creates lateral potential wells in different region for electrons and holes, causing decreasing overlap of their wave functions.

Chapter 1

Review of plate theory

From the historical viewpoint, the name "plate" is common in the mechanical engineering community since 1900's. The thin plate refers to a structure, whose thickness d is much thinner compared to its other dimensions L_x and L_y, Fig. 1.1(a). In the microelectronics community, the equivalent term "thin film" is used for the plate. Still recently, the term "nanomembrane" emerged in connection with ability to curl and shape by internal strains. Thus, we will interchangeably use the terms film and nanomembrane in this thesis. We use continuum approximation of the thin film, which is typically valid for films thicker than few atomic layers. The film is assumed to be isotropic and elastic with Young's modulus Y and Poisson's ratio ν, without non-reversible plastic deformation. Basic sources of this section are books of Landau and Lifshitz [12] or Audoly and Pomeau [4].

1.1 Small deflections

Small deflection of thin film is such that the out-of-plane film deflection $\zeta(x, y)$ is small compared to film thickness d. For bending of the film in x direction only, the film is compressed on one surface and stretched at the other surface with linear dependence as we go through the film thickness. The plane in the film with neither compression nor tension is called a neutral plane of the film, Fig. 1.1(b).

For general deflection $\zeta(x, y)$, the bending strain is defined as [12]

$$\varepsilon^b_{xx} = -(z - z_b)\,\kappa_{xx},\ \varepsilon^b_{yy} = -(z - z_b)\,\kappa_{yy},\ \varepsilon^b_{xy} = -(z - z_b)\,\kappa_{xy}, \tag{1.1}$$

where z is the coordinate along the film thickness with origin at the bottom surface of

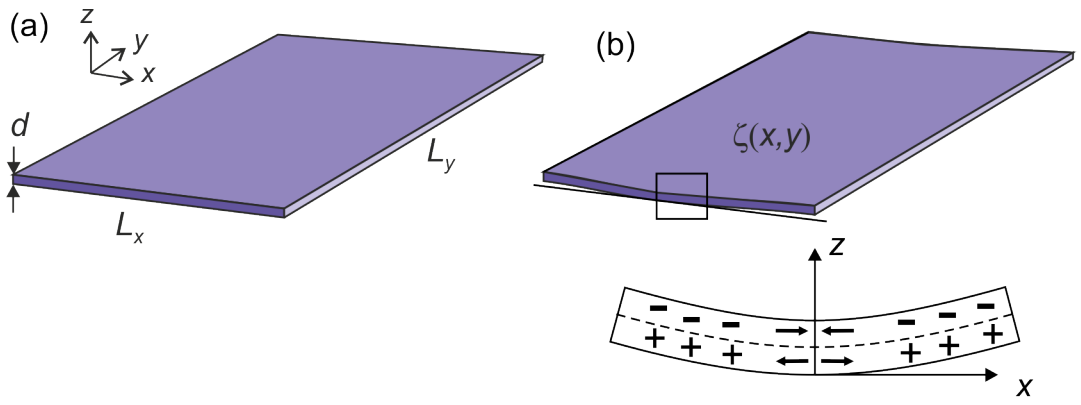

Figure 1.1: (a) Sketch of the flat thin film with thickness d, dimensions L_x, L_y and coordinate system (x, y, z). (b) Small out-of-plane deflection $\zeta(x, y) \ll d$ of the film (top), with deflection enlarged with respect to thickness for good visibility. Close-up of the square region (bottom) with neutral plane (dashed) and compressive (< 0, top layer) or tensile (> 0, bottom layer) bending strains.

the membrane, z_b is position of (mechanical) neutral plane of the membrane during small bending and

$$\kappa_{xx} = \frac{\partial^2 \zeta}{\partial x^2},\ \kappa_{yy} = \frac{\partial^2 \zeta}{\partial y^2},\ \kappa_{xy} = \frac{\partial^2 \zeta}{\partial x \partial y} \tag{1.2}$$

are local curvatures of the film. We will call the surface convex (concave) at certain point, when its curvature is positive (negative). For films with i layers with thicknesses d_i stacked on top of each other, the position of neutral plane is given by [13]

$$z_b = \frac{\sum_{i=1} \overline{Y}_i d_i \left(z_{i+1} + z_i\right)}{2 \sum_{i=1} \overline{Y}_i d_i}, \tag{1.3}$$

$$z_1 = 0,\ z_2 = d_1,\ z_3 = d_1 + d_2,\ z_4 = d_1 + d_2 + d_3, \ldots. \tag{1.4}$$

The plane strain Young's modulus is denoted by

$$\overline{Y}_i = \frac{Y_i}{1 - \nu_i^2}. \tag{1.5}$$

Since the layers are thin, the transverse stress through film thickness has to be zero ($\sigma_{zz} = 0$) at equilibrium [12], implying by Hooke's law for the transverse strain

$$\varepsilon_{zz} = -\frac{\nu}{1 - \nu} \left(\varepsilon_{xx} + \varepsilon_{yy}\right), \tag{1.6}$$

and the volumetric strain (the relative variation of the volume) is

$$\varepsilon_{vol} = \frac{1-2\nu}{1-\nu}\left(\varepsilon_{xx}+\varepsilon_{yy}\right). \tag{1.7}$$

Total elastic energy for bending of the film is computed by integrating over film area

$$U_b = \frac{D}{2}\int\int\left[\left(\kappa_{xx}+\kappa_{yy}\right)^2 + 2\left(1-\nu\right)\left(\kappa_{xy}^2-\kappa_{xx}\kappa_{yy}\right)\right]\mathrm{d}x\mathrm{d}y, \tag{1.8}$$

where integral through thickness was already performed and bending rigidity of the film is denoted

$$D = \frac{Yd^3}{12\left(1-\nu^2\right)}. \tag{1.9}$$

When there are no external forces normal to film surface, mechanical equilibrium is usually found by minimizing the elastic energy of the plate eq. (1.8), which results in equation [12]

$$D\Delta^2\zeta = 0, \tag{1.10}$$

where Δ denotes Laplacian operator in two dimensions x and y

$$\Delta = \frac{\partial^2}{\partial x^2}+\frac{\partial^2}{\partial y^2}. \tag{1.11}$$

For the case of initial biaxial stress σ_0 in the plate ($<$0 for compression), the mechanical equilibrium is expressed by equation [14]

$$D\Delta^2\zeta - d\sigma_0\Delta\zeta = 0. \tag{1.12}$$

1.2 Large deflections

For large out-of-plane displacement $\zeta > d$, Fig. 1.2, correction to the curvature in bending strain has to be applied when we retain the original coordinate system (x, y, z) (since the actual curvature is defined through the arclength [15, 4])

$$\kappa_{xx} = \frac{\partial^2\zeta}{\partial x^2}\frac{1}{\left(1+\left(\frac{\partial\zeta}{\partial x}\right)^2\right)^{3/2}},\ \kappa_{yy} = \frac{\partial^2\zeta}{\partial y^2}\frac{1}{\left(1+\left(\frac{\partial\zeta}{\partial y}\right)^2\right)^{3/2}}, \tag{1.13}$$

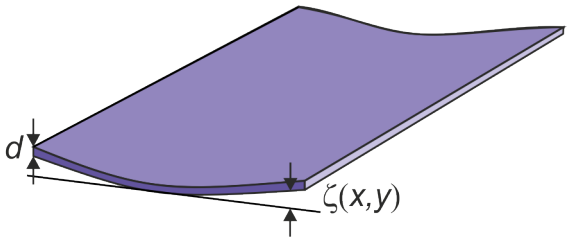

Figure 1.2: Large out-of-plane deflection $\zeta(x, y)$ of the film.

$$\kappa_{xy} = \frac{\partial^2 \zeta}{\partial x \partial y} \frac{1}{\left(1 + \left(\frac{\partial \zeta}{\partial x}\right)^2 + \left(\frac{\partial \zeta}{\partial y}\right)^2\right)^{3/2}}. \tag{1.14}$$

Neutral plane does not exist generally as in the case of small deflection, because the middle plane of the film is stretched by substantial membrane strain [12]

$$\varepsilon^m_{xx} = \frac{\partial u_x}{\partial x} + \frac{1}{2}\left(\frac{\partial \zeta}{\partial x}\right)^2, \tag{1.15}$$

$$\varepsilon^m_{yy} = \frac{\partial u_y}{\partial y} + \frac{1}{2}\left(\frac{\partial \zeta}{\partial y}\right)^2, \tag{1.16}$$

$$\varepsilon^m_{xy} = \frac{1}{2}\left(\frac{\partial u_x}{\partial y} + \frac{\partial u_y}{\partial x} + \frac{\partial \zeta}{\partial x}\frac{\partial \zeta}{\partial y}\right), \tag{1.17}$$

where u_x, u_y denote in-plane displacements solely due to stretching.

Stretching energy is given by

$$U_s = \frac{d}{2}\int\int \left[\varepsilon^m_{xx}\sigma^m_{xx} + \varepsilon^m_{yy}\sigma^m_{yy} + 2\varepsilon^m_{xy}\sigma^m_{xy}\right] \mathrm{d}x\mathrm{d}y, \tag{1.18}$$

where membrane stresses are given by Hooke's law

$$\sigma^m_{xx} = \frac{Y}{1-\nu^2}\left(\varepsilon^m_{xx} + \nu\varepsilon^m_{yy}\right), \tag{1.19}$$

$$\sigma^m_{yy} = \frac{Y}{1-\nu^2}\left(\varepsilon^m_{yy} + \nu\varepsilon^m_{xx}\right), \tag{1.20}$$

$$\sigma^m_{xy} = \frac{Y}{1+\nu}\varepsilon^m_{xy}. \tag{1.21}$$

Total elastic energy of the film U consists of decoupled bending energy eq. (1.8) and stretching energy eq. (1.18) [12]

$$U = U_b + U_s. \tag{1.22}$$

Equations of mechanical equilibrium are found also by minimizing the total elastic energy [12], resulting in the famous Föppl-von Kármán (FvK) equations

$$D\Delta^2\zeta - d\left(\frac{\partial^2\varphi}{\partial y^2}\kappa_{xx} + \frac{\partial^2\varphi}{\partial x^2}\kappa_{yy} - 2\frac{\partial^2\varphi}{\partial x\partial y}\kappa_{xy}\right) = 0, \tag{1.23}$$

$$\Delta^2\varphi = Y\left(\kappa_{xy}^2 - \kappa_{xx}\kappa_{yy}\right), \tag{1.24}$$

where φ is stress (Airy) function defined by

$$\sigma_{xx}^m = \frac{\partial^2\varphi}{\partial y^2},\ \sigma_{yy}^m = \frac{\partial^2\varphi}{\partial x^2},\ \sigma_{xy}^m = -\frac{\partial^2\varphi}{\partial x\partial y}. \tag{1.25}$$

For the case of initial biaxial stress σ_0 in the plate, left side of equation (1.23) will be supplemented by term $-d\sigma_0\Delta\zeta$ as in the case of small deflections eq. (1.12).

Since FvK equations are nonlinear and thus difficult to solve, the theoretical study of thin films has not evolved very rapidly. However, in the last 30 years, it increases to gain importance due to the applications and interest in microelectronics, thin coatings and biological membranes.

Chapter 2

Bending and wrinkling of strained films

In 1909, G. G. Stoney [16] has derived a formula to describe bending radius of thick substrate d_1 due to the thin (thickness d_2) strained film (ε_2) on top of it

$$R_{St} = \frac{\rho\delta^2 d_2}{6\varepsilon_2}, \tag{2.1}$$

where $\rho = \bar{Y}_1/\bar{Y}_2$ is the ratio of plane strain Young's moduli and $\delta = d_1/d_2$ is the ratio of thicknesses, Fig. 2.1. Stoney formula is widely used to estimate stresses in thin films from the measurement of curvature of thin films [17] and for description of micro- and nanocantilevers [1].

Timoshenko [18] has extended Stoney formula for substrate and film of similar thickness during study of heat-induced bending of bimetal stripe (thermostat) with different thermal expansion coefficient. The resulting radius of curvature is

$$R_{Ti} = \frac{d_2}{6\,(1+\nu)\,\varepsilon_2}\frac{1+4\rho\delta+6\rho\delta^2+4\rho\delta^3+\rho^2\delta^4}{\rho\delta\,(1+\delta)}, \tag{2.2}$$

where ε_2 is the thermal strain mismatch between the layers. Usually, there is only small deformation in thermostat (in comparison with other dimensions) and it will not form a complete scroll, because the thermal strains are generally too small. Already Stoney [16] described curling of strained metal film into beautiful coils when released from its host substrate.

In the last decade, selective chemical etching was employed to remove single layer from the layer stack and thus to obtain free-hanging film connected only to the etching front, Fig. 2.2(a). The film acquires equilibrium shape by relaxing its

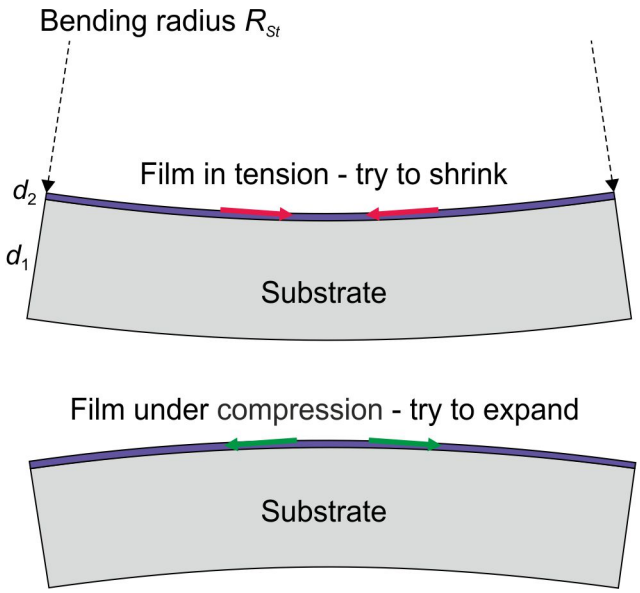

Figure 2.1: Illustration of bending of the thick substrate due to tensile strained (top) and compressed (bottom) thin film.

elastic energy. On one side, pure bending and roll-up to tubes with multiple rotations were observed and created lot of interest [8, 6], Fig. 2.2(b). On the other side and less noticed by the community, wrinkling (buckling) of the film at the etching front was observed in [19, 10], Fig. 2.2(c), and by many experimentalists in Max-Planck Institute for Solid State Research, Stuttgart and IFW Dresden, who actually aimed to get rolled-up tubes but ended up with wrinkled films. Most of the effects were considered undesirable and not reported publicly. However, if a reliable technology must be developed, the understanding of the conditions preferring rolling or wrinkling is very fundamental.

Whether the film bends or wrinkles sensitively depends on the built-in strain gradient across the film thickness. Intuitively speaking, if the strain gradient is large, the film bends into a curved structure, whereas for a small or zero strain gradient the film forms wrinkles. Interestingly, the competing mechanisms of wrinkling and bending, as the strain gradient inside the film changes, have not been quantified so far. This circumstance is even more surprising since a variety of fundamental investigations [21, 22, 23] as well as applications based on bent [16, 18, 1] and wrinkled [19, 9, 24, 10, 25] films have been put forward. The roll-up of a strained film into a cylindrical geometry seems particularly appealing [6, 8], since size, orientation and number of rotations of a micro- or nanotube become well-controlled and predictable entities. These virtues have led to exciting perspectives of radial superlattices [26],

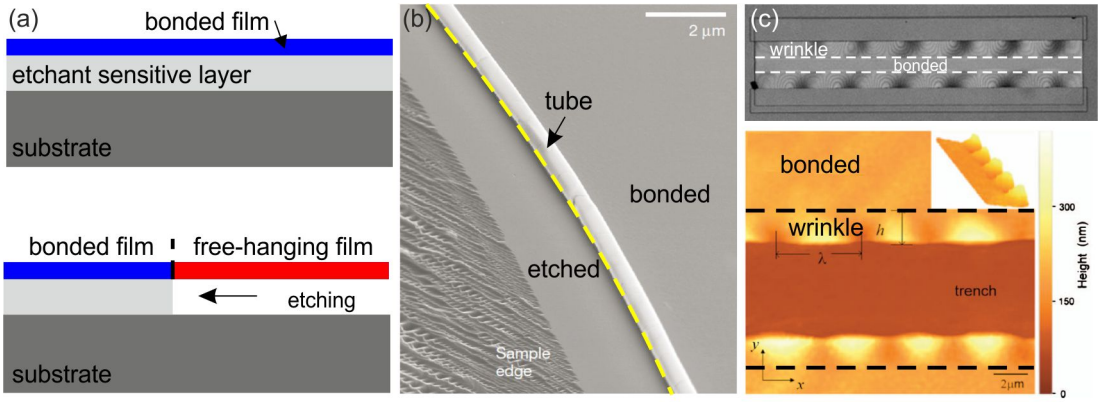

Figure 2.2: (a) Film bonded to an etchant-sensitive layer (top). During etching of the etchant-sensitive layer, part of the film is left free-hanging (bottom). (b,c) Different structures formed during strain relaxation of the free-hanging film fixed at the etching front (dashed lines). (a) Rolled-up tube, figure re-edited from [6]. (c) Wrinkled films, figures re-edited from [19] (top) and [20] (bottom).

optical microcavities [21, 27, 11], microtubular jet engines [28] and ultra-compact energy storage elements [29].

Various physical mechanism can be employed to produce intrinsic stresses in thin films, as reviewed for evaporated [30], sputtered [31], and epitaxial [32] thin films. If two layers with different stress state are stacked within the film, the stress (strain) gradient through film thickness arises from epitaxial mismatch strain [6], thermal strain [33] or surface stress imbalance in ultrathin layers of graphene [34] or silicon [22].

Etching of the etchant-sensitive sacrificial layer is a chemical reaction with lot of energy supply which directly breaks the bonds between sacrificial layer and top film and indirectly creates two new surfaces. The energetics of chemical etching cannot be simplified to the comparative interplay of surface and elastic energies unlike other systems such as epitaxial growth of self-assembled quantum dots.. We will not consider surface stress of the film, because we typically assume only films thicker than 10 nm. Below this thickness, the effect of surface stress will change the expression for bending radius of bilayer [35].

In this chapter, we assume a partially released bilayer film, consisting of two layers with thicknesses d_1 and d_2, which are subject to biaxial strain ε_1 and ε_2, respectively, Fig. 2.3(a). The film is free-hanging over the etching length h, which is free to elastically relax, constrained only by the fixed etching front boundary. The unreleased part of the film is still firmly bonded to the sacrificial layer. The average strain of the

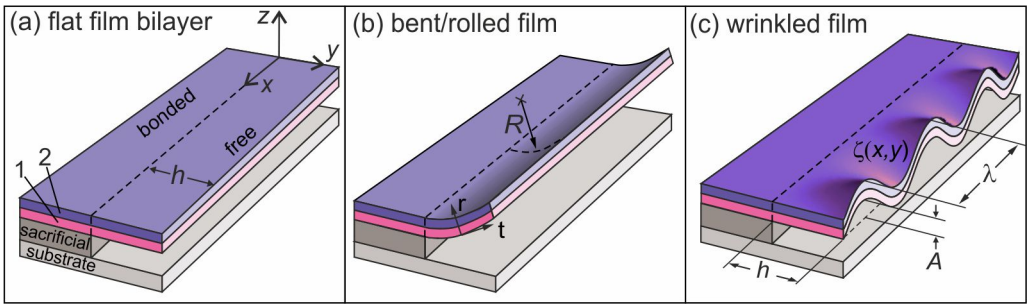

Figure 2.3: Schematics of (a) free-hanging bilayer film with the length h, (b) bent film with radius of curvature R and (c) wrinkled film with deflection profile $\zeta(x, y)$, amplitude A and period λ.

bilayer is defined as

$$\bar{\varepsilon} = \frac{\varepsilon_1 d_1 + \varepsilon_2 d_2}{d_1 + d_2} \tag{2.3}$$

and the strain gradient is defined as

$$\Delta\varepsilon = \varepsilon_2 - \varepsilon_1. \tag{2.4}$$

The initial elastic energy (given per unit area) of the film is

$$U_0 = \frac{Y}{1-\nu}\left(d_1\varepsilon_1^2 + d_2\varepsilon_2^2\right). \tag{2.5}$$

Throughout this chapter, we consider a typical bilayer consisting of 10 nm $In_{0.1}Ga_{0.9}As$ with $\varepsilon_1 = -0.71\%$ and 10 nm GaAs with $\varepsilon_2 = 0\%$. Different isotropic elastic constants Y_1, Y_2, ν_1, ν_2 are considered where possible, but for simplicity of some expressions equal isotropic elastic constants $Y = 80$ GPa, $\nu = 0.31$ are inserted. We consider the initial stage of strain relaxation for the case $\Delta\varepsilon > 0$ which leads to rolling-up away from the substrate, Fig. 2.3(b). The opposite situation with $\Delta\varepsilon < 0$ leads to rolling-down of the bilayer film to the substrate and will be commented in the discussion.

We will compute the elastic energy of bent and wrinkled free-hanging film. A preferable shape diagram of the relaxed free-hanging films is then constructed by comparing the elastic energy of bent and wrinkled film shape. We also consider a rolled-up tube, which has already performed multiple rotations during relaxation and eventually stops rolling further due to competing relaxation into wrinkle shape near the etching front. Based on this model, we provide an upper limit for the maximum achievable number of tube rotations.

2.1 Bent free-hanging films

The radius of rolled-up tubes can be estimated with Timoshenko model, eq. (2.2), which shows good agreement with experiment [36]. Long (short) tubes show plane strain (stress) relaxation along the tube axis [37], which is reflected in the constant $1+\nu$ in the denominator of eq. (2.2).

We adopt the approach from Ref. [37] to estimate the elastic energy of the bent film. The film bends and adapts a uniform inner radius R. The energy calculation is performed in a cylindrical coordinate system (x,t,r) with the origin at the outer surface of the bent film in Fig. 2.3(b). Since the film is still firmly attached to the sacrificial layer, and we assume $L \gg R$, there is no relaxation in the x direction [38] (plane strain condition in x) and thus $\varepsilon_{xxi} = \varepsilon_i$ for layer no. 1 and no. 2, respectively. For the position of top z_{i+1} and bottom z_i surface of layer i we use notation from eq. (1.4).

In the tangential direction, the strain can relax by bending and the final tangential strain can be written as

$$\varepsilon_{ti} = \varepsilon_i + \varepsilon_{const} - \frac{r - r_b}{R}, \tag{2.6}$$

where ε_{const} is a constant strain, r_b indicates the location of the neutral plane and the last term is the bending strain component eq. (1.1). The transverse radial strain is given from eq. (1.6)

$$\varepsilon_{ri} = -\frac{\nu_i}{1-\nu_i}(\varepsilon_{ti} + \varepsilon_{xxi}). \tag{2.7}$$

From the condition of zero total bending force on the film from the bending strain

$$\sum_{i=1}^{2} \overline{Y}_i \int_{z_i}^{z_{i+1}} \frac{r - r_b}{R} \mathrm{d}r = 0 \tag{2.8}$$

we derive

$$r_b = \frac{d_2(1 + 2\delta + \rho\delta^2)}{2(1+\rho\delta)}, \tag{2.9}$$

where

$$\delta = \frac{d_1}{d_2}, \tag{2.10}$$

$$\rho = \frac{\overline{Y}_1}{\overline{Y}_2}. \tag{2.11}$$

The total elastic energy of the bent film is calculated by integrating the elastic

strain energy density from the outer to the inner film surface

$$U_{bent} = \sum_{i=1}^{2} \frac{\overline{Y}_i}{2} \int_{z_i}^{z_{i+1}} \left(\varepsilon_{ti}^2 + \varepsilon_{xxi}^2 + 2\nu_i \varepsilon_{ti} \varepsilon_{xxi}\right) \mathrm{d}r. \tag{2.12}$$

By minimizing the energy of the bent film with respect to the remaining unknown parameters ε_{const} and R

$$\frac{\partial U_{bent}}{\partial \varepsilon_{const}} = 0, \ \frac{\partial U_{bent}}{\partial R} = 0, \tag{2.13}$$

we obtain the equilibrium constant strain

$$\varepsilon_{const0} = -\frac{\rho\delta\left(1+\nu_1\right)\varepsilon_1 + \left(1+\nu_2\right)\varepsilon_2}{1+\rho\delta} \tag{2.14}$$

and the equilibrium tube radius

$$R_0 = \frac{d_2}{6\left[\left(1+\nu_2\right)\varepsilon_2 - \left(1+\nu_1\right)\varepsilon_1\right]} \frac{1 + 4\rho\delta + 6\rho\delta^2 + 4\rho\delta^3 + \rho^2\delta^4}{\rho\delta(1+\delta)}. \tag{2.15}$$

For the approximation of the same elastic properties of both layers we can write

$$R_0 = \frac{\left(d_1 + d_2\right)^3}{6\left(1+\nu\right) d_1 d_2 \Delta\varepsilon}, \tag{2.16}$$

in agreement with previous reports [36, 39].

Subsequently, R_0 and ε_{const0} are used to calculate the equilibrium minimum elastic energy of the rolled structure, which for equal elastic constants reads

$$U_{b0} = \frac{U_{bent}(R_0, \varepsilon_{const0})}{U_0} = \frac{2 + 2(1-2\nu)\delta + 2(2-\nu)\delta^2 + (1-\nu)\delta^3}{2(1+\delta)^3}. \tag{2.17}$$

and for symmetric bilayer ($\delta = 1$) U_{b0} equals to $\frac{9-7\nu}{16}$. Amazingly, it depends only on Poisson's ratio of the film and thickness ratio, but not on the strain gradient. The value of bent energy will be later compared with the wrinkle energy. For the typical bilayer, the equilibrium radius and minimum energy are $R_0 \approx 1.4\ \mu\mathrm{m}$ and $U_{b0} = 0.43$, respectively.

2.2 Wrinkled free-hanging films

If the free-hanging film is sufficiently compressed along the fixed boundary, it will buckle and deform out of its plane. Wrinkling of free-hanging films was first studied

during etching of polysilicon [19] and SiGe [10] films. The strain distribution in wrinkled film was obtained qualitatively by micro-Raman spectroscopy [20]. The free-hanging film geometry is also found during swelling of gels in macroscopic context [24] and during tearing of plastic sheets [40, 41] or growth of plant leaves [41, 42]. Wrinkling period of the free-hanging film was estimated by energy minimization of post-buckled shape $\lambda \approx 28h^{0.62}$ [10] or by linear stability analysis valid just at the onset of wrinkling $\lambda \approx 3.3h$ [24]. Very recently, wrinkling near edges with self-similar fractal features was reviewed from the mathematical perspective [4].

For the calculation of the elastic energy of the wrinkled structure, we extend a previous formulation of a single layer [10] to the bilayer film. We parameterize the vertical deflection of the wrinkle as

$$\zeta(x, y) = Af(y/h)\cos(kx), \tag{2.18}$$

where A is the maximum amplitude of the wrinkle at the free end, Fig. 2.3(c), $k = 2\pi/\lambda$ is the wrinkle wavenumber in the x direction (λ is period of the wrinkle) and we choose Ansatz function $f(y/h)$ for connecting the wrinkled to fixed planar boundary

$$f(y/h) = \frac{1 - \cos(\frac{\pi y}{h})}{2}. \tag{2.19}$$

The fixed boundary forces the left side of the wrinkle to be clamped, i.e.

$$\zeta(x, 0) = 0 \text{ and } \frac{\partial \zeta}{\partial y}(x, 0) = 0, \tag{2.20}$$

which is satisfied naturally by our choice of $f(y/h)$.

The boundary conditions for free edge read [12]

$$\frac{\partial^3 \zeta}{\partial y^3}(x, 1) + (2 - \nu)\frac{\partial^3 \zeta}{\partial y \partial x^2}(x, 1) = 0, \tag{2.21}$$

$$\frac{\partial^2 \zeta}{\partial y^2}(x, 1) + \nu\frac{\partial^2 \zeta}{\partial x^2}(x, 1) = 0. \tag{2.22}$$

First boundary condition reads for our wrinkle profile

$$\frac{f'''(1)}{h^3} - (2 - \nu)k^2\frac{f'(1)}{h} = 0,$$

and it is satisfied automatically

$$\frac{1}{2}\left(\frac{\pi}{h}\right)^3 \sin(\pi) - (2-\nu)k^2\frac{1}{2}\left(\frac{\pi}{h}\right)\sin(\pi) = 0.$$

By inserting our wrinkle profile in the second boundary condition we get

$$\frac{f''(1)}{h^2} - \nu k^2 f(1) = 0,$$

and by inserting eq. 2.19

$$\frac{1}{2}\left(\frac{\pi}{h}\right)^2 \cos(\pi) + \nu k^2 \cos(\pi) = 0.$$

This condition is not satisfied by our choice of $f()$, but the elastic edge energy is low compared with elastic energy in plate volume in the films we considered. Moreover, the free-edge might not be completely free in reality because of fluid-structure interactions. Therefore, we have used this ansatz function for the ease of the numerical calculation.

The in-plane displacement u_x is approximated by modifying the result of the in-plane equilibrium for our shape [43],

$$u_x = \frac{k\left[Af(y/h)\right]^2}{8}\sin(2kx). \tag{2.23}$$

The film is free to move in y, so we take

$$u_y = qy \tag{2.24}$$

neglecting an x dependence and with parameter q, denoting the magnitude of relaxation in the y direction.

The membrane strain ε^m in the layers is defined according to the large deflection plate theory, eqs. (1.15), (1.16) and (1.17), but with addition of the initial biaxial strain ε_i for i-th layer. The membrane stress σ^m is computed from Hooke law eqs. (1.19), (1.20) and (1.21).

The total wrinkle elastic energy U_w can be decoupled into stretching energy U_{sw} (eq.(1.18)) and bending energy U_{bw} (eq. (1.8))

$$U_w = U_{sw} + U_{bw}. \tag{2.25}$$

The interplay between the stretching and bending energies will determine the equilibrium wrinkle period and amplitude. Bending energy U_{bw} is computed with the modified bending rigidity of the bilayer film [44]

$$D_{12} = \frac{Y_1 d_1^3}{12\left(1-\nu_1^2\right)} \frac{1+\rho^2\delta^4+2\rho\delta\left(2+3\delta+2\delta^2\right)}{1+\rho\delta}. \tag{2.26}$$

Due to the increasing length of the expressions, we will show the formulas only for the case of symmetric bilayer $d_1 = d_2$ $(d = 2d_1)$, equal elastic constants and $\varepsilon_1 < 0$, $\varepsilon_2 = 0$. The wrinkle bending energy per unit length in x is obtained by integrating in y from 0 to h and averaged over one period λ

$$U_{bw} = \frac{A^2 d^3 Y\left(3h^4k^4+2h^2k^2\pi^2+\pi^4\right)}{384h^3\left(1-\nu^2\right)} \tag{2.27}$$

and stretching energy per unit length is also calculated in the same fashion

$$\begin{aligned} U_{sw} = \frac{dY}{h^3\left(1-\nu^2\right)}\{&\frac{h^4q^2}{2} + \frac{A^2h^2q}{32}\left(\pi^2+3h^2k^2\nu\right) \\ &+ \frac{A^4}{16384}\left[140h^4k^4+18\pi^4+5h^2k^2\pi^2(1+7\nu)\right] \\ &+ h^2(1+\nu)\varepsilon_1\left[\frac{A^2}{64}\left(3h^2k^2+\pi^2\right)+\frac{h^2(q+\varepsilon_1)}{2}\right]\}. \end{aligned} \tag{2.28}$$

We will find minimum elastic energy of wrinkle (and hence its equilibrium morphology) by finding stationary points of elastic energy. We start with stationary point with respect to relaxation in y direction

$$\frac{\partial U_w}{\partial q} = 0, \tag{2.29}$$

which gives the equilibrium relaxation parameter

$$q_0 = -\frac{A^2}{h^2}\frac{\pi^2+3A^2k^2\nu}{32} - \frac{\varepsilon_1(1+\nu)}{2}. \tag{2.30}$$

Then we put q_0 into expression for stretching energy eq. (2.28) and find equilibrium with respect to A

$$\frac{\partial U_w}{\partial A} = 0, \tag{2.31}$$

which results in equilibrium amplitude

$$A_0 = 8\sqrt{\frac{-d^2\left(3h^4k^4 + 2h^2k^2\pi^2 + \pi^4\right) - 18h^4k^2\left(1-\nu^2\right)\varepsilon_1}{3\left[10\pi^4 + h^2k^2\pi^2(5-13\nu) + 4h^4k^4\left(35-18\nu^2\right)\right]}}. \tag{2.32}$$

Since amplitude A_0 has to be real positive number, expression under square root should be greater than zero (because denominator is always greater than 0), leading to inequality

$$-d^2\left(3h^4k_s^4 + 2h^2k_s^2\pi^2 + \pi^4\right) - 18h^4k_s^2\left(1-\nu^2\right)\varepsilon_1 \geq 0.$$

The solution of this inequality is interval

$$k_{s1} \leq k_s \leq k_{s2},$$

where

$$k_{s1} = \sqrt{-\frac{\pi^2}{9h^2} - \frac{\varepsilon_1}{d^2}(1+\nu^2) - \frac{\sqrt{\left(2d^2\pi^2 + 18h^2\varepsilon_1 - 18h^2\nu^2\varepsilon_1\right)^2 - 12d^4\pi^4}}{18d^2h^2}}, \tag{2.33}$$

$$k_{s2} = \sqrt{-\frac{\pi^2}{9h^2} - \frac{\varepsilon_1}{d^2}(1+\nu^2) + \frac{\sqrt{\left(2d^2\pi^2 + 18h^2\varepsilon_1 - 18h^2\nu^2\varepsilon_1\right)^2 - 12d^4\pi^4}}{18d^2h^2}}. \tag{2.34}$$

The argument of the nested square root in previous expression is the same for both k_{s1}, k_{s2} and it is negative below a "critical etching length" for wrinkle formation

$$h_{cw} = \frac{\pi d}{3}\sqrt{\frac{1+\sqrt{3}}{-\left(1-\nu^2\right)\varepsilon_1}}, \tag{2.35}$$

This implies that the wrinkle is not energetically preferred at $h < h_{cw}$. Above this critical etching length, real wavevector is obtained. Minimization of wrinkle elastic energy U_w with respect to wavenumber k becomes

$$\begin{aligned}\frac{\partial U_w}{\partial k} &= d^4\left(3h^4k^4+2h^2k^2\pi^2+\pi^4\right)\left(9h^4k^4\pi^2(-5+13\nu)-\pi^6(35+13\nu)\right.\\ &+ \left.2h^2k^2\pi^4(75+(13-72\nu)\nu)+\underline{24h^6k^6\left(-35+18\nu^2\right)}\right)\\ &+ 36h^2\left(-1+\nu^2\right)\varepsilon_1\left(2d^2\left(20h^2k^2\pi^6+5\pi^8+\underline{3h^6k^6\pi^2(5-13\nu)}\right.\right.\\ &+ \left.6h^8k^8\left(35-18\nu^2\right)+h^4k^4\pi^4(-20+\nu(-13+36\nu))\right)\\ &+ \left.9h^4k^2\pi^2\left(-1+\nu^2\right)\left(\underline{-20\pi^2}+h^2k^2(-5+13\nu)\right)\varepsilon_1\right)\\ &= 0. \end{aligned} \tag{2.36}$$

If we keep only the terms with largest numerical scale (underlined), i.e. h^6k^2, h^8k^4 and $h^{10}k^8$ and divide them all with h^6k^2, we obtain

$$a_1+a_2k_0^2+a_3k_0^6=0, \tag{2.37}$$

where

$$a_1=60\pi^4\varepsilon_1\left(1-\nu^2\right), \tag{2.38}$$

$$a_2=3\pi^2h^2\varepsilon_1\left(1-\nu^2\right)(5-13\nu), \tag{2.39}$$

$$a_3=4d^2h^4\left(35-18\nu^2\right). \tag{2.40}$$

Previous equation for k_0 is the sixth order polynomial equation and its symbolic solution, which is real and positive, can obtained with Mathematica [45], the equilibrium wavenumber

$$k_0=\sqrt{-\frac{\left(\frac{2}{3}\right)^{1/3}a_2}{\left(-9a_1a_3^2+\sqrt{3}\sqrt{4a_2^3a_3^3+27a_1^2a_3^4}\right)^{1/3}}+\frac{\left(-9a_1a_3^2+\sqrt{3}\sqrt{4a_2^3a_3^3+27a_1^2a_3^4}\right)^{1/3}}{2^{1/3}3^{2/3}a_3}}, \tag{2.41}$$

The equilibrium wrinkle period is then expressed as $\lambda_0=2\pi/k_0$ and it is shown on Fig. 2.4(a). By expansion in h we also find the leading order term for wrinkle period

$$\lambda_0^*=2\sqrt{2\pi}h^{2/3}\left(-\frac{d^2\left(35-18\nu^2\right)}{120\pi\left(1-\nu^2\right)\varepsilon_1}\right)^{1/6}, \tag{2.42}$$

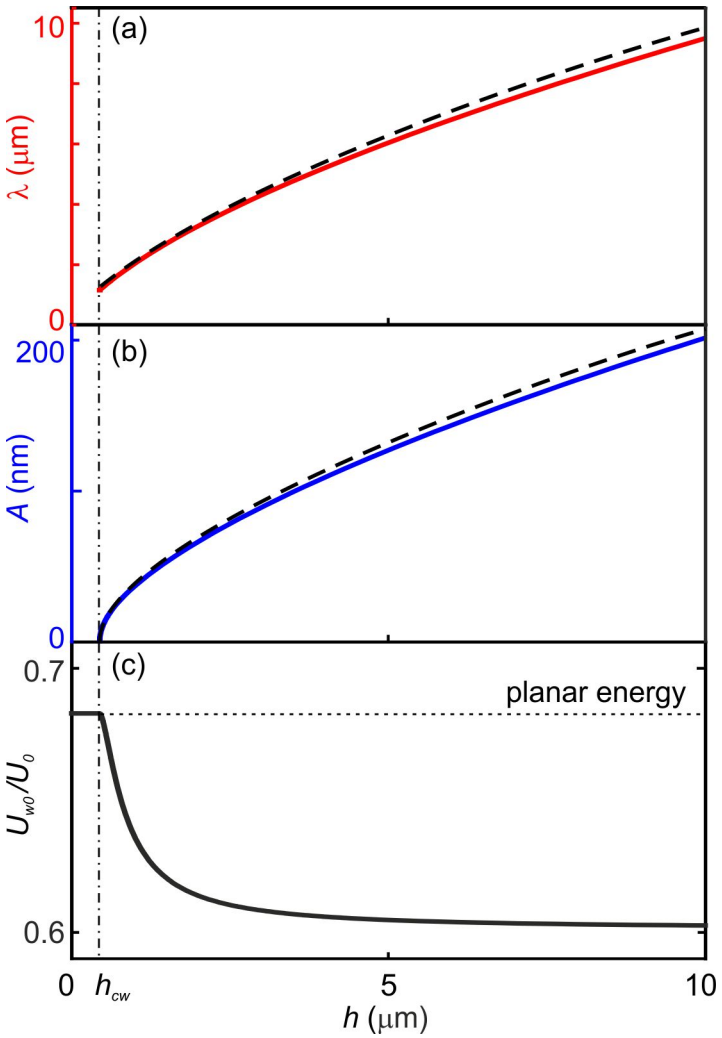

Figure 2.4: Equilibrium wrinkle (a) period (red), (b) amplitude (blue) and (c) energy as function of etching length h. Vertical dash-dotted line marks the critical wrinkle length h_{cw}. Dashed curves in (a) and (b) show leading order terms. Parameters of typical bilayer structure are used.

which is shown as dashed curve in Fig. 2.4(a). This scaling is similar to the previously reported scaling for the single layer wrinkling in the same geometry $h^{0.62}$ [10] and slightly different from the $h^{0.5}$ reported for the wrinkling phenomena in general geometry [46]. Equilibrium wrinkle amplitude is obtained by inserting eq. (2.41) into eq. (2.32) (symbolic expression is too long to show) and the numerical result for our typical bilayer structure is shown in Fig. 2.4(b).

Below the critical etching length for wrinkle formation $h_{cw} \approx 439$ nm,[1] the bilayer cannot buckle $A = 0$, $k = 0$ and relaxes only in-plane in y direction with $q_0 = -\varepsilon_1(1+\nu)/2$. The elastic energy is decreased to $0.68U_0$ ("planar" energy), Fig. 2.4(c).

Above h_{cw}, wrinkling can occur with nonzero amplitude and energy lower than the planar energy. The equilibrium wrinkle energy U_{w0} as a function of etching length h is obtained by inserting equilibrium q_0, A_0 and k_0 from eqs. (2.30), (2.32) and (2.41) into eqs.(2.25),(2.27) and (2.28). Because the expression is rather large, we only show its numerical dependence in Fig. 2.4(c). For very large h, the wrinkle energy U_{w0} decreases down to an asymptotic value $0.60U_0$.

Our minimum of the total elastic energy is equivalent to the mechanical equilibrium state obtained from solving the non-linear FvK equations within our class of shapes [12]. It is beyond the scope of this work to calculate the exact solution from these equations, and a combination of bent and wrinkled shape might indeed be the accurate shape obtained by exactly solving the FvK equations.

2.3 Competition of bending and wrinkling of the film

The preferable shape of the free-hanging film of length h is determined by comparing the elastic energy of the bent U_{b0} and wrinkle U_{w0} shapes. For our typical bilayer, the energy of the wrinkled film U_{w0} is between $0.60U_0$ and $0.68U_0$, Fig. 2.4(c), which is always larger than the energy of the bent structure $U_{b0} = 0.43U_0$. Therefore bent film is energetically preferred over wrinkled film for the typical bilayer.

To extend our considerations, we calculated the energetically favorable shapes as a function of etching length h and strain gradient $\Delta\varepsilon$ for fixed average strain $\bar{\varepsilon}$, as shown in the shape diagram, Fig. 2.5. For example, for $\Delta\varepsilon = 0.20\%$ and

[1] This is in analogy to critical buckling stress for buckling of rods, but here we change dimension rather than the stress.

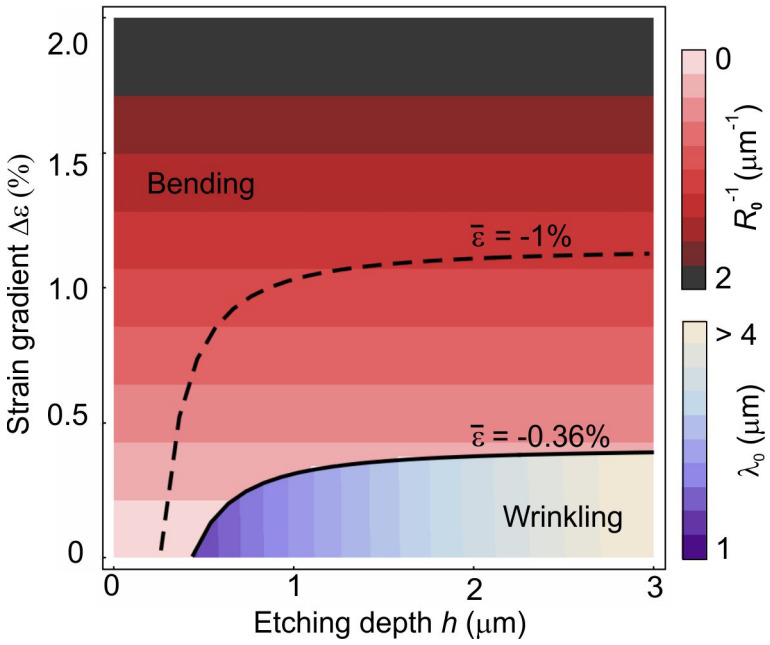

Figure 2.5: Shape diagram of favorable shapes of free-hanging film fixed at one edge. Radius of curvature R_0^{-1} is shown for the bent structure and equilibrium wrinkle period λ_0 for the wrinkled structure. Solid curve shows the boundary between bent and wrinkled shapes for our typical structure and dashed curve for $\bar{\varepsilon} = -1.0\%$.

$\bar{\varepsilon} = -0.36\%$, bending will be favored only until h is increased to ≈ 700 nm. Beyond this length, the wrinkle becomes favorable geometry as it acquires lower energy than the bent structure. If we consider higher average strain, for example $\bar{\varepsilon} = -1.0\%$ (dashed boundary in Fig. 2.5), the phase boundary curve moves upward and the wrinkling region is enlarged.

Based on above analysis, we make following remarks :

1. Altering our assumption on the wrinkle shape (e.g. from trigonometric to polynomial function) and varying elastic constants within realistic values does not qualitatively change our results.

2. Our theory is valid for asymmetric bilayers as well, but the phase diagram and the maximum number of rotations will be quantitatively modified.

3. For tensile average strain $\bar{\varepsilon} > 0$, no physical minimum of wrinkling energy exists for our model, consistent with observations of wrinkles only for compressive strains near the fixed boundary [19, 24, 10, 46].

4. In typical experiments the layer is partially released by selectively etching away a sacrificial buffer layer [6]. If the amplitude of the wrinkle becomes too large,

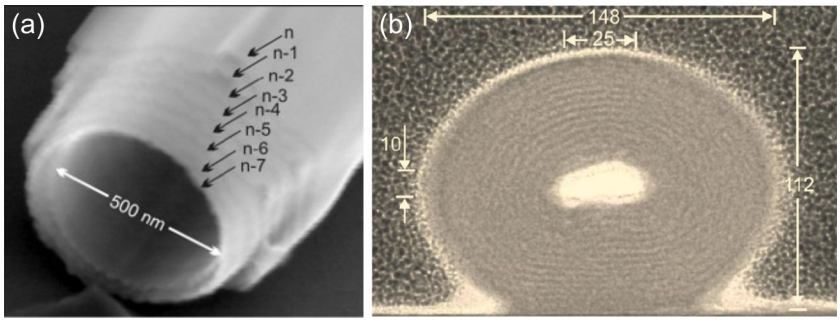

Figure 2.6: Scanning electron micrograph of rolled-up tube with ~39 rotations and first 8 rotations labeled, taken from [9]. (b) Transmission electron micrograph of rolled-up tube with 35-40 rotations. Dimensions are shown in nanometers. Taken from [48].

the film may touch the substrate [25]. In this case our model does not apply, because the film-substrate interaction energies might be larger than the elastic energy relaxation through bending and/or wrinkling. The same applies for $\Delta\varepsilon < 0$, where the film rolls-down towards the substrate surface [47].

The shape diagram in Fig. 2.5 can be used as a predictive tool for the deliberate design of rolled-up/wrinkled structures based on defined strains inside the constituent layers.

2.4 Maximum number of tube rotations

The maximum number of tube rotations observed in experiments so far is relatively low (~ 40) [9, 48], Fig. 2.6. One reason might be that wrinkling becomes energetically preferable over bending during the final stage of tube rolling-up. We can use wrinkling model from previous section to estimate energies for this scenario and obtain a limit for the maximum number of tube rotations N_{max} for a film released from the substrate by progressive underetching.

Consider the tube, which has already rolled up some rotations and the subsequent windings do not interact. The tube radius for the first rotation is the equilibrium tube radius R_0 and it linearly increases with the number of rotations N (continuous variable) as

$$R_N = R_0 + N(d_1 + d_2). \tag{2.43}$$

We consider an additional portion of the released layer of length H as outlined in Fig. 2.7(a). The film has two pathways to relax. Either the film continues to roll up with

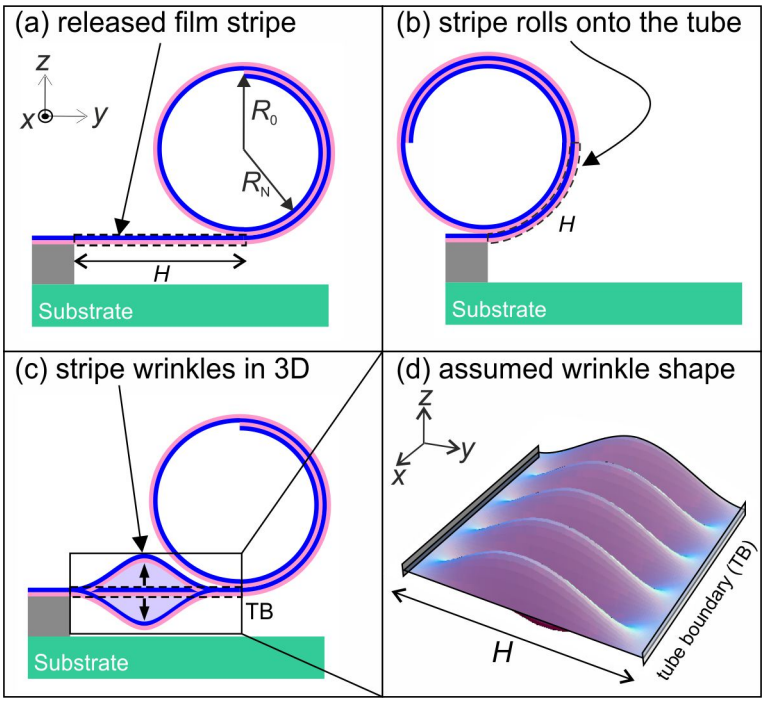

Figure 2.7: Schematic illustration of the mechanism, which ceases the roll-up process. (a) A strip of length H can (b) roll onto the outer part of the tube or (c) wrinkle, depending on the final energy of the system. (d) Assumed 3D wrinkle profile between fixed boundary (left) and tube boundary (TB, right).

radius R_N, Fig. 2.7(b) or forms wrinkles, Figs. 2.7(c) and (d). These two processes are energetically compared to calculate the maximum number of rotations.

When the film of length H is rolled onto the tube with outer radius $R > R_0$, the energy stored in the layer increases as the radius increases. The energy of a rolled up film as a function of its radius is calculated by eq. (2.12) for constant equilibrium strain ε_{const0} and hence (for layers with equal elastic constants)

$$U_{bent}(R) = \frac{(1+\delta)^4 d_2^2 + 12R\delta(1+\delta)d_2\varepsilon_1\,(1+\nu) + 12R^2\delta\varepsilon_1^2\,(2+\delta+\nu\,(2-\delta\nu))}{24R^2\delta(1+\delta)\varepsilon_1^2\,(1+\nu)}. \tag{2.44}$$

Fig. 2.8(a). For infinite radius the energy approaches the value of a planar relaxed film

$$U_{planar} = \frac{2+\delta(1-\nu)}{2(1+\delta)}. \tag{2.45}$$

The wrinkle shape between the etching front and tube boundary (TB) can be assumed to be doubled with respect to the wrinkle profile in previous section, eq.

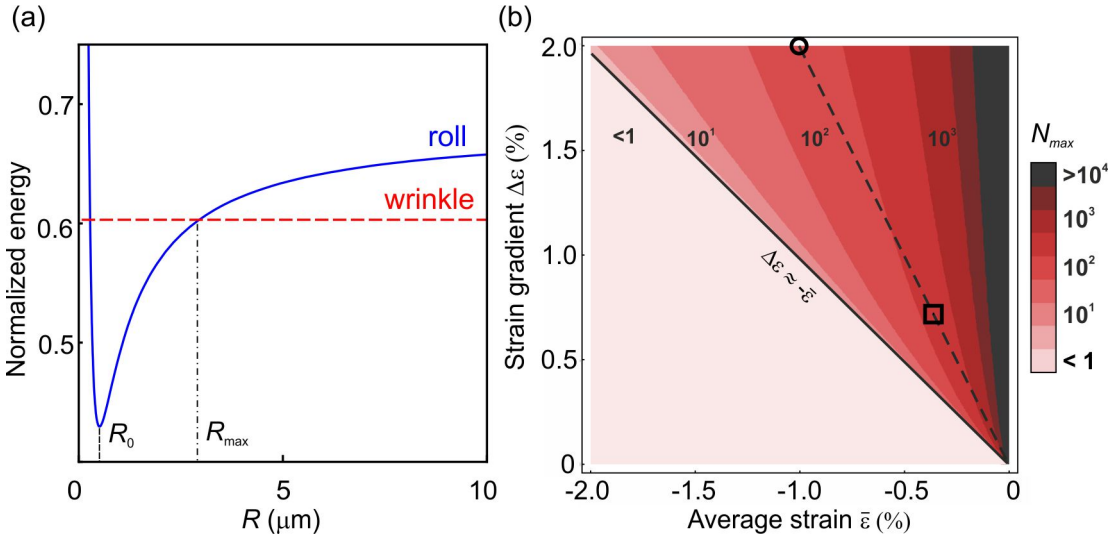

Figure 2.8: (a) Comparison between the elastic energies of roll-up and wrinkle shape for $\bar{\varepsilon} = -1.0\%$ and $\Delta\varepsilon = 2.0\%$ (circle point in the diagram). (b) Contour of the maximum number of tube rotations $N_{\max}$ as a function of average strain and strain gradient for the considered wrinkle length $H = 3H_{cw}$. Square point denotes our typical strain combination as specified in the text. The dashed line denotes typical strain combinations for bilayers, where only one layer is compressively strained initially.

(2.18), since now the right wrinkle edge has to be smoothly clamped to the tube boundary (TB), i.e.

$$\zeta(x, H) = 0, \ \frac{\partial \zeta}{\partial y}(x, H) = 0, \tag{2.46}$$

Fig. 2.7(c). Therefore, to calculate the energy of this wrinkled film portion, the previous formulation needs to be slightly modified. Since the shape of wrinkles was enlarged by symmetric half, the averaged wrinkle energy stays same, Fig. 2.4(c).

The elastic energy of the wrinkled portion will be now compared with the elastic energy of the rolled-up portion. The maximum radius of the outer tube rotation $R_N = R_{\max}$ is reached when the energy of wrinkle portion becomes lower than the energy of roll-up portion as shown on Fig. 2.8(a). For this comparison we take $H = 3H_{cw}$, since for this length the strain energy is largely relaxed compared to the planar value, see Fig. 2.4(c) for wrinkle with half-size domain $h = 3h_{cw}$. The maximum number of rotations is then determined by the relation

$$N_{\max} = \frac{R_{\max} - R_0}{d_1 + d_2}. \tag{2.47}$$

For a broad range of average strain and strain gradient, the maximum number of

tube rotations is shown in Fig. 2.8(b). For our typical structure we obtain $N_{\max} \approx 510$, square point in Fig. 2.8(b). Rolled-up films with less than one rotation are obtained for $\Delta\varepsilon < -\bar{\varepsilon}$, otherwise $N_{\max}$ increases rapidly when the magnitude of average strain is decreased towards zero for non-zero $\Delta\varepsilon$.

For the estimation of the maximum number of tube rotations, we assume non- or only weakly interacting windings. If the windings are tightly bonded together, the infinitesimally small incremental increase in H during roll-up does not allow a sufficient length for wrinkling and thus the number of rotations is not limited within the framework of our model. Both cases, tightly bonded [26, 49] and non- or weakly interacting windings [50], have been reported in the literature. The number of rotations might be influenced by certain process parameters such as finite fluid flow during underetching. In this way the maximum number of rotations might be increased if the fluid flow is applied along the roll-up direction. For short films, i.e. $L_x \ll R$, wrinkling might not occur due to the full relaxation in the tube-axial direction (plane stress) [37]. As a result, there is no limit of the number of rotations within the framework of our model. Considering H much larger than $3H_{cw}$ (which approaches the saturation wrinkle energy) will lead to a decrease of $N_{\max}$ on the order of 10%.

More systematic experimental data to explore the maximum number of tube rotations are missing. The maximum reported values $N_{\max}$ for $In_{0.33}Ga_{0.67}As$ are 30-40 rotations [9, 48], about one order of magnitude below our prediction $N_{\max} \approx 250$ for this system. This might be due to specific processing parameters present in experiments, for instance a misalignment of the rolling direction from the preferential rolling direction due to its crystallographic softness, an inhomogeneous etching front and loose rotations [9]. Therefore, the maximum experimentally obtained number of rotations have always been lower than our theoretical estimate.

2.5 Conclusion

We have performed an energetic comparison between the bending and wrinkling of compressively strained free-hanging films, and we have drawn the phase diagram for the preferential shape of the film as a function of length, average strain and strain gradient. For small strain gradients $\Delta\varepsilon$, the film wrinkles, while for sufficiently large strain gradient, a phase transition from wrinkling to bending occurs. We have applied our theory to estimate the maximum number of tube rotations during a roll-up process. We are aware of the limitations of our model, which we have carefully discussed and taken into account for all interpretations. Our considerations provide the theoretical

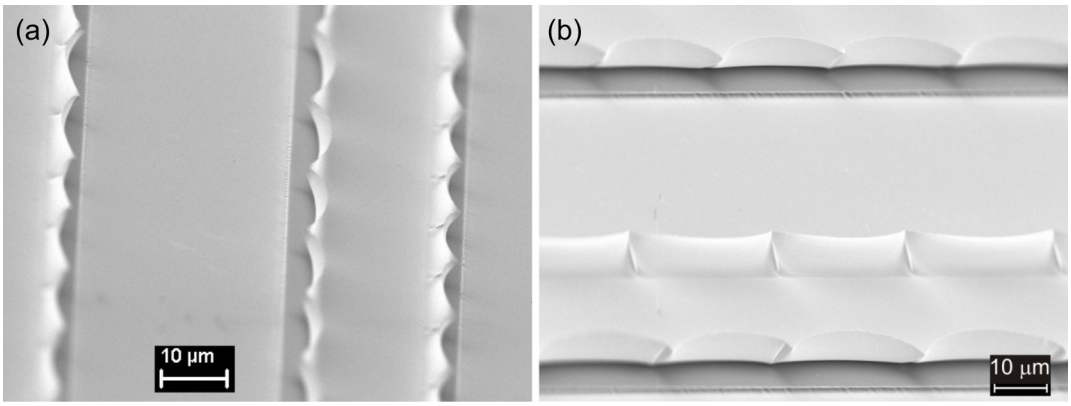

Figure 2.9: Side view scanning electron micrographs of structures mixed from bent and wrinkle shape (a) viewed along the trench and (b) viewed perpendicular to the trench.

framework to fundamentally understand bending and wrinkling of free-hanging films attached to one fixed boundary. Since such layers have gained substantial relevance for applications, our work is of practical interest for many materials and material combinations as well as for different geometries and length scales.

2.6 Outlook

The results of this chapter for determining preferred shape of free-hanging film have inherent limits. Most importantly, the distinction between bent and wrinkled shape doesn't have to be satisfied in experiments. At the end of my thesis work, the $In_{0.1}Ga_{0.9}As/GaAs$ bilayer samples with short etching length ($\sim 5\ \mu m$) of sacrificial AlAs layer were prepared within the collaboration with Dr. A. Malachias and Dr. Ch. Deneke (both at LNLS Brasil). I designed and structured samples of various thicknesses with conventional optical lithography. The measured X-ray diffraction on ensemble of structures with mixed tube and wrinkle shape reveals interesting strain states. The scanning electron micrograph shows beautifully periodic mixed morphologies of bent and wrinkled film, Fig. 2.9. With this study, we hope to further refine understanding of the relaxation of free-hanging films. Another interesting features are the singular points "crumples" where bent region goes into wrinkled region, Fig. 2.9(b). Study of crumples is recently active field of research ranging from paper down to graphene [51]. Further details will be published elsewhere.

Chapter 3

Rolling-up of wrinkled films

Many promising applications of rolled-up nanomembranes have been proposed and demonstrated in the last decade [6, 52, 33, 53]; however each of them requires special structural and geometrical prerequisites. For instance, long tubes with small diameters are most suitable for applications such as nanopipelines [54] and metamaterial fibers [55], Fig. 3.1(a). Compact tubes with many windings are preferred for capacitors [29], coils [52] or X-ray waveguiding tubes [48], Fig. 3.1(b,c). Similarly, carbon nanoscrolls [56, 34, 57] possess unusual electronic [58] and optical properties [59], and because of their unique topology, they facilitate chemical doping [60] and hydrogen storage [61] for possible use in super capacitors and batteries [60]. Rigorous control of the rolling process and the realization of novel tubular shapes lie at the heart of a more deterministic deployment of these rolled-up nanomembranes.

Let us consider a typical flat rectangular film pattern with initial strain gradient across the film thickness. Once the film is released from the substrate, it first bends at all four edges simultaneously. However, further bending (rolling) occurs only along the long edges of the rectangular film, Fig. 3.2, because longer edges experience larger bending force/moment than the shorter edges [62, 63]. After finishing our work, two relevant experimental and numerical studies appeared; a statistical study on percentage of tubes rolled-up from long or short edge [64]; and study how edge curvature effects determine the direction of bilayer bending [65].

To experimentally overcome the limitation of tubes forming only at the long edge of the pattern together with poor rolling behavior at the corners and to control the final position of the tubes, different techniques have been developed [66, 67, 33]. In shallow etching technique [66], two lithographic steps (deep and shallow) are used, Fig. 3.3(a). For example, consider GaAs/InGaAs tube made by selective etching of

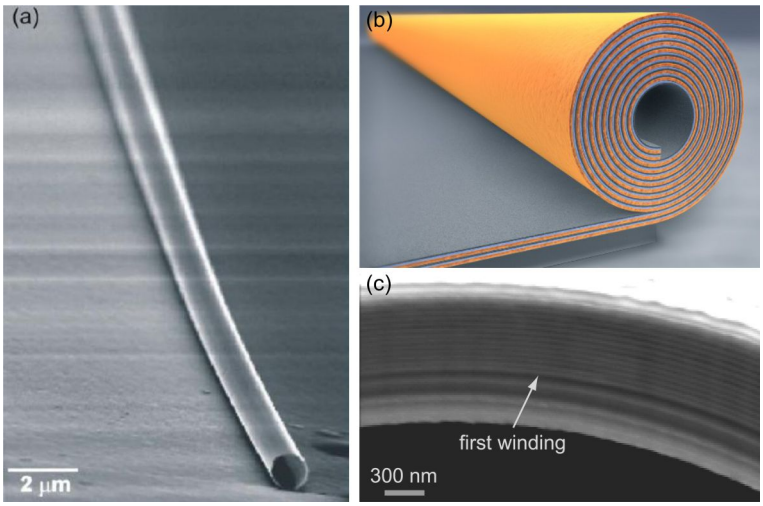

Figure 3.1: (a) Long tube with one rotation, taken from [52]. (b) Sketch of tube with many rotations needed for capacitors and (c) transmission electron micrograph of tube wall with 11 rotations. Both (b) and (c) are taken from [29].

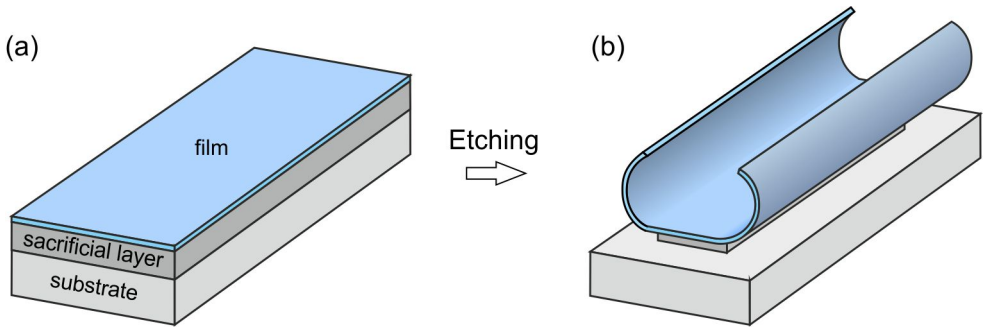

Figure 3.2: (a) Rectangular flat film pattern before etching. (b) During etching of sacrificial layer, tubes tend to form on long edges of the rectangular pattern.

AlAs on GaAs substrate. First, deep patterns are produced down to the substrate (GaAs). Second, shallow patterns are produced and top layer (GaAs) of the bilayer (GaAs/InGaAs) is removed outside of the patterned area. Etching of the sacrificial layer (AlAs) starts simultaneously from all sides of the deep mesa but the strain gradient needed for rolling-up is present only in the bilayer pattern. The bilayer also starts rolling from the shallow patterns where it has to rupture the adjacent InGaAs single layer. In similar way, anisotropic etching speed of Si (fastest for $<110>$) can be used, which makes the rolling process proceed most rapidly in the $<110>$ lateral directions [67, 68].

Tilted deposition technique is used for physical vapor deposition methods such as e-beam or thermal evaporation and sputtering deposition [33], Fig. 3.3(b). A narrow gap is created after deposition at the far end of the patterned photoresist layer due to the ballistic shadow effect and it allows etchant to enter here only. As the film starts to bend from the gap, it needs to rupture at the lateral side of the pattern, which slows down the rolling process. The same gap can be opened also for chemical vapor deposition methods by second lithographic step [33]. It is also possible to induce a specific rolling direction of a thin film by patterning a kinked trench [69] or depositing additional layers of hollow regions and interconnected hinges with differing residual stress and elastic moduli [70, 71].

In this chapter we discuss a new approach to control the tube rolling process by starting from a wrinkled film. Our approach is an alternative to overcome drawbacks of aforementioned methods, which include film rupture at pattern edges, damage by inaccurate etching and increased number of additional layers or photolithography steps involved. These nanomembranes are not limited to typical thin films but they also include two-dimensional atomic crystals such as graphene. Analogous to the macroscopic scale, where wrinkles are commonly taken to modify the elastic properties of a layered structure (e.g. cardboard paper), we assume a wrinkled film with anisotropic bending properties. We theoretically investigate the bending of such rectangular wrinkled films, taking into account variations of strain gradient, wrinkle geometries and pattern sizes. In contrast to typical rolled-up tubes formed from flat films, which bend *perpendicular* to the longer edge of rectangular patterns, we find a regime where rolling *parallel* to the long edge of the wrinkled film is favorable. A non-uniform radius of the rolled-up tube is well reproduced by elasticity theory and simulations of the film relaxation using a finite element method. Finally, experimental data are provided which confirm our theoretical predictions. Parts of this chapter have been published in [72].

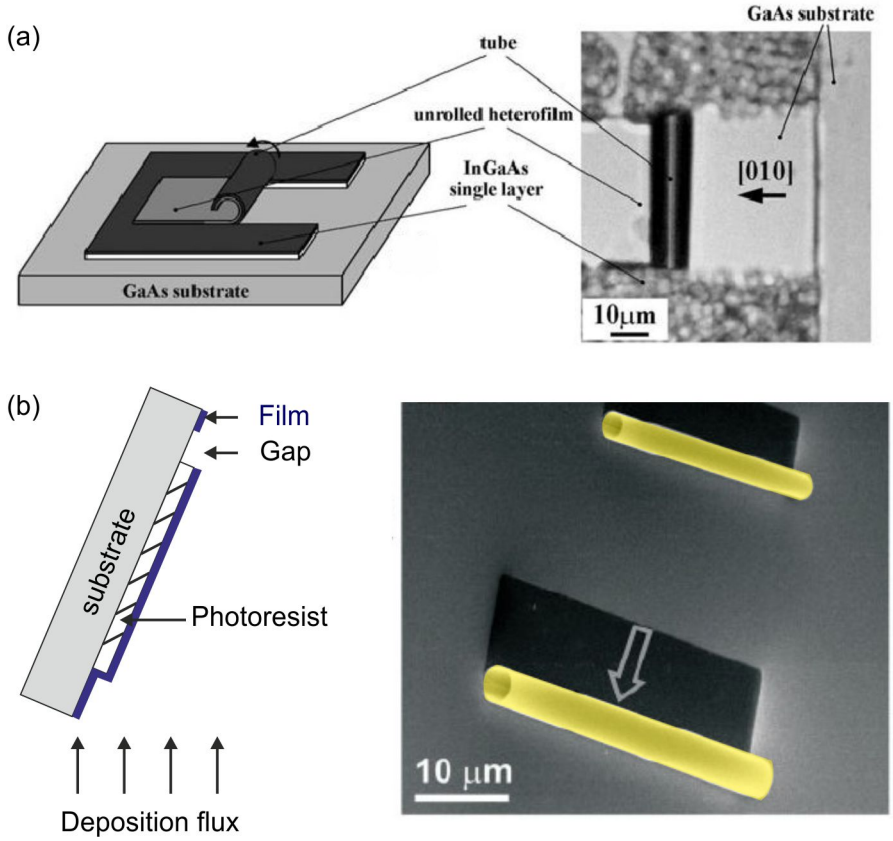

Figure 3.3: (a) Schematic of the deep and shallow lithographic patterns with rolling-up direction (left) and optical microscope image of the tube rolled-up from single pattern edge (right), taken from [66]. (b) Schematic of film angle deposition, during which gap is created due to the shadow effect (left). Rolling-up of tubes from the gap (start of arrow), where etchant can access the sacrificial layer (right). Figure re-edited from [33].

3.1 Theory

We assume a rectangular wrinkled film on sacrificial layer, as shown in Fig. 3.4(a). When the film is gradually released from its substrate by etching an underlying sacrificial layer, elastic relaxation occurs by bending and rolling-up the film either into a tube at the wrinkled edge (TWE), Fig. 3.4(b), or into a tube at the flat edge (TFE), Fig. 3.4(c). We show that bending the wrinkled edge (WE) can be efficiently suppressed by an energy barrier arising from the need to flatten the released wrinkled film during bending. The relaxation of the released part of the film, as denoted in Fig. 3.4(b,c), is described by the change in total elastic energy between the initial film and the relaxed TWE or TFE. For this purpose, we compute the change in elastic energy of the relaxed film portion on the WE and FE, followed by the computation of the total energy change of the released film area from these two contributions.

The initially rectangular wrinkled film of dimensions L_x, L_y and thickness d is approximated by a sinusoidal shape of its neutral plane, Fig. 3.4(a),

$$\zeta_0 = A\sin(kx), \tag{3.1}$$

where A, and k are the amplitude and wavenumber of the wrinkle in the x direction. We consider small slope wrinkles, where the amplitude A is much smaller than the wrinkle period $\lambda = 2\pi/k$. It is most interesting to consider a film which is longer in the wrinkle direction, i.e., x direction $(L_x > L_y)$ since wrinkling along the shorter direction (y) only enhances the tendency of the film to roll-up into that same (y) direction. The initial curvature of the wrinkled film is

$$c_0(x) \approx -Ak^2\sin(kx) = -k^2\zeta_0, \tag{3.2}$$

and the initial biaxial in-plane strain is assumed to come from depositing the film on wrinkled sacrificial layer

$$\varepsilon_{xx} = \varepsilon_{yy} = \varepsilon_0 = \bar{\varepsilon} + \frac{\Delta\varepsilon}{d}(z - \zeta_0), \tag{3.3}$$

$$\varepsilon_{xy} = 0. \tag{3.4}$$

where $\bar{\varepsilon}$ and $\Delta\varepsilon$ are average strain and strain gradient in the film, respectively. The origin of the z axis is now in the neutral plane of the film, Fig. 3.4(a). It should be noted that if the film is wrinkled after its deposition, bending strains should be

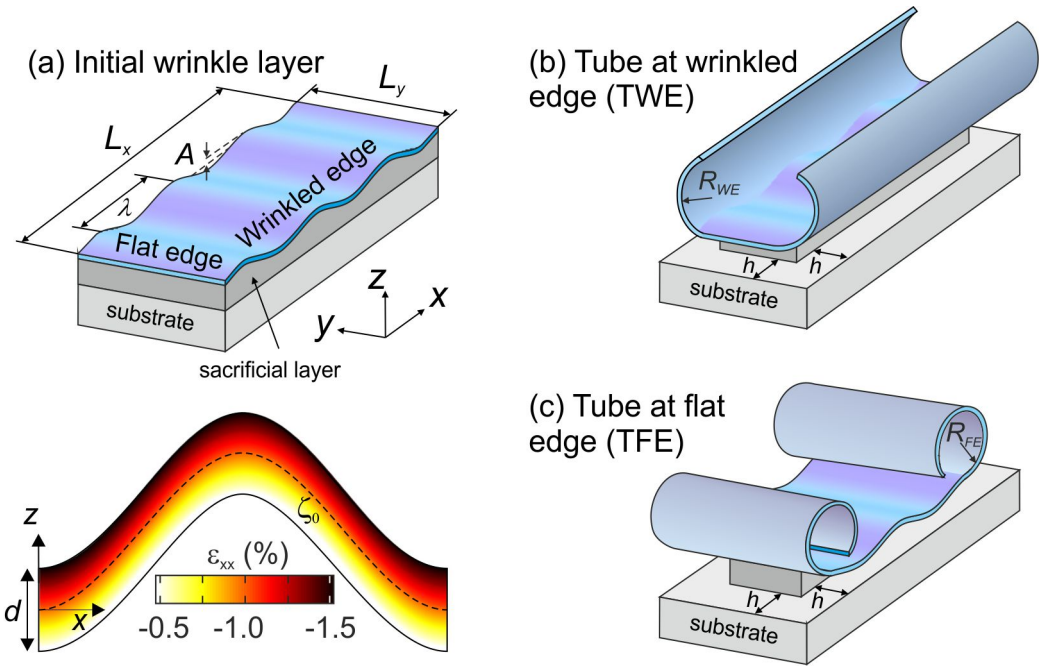

Figure 3.4: (a) Sketch of initial rectangular wrinkled film. The coordinate system (x, y, z) and notation of flat and wrinkle edges are defined. Bottom part shows initial strain in one period, eq. (3.3), for $\bar{\varepsilon} = -0.5\%$ and $\Delta\varepsilon = -1.0\%$. Upon release of the film over a length h, the film relaxes by either (b) rolling-up at the wrinkled edge with a curvature radius R_{WE} or (c) rolling-up at the flat edge with the curvature radius R_{FE}.

included (see Chapter 4, eq. (4.17)). By the Hooke's law for thin plate

$$\sigma_{xx} = \sigma_{yy} = \sigma_0 = \frac{Y\varepsilon_0}{1-\nu}. \tag{3.5}$$

Isotropic linear elastic properties of the film with Young's modulus Y and Poisson's ratio ν are assumed.

Etching the sacrificial layer leaves the film of length h on all four edges free to relax its elastic energy by bending. The bending moment (per unit film width) created by normal stress with respect to the neutral plane is derived by integrating the normal force through the thickness of the film [37]

$$M_0 = \int_{\zeta_0 - d/2}^{\zeta_0 + d/2} \sigma_0 (z - \zeta_0) \mathrm{d}z = \frac{(1+\nu) D \Delta\varepsilon}{d} \tag{3.6}$$

and it is equal for WE and FE. We also define bending moment vector in the initial configuration $\boldsymbol{M_0} = (-M_0, -M_0)$. The bending rigidity D of the flat film is given in eq. (1.9). The bending (roll-up) radius of the flat film portion R_0 due to the bending moment M_0 can be calculated by the classical expression for pure bending of a thin plate [12, 73]

$$R_0 = \frac{D}{M_0} = \frac{d}{(1+\nu)\Delta\varepsilon} \tag{3.7}$$

in agreement with experimental studies [8, 39] and bending radius due to Timoshenko eq. (2.2) [36, 37]. The corresponding curvature of rolled-up tube is

$$g_0 = \frac{1}{R_0}. \tag{3.8}$$

We evaluate the change in elastic energy of the released film portion undergoing attenuation of wrinkles and transition to the rolled-up state (in y direction) by a simple bistability model [74]. The curvature of the film is separated into a 'local' wrinkle curvature $c(x)$ and a 'global' average curvature g of the film. These two curvatures interplay and cause significant stretching strains, in addition to bending strains. However, it is possible to include stretching strains by considering the wrinkled membrane as equivalent flat membrane with anisotropic effective stiffness altered by wrinkles [75].

We assume that the local curvature of wrinkle $c(x)$ remains sinusoidal during wrinkle attenuation and transition to rolled-up tube. We also assume that wrinkle period λ does not change and local curvature $c(x)$ stays in phase with initial local

curvature $c_0(x)$ and therefore

$$c(x) = (1 - \gamma)c_0, \tag{3.9}$$

where γ is wrinkle attenuation parameter. The value of the wrinkle attenuation parameter $\gamma = 0$ corresponds to the initial wrinkle with local curvature c_0 and global curvature $g = 0$. The value $\gamma = 1$ denotes a film that is locally flat $c = 0$, but can be globally curved $g \neq 0$.

Alternative formulas for bending energy of the anisotropic film will be needed [74]. We define curvature and bending moment vectors

$$\boldsymbol{\kappa} = (\kappa_{xx}, \kappa_{yy}) \tag{3.10}$$

and

$$\boldsymbol{M} = (-M_{xx}, -M_{yy}) \tag{3.11}$$

with minus sign to deal with positive values of global curvature, respectively, which are connected by the bending rigidity (stiffness) matrix

$$\boldsymbol{D} = D \begin{pmatrix} 1 & \nu \\ \nu & 1 \end{pmatrix}, \tag{3.12}$$

$$\boldsymbol{M} = \boldsymbol{\kappa}\boldsymbol{D}. \tag{3.13}$$

The bending energy density is given by

$$u_b = \int_{\mathbf{0}}^{\boldsymbol{\kappa}} \left(\boldsymbol{M}^{\boldsymbol{T}} + \boldsymbol{M}_{\mathbf{0}}^{\boldsymbol{T}}\right) \mathrm{d}\boldsymbol{\kappa} = \frac{1}{2}\boldsymbol{\kappa}^{\boldsymbol{T}}\boldsymbol{D}\boldsymbol{\kappa} + \boldsymbol{M}_{\mathbf{0}}^{\boldsymbol{T}}\boldsymbol{\kappa}, \tag{3.14}$$

where superscripted ^{T} means transpose and the first term corresponds to bending energy density we have shown previously in eq. (1.8). It's worth noting that stretching energy will be included with the effective stiffness of wrinkled film in next paragraph. The initial total curvature of wrinkled film before release can be written in vector notation as

$$\boldsymbol{\kappa_0} = (c_0(x), 0). \tag{3.15}$$

3.1.1 Rolling-up on wrinkled edge

Let us consider rolling up of portion A on wrinkled edge, Fig. 3.5(a). The actual curvature during the wrinkle attenuation process is $\boldsymbol{\kappa}_{WE} = (c(x), g_{WE})$, where $c(x) =$

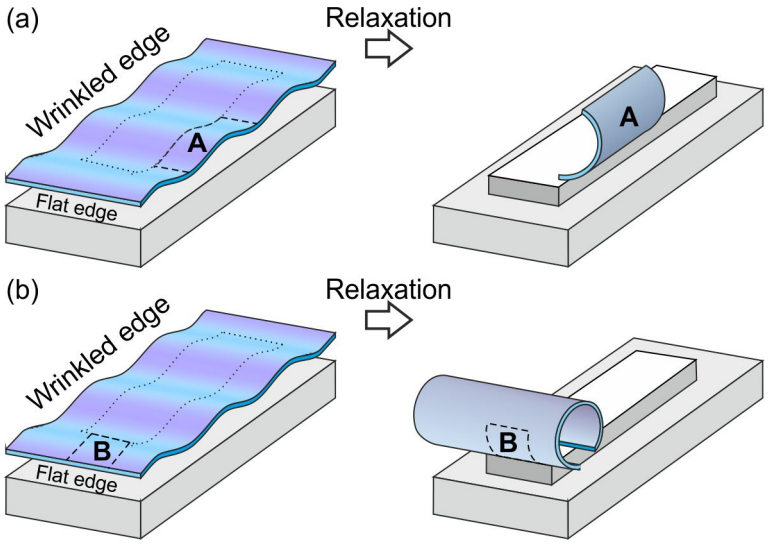

Figure 3.5: Schematic of relaxation of film portion on (a) wrinkled and (b) flat edge of rectangular pattern. In the left column, situation after etching some length but before relaxation of initial strain is depicted. In the right column, rolled-up shape of film after relaxation is shown.

$(1-\gamma)c_0(x)$. Note that even for $\gamma = 0$ there is some global curvature g_{WE}. The change in the total curvature during rolling-up of wrinkled film portion A between these two states is

$$\boldsymbol{\Delta\kappa}_{WE} = \boldsymbol{\kappa} - \boldsymbol{\kappa_0} = (-\gamma c_0(x), g_{WE}). \tag{3.16}$$

The effective stiffness of wrinkled film is increased in y direction [75]

$$\boldsymbol{D} = D \begin{pmatrix} 1 & \nu \\ \nu & 1+\alpha_\gamma \end{pmatrix}, \tag{3.17}$$

where the factor

$$\alpha_\gamma = 6(1-\nu^2)(1-\gamma^2)\frac{A^2}{d^2} \tag{3.18}$$

includes contribution from the different bending rigidity along the sinusoidal wrinkle (contour). Change in the bending energy (we omit superscript $_b$ in the following) of the film from eqs. (3.14) and (3.16) is

$$u_{WE} = -M_0\left(g_{WE} + c_0(x)\gamma\right) + \frac{D}{2}\left[(1+\alpha_\gamma)g_{WE}^2 + \gamma^2 c_0^2(x) - 2c_0(x)\gamma k\nu\right]. \tag{3.19}$$

The average change in elastic energy density of the wrinkled film per period caused by the curvature change $\boldsymbol{\Delta\kappa}_{WE}$ is given by

$$\bar{u}_{WE} = \frac{1}{\lambda}\int_0^\lambda u_{WE}\mathrm{d}x = -M_0 g_{WE} + \frac{D}{2}\left[(1+\alpha_\gamma)g_{WE}^2 + \frac{\gamma^2}{2}(Ak^2)^2\right], \tag{3.20}$$

where we have used

$$\int_0^\lambda c_0(x)\mathrm{d}x = 0, \tag{3.21}$$

and

$$\int_0^\lambda c_0^2(x)\mathrm{d}x = \frac{(Ak^2)^2}{2}. \tag{3.22}$$

Equilibrium with respect to g_{WE} is obtained from stationary condition

$$\frac{\mathrm{d}\bar{u}_{WE}}{\mathrm{d}g_{WE}} = 0, \tag{3.23}$$

which gives

$$g_{WE,Eq}(\gamma) = \frac{M_0}{D(1+\alpha_\gamma)}. \tag{3.24}$$

If the wrinkles are almost fully attenuated ($\gamma = 1$), the radius of the tube at the WE is given by the reciprocal value of the equilibrium curvature

$$R_{WE} = \frac{1}{g_{WE,Eq}(1)} = R_0. \tag{3.25}$$

Inserting this equilibrium curvature into eq. (3.20), we obtain

$$u_{WE}(\gamma) \equiv \bar{u}_{WE,Eq} = -\frac{M_0^2}{2D(1+\alpha_\gamma)} + \frac{1}{4}D\gamma^2(Ak^2)^2 \tag{3.26}$$

To simplify the notation, we introduced $u_{WE}(\gamma)$, which is a function of γ.

We numerically identify three characteristic energy regimes of $u_{WE}(\gamma)$ as shown in Fig. 3.6 :

1. i.e. for $A = 120\,\mathrm{nm}$ and $\Delta\varepsilon = 0.1\%$, energy decreases monotonically to its minimum $\gamma = 1$ as the film rolls up at WE.

2. i.e. for $A = 500\,\mathrm{nm}$ and $\Delta\varepsilon = 0.1\%$, energy first increases (energy barrier), but then decreases to a minimum at $\gamma \approx 1$.

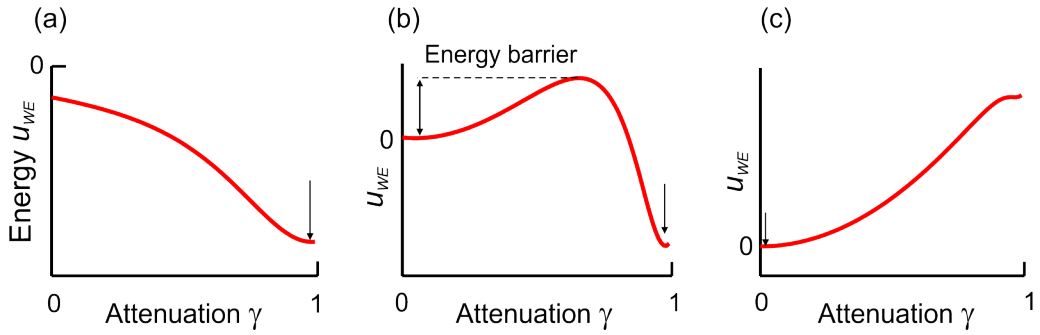

Figure 3.6: Three types of energy landscape $u_{WE}(\gamma)$ during attenuation of wrinkles γ and rolling-up to tube on wrinkled edge (TWE). (a) $A = 120\,\mathrm{nm}$ and $\Delta\varepsilon = 0.1\%$, (b) $A = 500\,\mathrm{nm}$ and $\Delta\varepsilon = 0.1\%$, (c) $A = 500\,\mathrm{nm}$ and $\Delta\varepsilon = 0.02\%$. Arrows show position of minima.

3. i.e. for $A = 500\,\mathrm{nm}$ and $\Delta\varepsilon = 0.02\%$, energy only increases during wrinkle attenuation. Minimum is at $\gamma = 0$.

These regimes are used when considering the total energy change in Section 3.1.3. A film thickness $d = 70\,\mathrm{nm}$ and a wrinkle period $\lambda = 40\,\mu\mathrm{m}$ are considered in the following. These parameters were chosen in view of our experimental result shown in Section 3.3. Elastic properties of CuNi alloy (Constantan) are assumed $Y = 162\,\mathrm{GPa}$, $\nu = 0.33$ [76].

3.1.2 Rolling-up on flat edge

Rolling of the film portion B at the FE is now considered, Fig. 3.5(b). The curvature in x direction is assumed to change abruptly from the initial curvature $c_0(x)$ to the curvature of the rolled-up tube g_{FE} (reciprocal of radius: R_{FE}), therefore $\boldsymbol{\Delta\kappa_{FE}} = (g_{FE} - c_0(x), 0)$. The resulting change in the local bending energy of the film from eq. (3.14) is

$$u_{FE} = -M_0 \left[g_{FE} + k^2\zeta_0 - \frac{R_0\left(g_{FE} + k^2\zeta_0\right)^2}{2} \right], \tag{3.27}$$

where we have used eq. (3.2) for curvature of wrinkled film. The equilibrium with respect to global curvature g_{FE}

$$\frac{\mathrm{d}u_{FE}}{\mathrm{d}g_{FE}} = 0 \tag{3.28}$$

leads to the dependence of the tube curvature radius on the reference coordinate x

$$g_{FE,Eq}(x) = g_0 \left(1 - R_0 k^2 A \sin(kx)\right) \tag{3.29}$$

with the corresponding energy

$$u_{FE,Eq} = -\frac{M_0^2}{2D} \equiv u_{FE}. \tag{3.30}$$

Since $u_{FE} < 0$, rolling-up TFE is always energetically favorable as compared to the unrolled film.

3.1.3 Total energy balance

Up to here, we considered portions A or B of the released film bending at WE or FE. We can now consider the change in total elastic energy of the whole released film (consisting of four edges) and the competition between TWE and TFE. Note that we do not consider relaxation at the corners in this simplification. If TWE is to prevail, we can approximate that the film on the FE is unrelaxed and therefore its energy does not change ($u = 0$), see Fig. 3.7(a), and therefore the total energy change originates only from the rolling at the WE,

$$U_{WE} = 2u_{WE}(1)L_x h, \tag{3.31}$$

where h is the etching length. If TFE should prevail, we approximate that the film at the WE is unrelaxed and the relaxation comes only from the rolling at the FE, Fig. 3.7(b)

$$U_{FE} = 2u_{FE}L_y h. \tag{3.32}$$

The minimum from U_{WE} and U_{FE} will determine the energetically favorable morphology.

In the regime left of the solid curve in Fig. 3.8, the energy change u_{WE} typically decreases with increasing γ and the minimum point is near $\gamma = 1$ (arrow in the inset). The rolling is preferred energetically at the WE when it releases more energy, $U_{WE} < U_{FE}$, and thus we obtain a condition for the aspect ratio of the stripe

$$\frac{L_y}{L_x} < 1 - \frac{\left(R_0 k^2 A\right)^2}{2}, \tag{3.33}$$

for which the tube rolls up from the WE. This ratio is always smaller than 1 and equals zero for $A_{\max} = \frac{\sqrt{2}}{R_0 k^2}$. Therefore, beyond this maximum wrinkle amplitude,

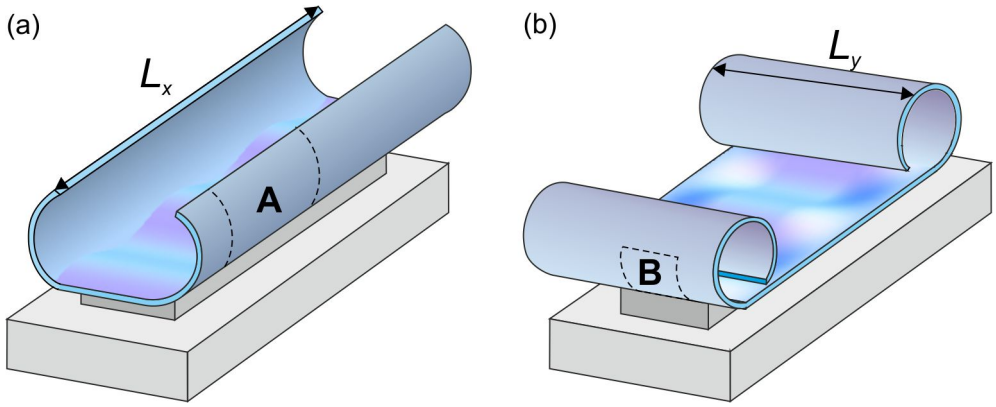

Figure 3.7: Sketch of relaxed film for (a) tube on wrinkled edge (TWE) and (b) tube on flat edge (TFE). Portions A and B at the wrinkled and flat edge are denoted.

one cannot find any aspect ratio L_y/L_x to make TWE energetically preferable.

In the regime below the dashed curve in Fig. 3.8, forming TWE would require an increase of energy to $U_{WE} \sim u_{WE}$ (inset), which is not energetically favorable. In contrast, TFE can be formed since the energy $U_{FE} < 0$ is released. The TWE is equal in energy to the initial wrinkled film (dashed curve in Fig. 3.8) for

$$u_{WE}(0) = u_{WE}(1), \tag{3.34}$$

which means

$$-\frac{M_0^2}{2D} + \frac{1}{4}D(Ak^2)^2 = -\frac{M_0^2}{2D(1+\alpha_1)}. \tag{3.35}$$

By using eq. (3.6) we are able to express

$$\Delta\varepsilon_{dash} = \frac{2\pi^2 d^2}{\lambda^2(1+\nu)}\sqrt{\frac{1+6(1-\nu)^2A^2/d^2}{3(1-\nu^2)}}, \tag{3.36}$$

which for $A \gg d$ results in the scaling $\sim Ad/\lambda^2$ for the phase boundary of these regions.

Between the solid and dashed curves, the film at the WE has to increase its energy from $u_{WE}(0)$ to the maximum of $u_{WE}(\gamma)$ (and also the total energy) to progress into the rolled-up state near $\gamma = 1$(arrow) (see upper right inset of Fig. 3.8). Under equilibrium conditions, the film cannot overcome this energy barrier and change its shape without some external forces. Therefore TWE is suppressed and TFE is formed, because $U_{FE} < 0$. It should be noted that even though the final shape is the same (TFE) as below the dashed curve, the film might be snapped to the second stable TWE state by external forces, which can be generated for instance

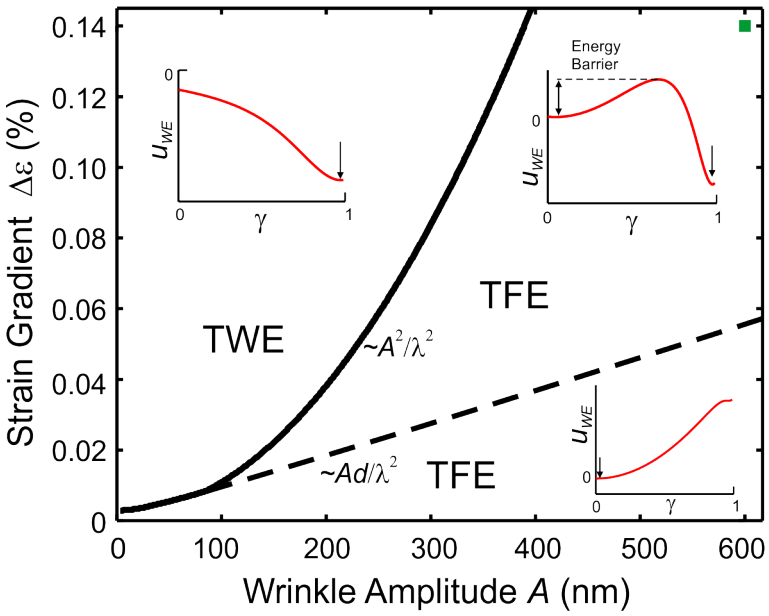

Figure 3.8: Phase diagram of tube shapes after release of a rectangular patterned wrinkled film as a function of wrinkle amplitude A and initial strain gradient $\Delta\varepsilon$. Insets show the elastic energy change $u_{WE}(\gamma)$ as a function of wrinkle attenuation parameter γ. Our experimental result from Fig. 3.15 is shown as a green data point in the upper right corner. Properties of $Cu_{0.59}Ni_{0.40}Mn_{0.01}$ from experimental Section 3.3 are used, $d = 70\ \mathrm{nm}$ and $\lambda = 40\ \mu\mathrm{m}$. Scaling of the dividing curves is also indicated.

during the fabrication process (e.g., capillary forces, flowing pressure).

The solid curve in Fig. 3.8 separates the region without energy barrier on the left from that with an energy barrier on the right and it scales as $\sim A^2/\lambda^2$, obtained by fitting the curve for fixed $d = 70\text{nm}$ within range $A = 10-500\text{nm}$ and $\lambda = 5-40\mu\text{m}$ [1]. Interestingly, this scaling is thickness independent and varies only with wrinkle parameters A, λ. For a given strain gradient, i.e. $\Delta\varepsilon = 0.1\%$ in Fig. 3.8, there exists a minimum wrinkle amplitude $A = 330$ nm for suppressing the rolling at the WE (solid curve).

3.1.4 Application to carbon nanoscrolls

It is known that graphene shows intrinsic ripples with ∼1 nm amplitude and 5-10 nm period [77], which are believed to overcome the intrinsic thermodynamic instability of a 2D crystal. Recently, also mechanical properties of extrinsically corrugated graphene were measured [78] and its conformity to substrate was theoretically investigated [79, 80, 81, 82]. Rolling-up of flat graphene sheet into carbon nanoscroll was reported [34, 57] and therefore rolling-up corrugated graphene sheet might be not far in the future.

Therefore we considered scrolling of a wrinkled graphene sheet within our continuum elasticity approach, neglecting its atomic thickness for simplicity. Based on recent experiments [83, 34, 57], approximate radius of carbon nanoscrolls is $R_0 = 30\text{nm}$ and effective graphene thickness $d = 0.34$ nm, which leads to an effective strain gradient $\Delta\varepsilon = 1.1\%$ from eq. 3.7 (omitting the Poisson ratio for simplicity). With the same calculation which produced Fig. 3.8 and graphene Young modulus $Y = 340$ GPa [84, 85], we predict that for corrugation period $\lambda = 2\ \mu$m [78] wrinkling with an amplitude ∼60 nm can suppress scrolling from the wrinkled graphene edge, Fig. 3.9.

It is know that properties of carbon nanotubes (e.g. electrical conductivity) depend on the way their structure corresponds to rolling-up of graphene sheet at an chiral angle [86]. Carbon nanoscrolls with various chirality were observed [83, 87]. By defining the graphene corrugations at given angle to the graphene lattice, it should be feasible to obtain carbon nanoscrolls with desirable chirality.

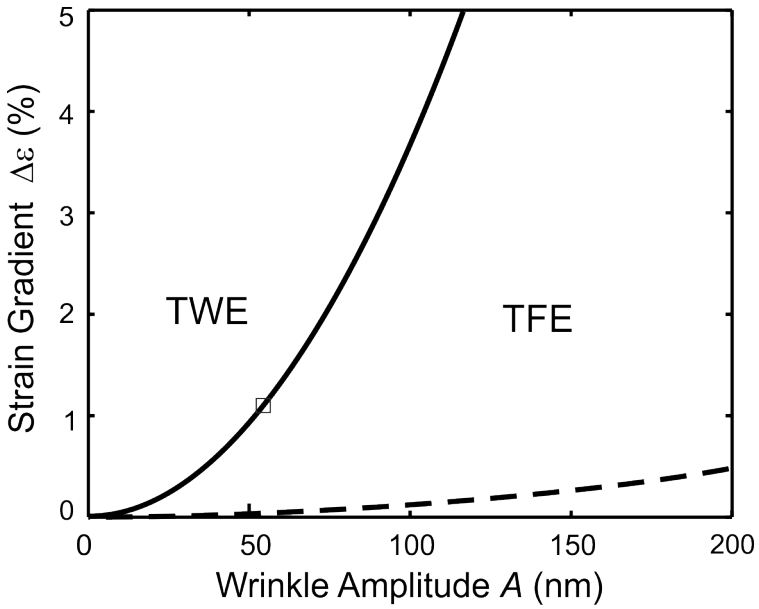

Figure 3.9: Phase diagram of carbon nanoscroll (tube) shapes after release of a rectangular corrugated graphene as a function of wrinkle amplitude A and initial strain gradient $\Delta\varepsilon$, for $\lambda = 2\,\mu\mathrm{m}$. Square mark denotes the transition between TWE and TFE for $\Delta\varepsilon = 1.1\%$ mentioned in text.

3.2 Finite element study

To confirm that our analytical eq. (3.29) is suitable to describe the curvature of the TFE, we used numerical finite element method with large deformations [88] (Structural Mechanics Module) to compute the elastic relaxation of the strained wrinkled film. For simplicity, we use a 2D cross-section of the film with plane strain condition and numerically solve the mechanical equilibrium equations [12] for displacements u_x and u_z ($u_z = \zeta$) in general form

$$\frac{\partial \sigma_{xx}}{\partial x} = 0, \; \frac{\partial \sigma_{xz}}{\partial x} = 0, \tag{3.37}$$

$$\frac{\partial \sigma_{zx}}{\partial z} = 0, \; \frac{\partial \sigma_{zz}}{\partial z} = 0. \tag{3.38}$$

Large deformation strains are

$$\varepsilon_{xx} = \varepsilon_0 + \frac{\partial u_x}{\partial x} + \frac{1}{2}\left(\frac{\partial u_z}{\partial x}\right)^2, \tag{3.39}$$

[1]The analytical formula does not exist in general, because it is a root of fifth order polynomial

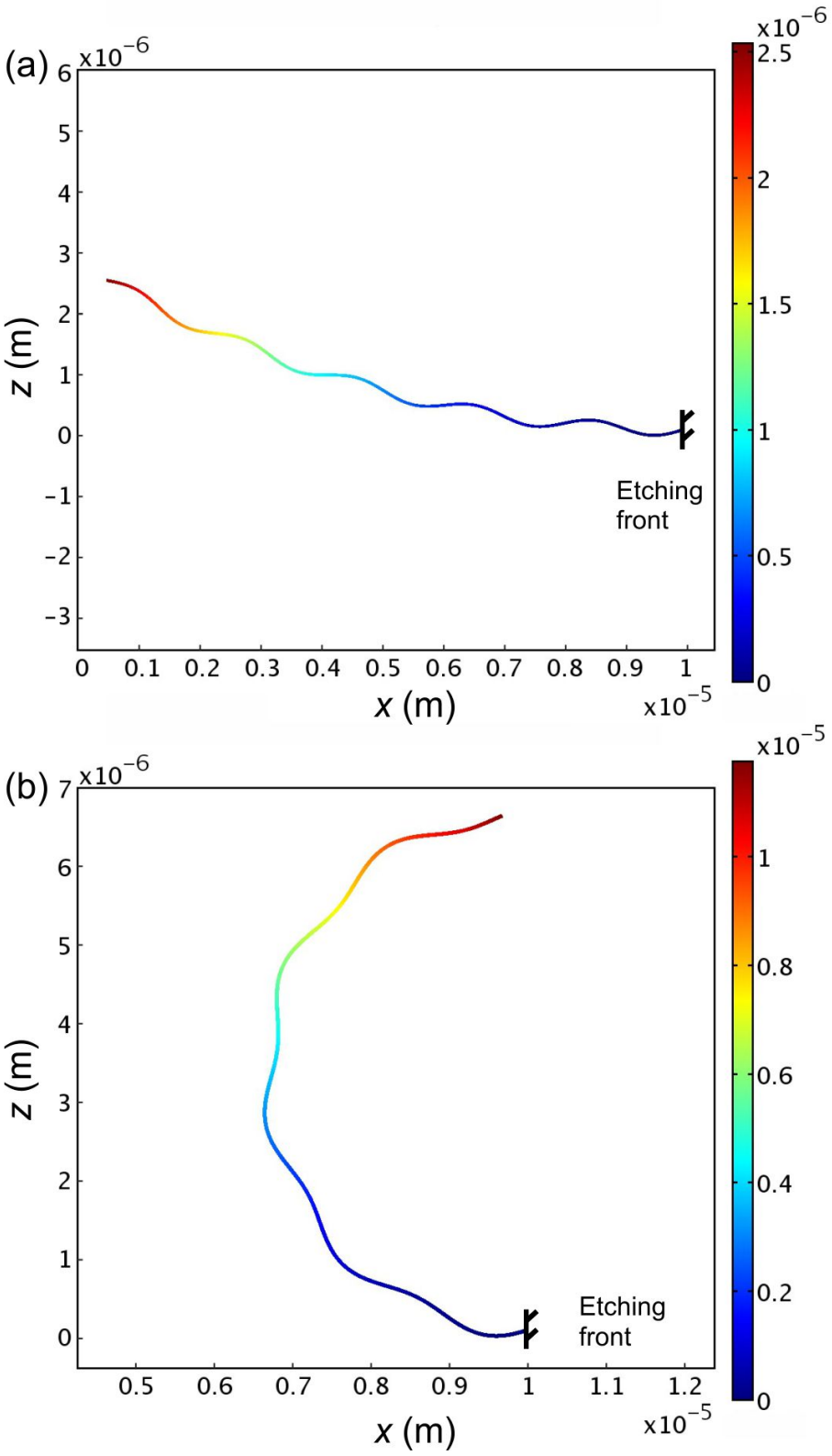

Figure 3.10: Numerical calculation of deformation during rolling of the wrinkled film from the flat edge, (a) $\Delta\varepsilon = 0.2\%$ and (b) $\Delta\varepsilon = 1.2\%$. Initial wrinkle shape $A = 100\,\mathrm{nm}$, $\lambda = 2\,\mu\mathrm{m}$ and $d = 50\,\mathrm{nm}$, $Y = 330\,\mathrm{GPa}$ and $\nu = 0.3$.

$$\varepsilon_{zz} = -\frac{2\nu}{1-\nu}\varepsilon_0 + \frac{\partial u_z}{\partial z} + \frac{1}{2}\left(\frac{\partial u_z}{\partial z}\right)^2, \tag{3.40}$$

$$\varepsilon_{xz} = \varepsilon_{zx} = \frac{1}{2}\left(\frac{\partial u_x}{\partial z} + \frac{\partial u_z}{\partial x} + \frac{\partial u_x}{\partial z}\frac{\partial u_z}{\partial x}\right), \tag{3.41}$$

where we used initial strain ε_0 in x and $-\frac{2\nu}{1-\nu}\varepsilon_0$ in z (eq. (1.6) with $\varepsilon_y = \varepsilon_0$, 2D plane strain). Stresses are related to strains by Hooke law

$$\sigma_{xx} = \frac{Y}{1+\nu}\left[\varepsilon_{xx} + \frac{\nu}{1-2\nu}\left(\varepsilon_{xx} + \varepsilon_{zz}\right)\right], \tag{3.42}$$

$$\sigma_{zz} = \frac{Y}{1+\nu}\left[\varepsilon_{zz} + \frac{\nu}{1-2\nu}\left(\varepsilon_{xx} + \varepsilon_{zz}\right)\right], \tag{3.43}$$

$$\sigma_{xz} = \frac{Y}{1+\nu}\varepsilon_{xz},\ \sigma_{zx} = \frac{Y}{1+\nu}\varepsilon_{zx}. \tag{3.44}$$

We considered five periods of the wrinkled film for the simulation. The mesh consisted of 292 triangular elements. Rather than dynamically removing the sacrificial layer and releasing the film gradually [89], we assume that all sacrificial layer is removed before start of the simulation and the initial biaxial strain eq. (3.3) in the film is linearly increased in steps of 0.02% to the final value (parametric study). The wrinkled film is fixed at the etching front boundary and free elsewhere.

Relaxed bent shapes can be seen for incomplete rotation on Fig. 3.10 and almost complete tube rotation on Fig. 3.11(a). The normalized curvature g_{FE}/g_0 is extracted from the relaxed shape and it compares very well to eq. (3.29), Fig. 3.11(b). Even though the normalized curvature oscillates around the curvature of the flat film g_0 and can be even negative in some intervals, the overall shape of the relaxed film is still tubular with an average curvature R_0. By proper design of the wrinkle profile, which matches the circumference of the tube to the integer multiple (l) of period

$$2\pi R_0 = l\lambda, \tag{3.45}$$

one can obtain new wrinkled tube structures with varying curvature along circumference, eq. (3.29), Fig. 3.12. If rolled-up from epitaxial layers, these structures might enlarge radial crystal lattices [90] with wrinkled radial lattices. Strain in these structures is not uniform along the circumference and might cause interesting electronic and optical properties, compare with Chapter 4. Optical confinement and whispering gallery modes in microtubes [91, 92] will be also changed. The mechanical stiffness

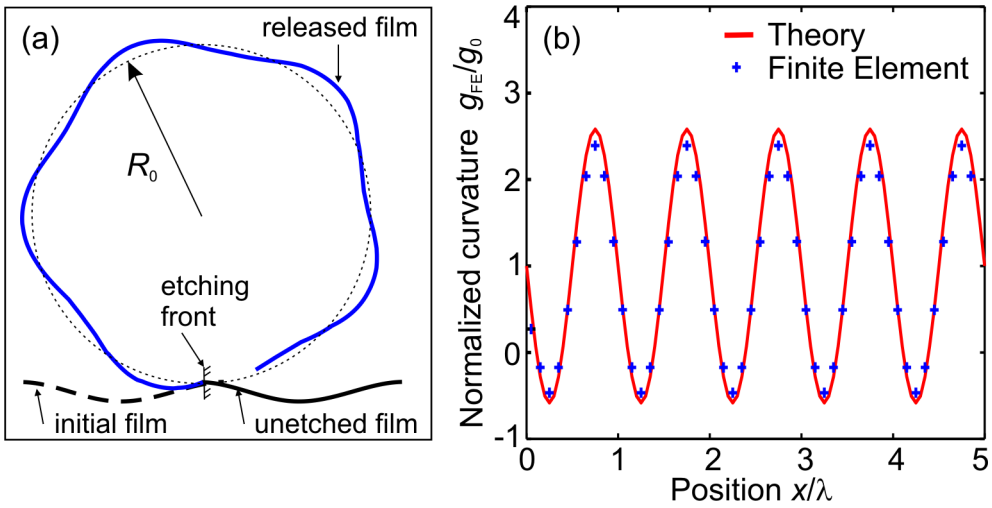

Figure 3.11: Finite element study of rolling the wrinkled film from the flat edge with 5 wrinkle periods, $\Delta\varepsilon = 2.4\%$, $A = 100\,\mathrm{nm}$ and $\lambda = 2\,\mu\mathrm{m}$. (a) Almost complete rotation of the released film with non-uniform tubular shape (solid blue line) and uniform tube (dashed line) as a guide to the eyes. (b) Curvature of the tube in (a), where the solid red line corresponds to the theoretical calculation using eq. (3.29) and blue marks show the results extracted from finite element calculations in (a).

of wrinkled tube structures will be also larger due to the anisotropic bending rigidity of wrinkled tube wall, similarly to eq. (3.18). Interestingly, related phenomena were also observed for geodesic curvature of plant leaves [41, 42].

3.3 Experiment

In order to qualitatively confirm theoretical predictions for rolling direction of wrinkled films from Section 3.1.3, we carried out rolling experiments with metallic wrinkled films on photoresist sacrificial layer. This was exception from theoretical focus of my

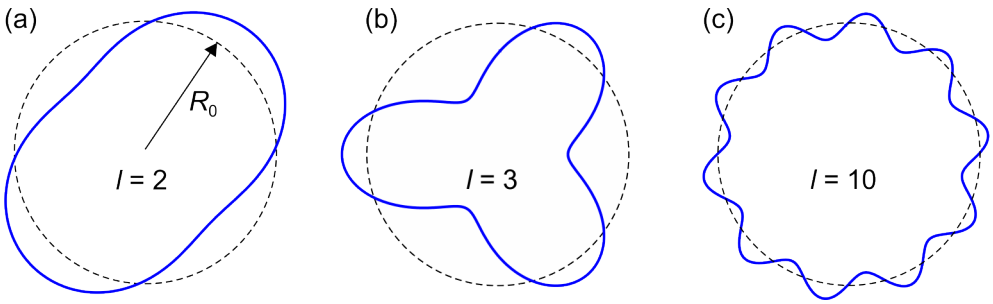

Figure 3.12: Wrinkled tube shapes with different number of periods l for one rotation, (a) $l = 2$, (b) $l = 3$, (a) $l = 10$.

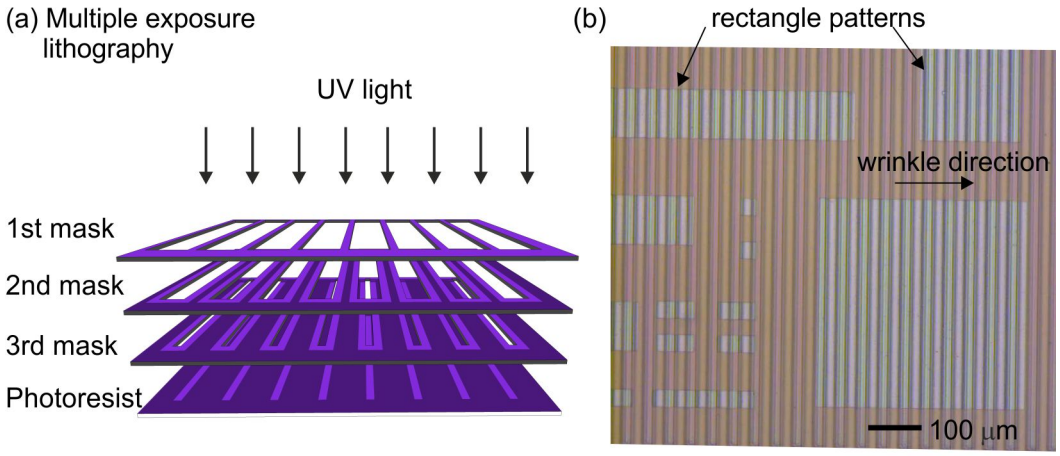

Figure 3.13: (a) Schematic of multiple exposure lithography. (b) Optical microscope image of wrinkled rectangular patterns of different dimensions.

work.

3.3.1 Fabrication of wrinkled films

In the last decade, a plenty of techniques to fabricate microscale wrinkled patterns have appeared in reviews [93, 94, 95], such as buckling of patterned films on elastomer substrate [5], uniaxial stretching of sheets [93, 96], chemical patterning of substrates with regions of high and low adhesion [97], or bonding of semiconductor membranes to prestrained elastomer [7, 98]. Recently, also metallic thin films were deposited on wrinkled resin layer [99].

We have chosen a technique similar to gray-scale lithography [100] and fabricated wrinkled photoresist surfaces by multiple exposure steps, Fig. 3.13. In the first lithographic step, Dr. I. Mönch has deposited alignment marks on thermally oxidized Si wafer and spin-coated ARP-3510 photoresist (Allresist GmbH, Germany) at 3500 min^{-1} for 35 s (2.5 μm thickness) and heated photoresist at 95°C for 1 min. Then the wafer was exposed for 1 s with a set of stripe masks with increasing width from 5 to 25 μm to enforce different total exposure and depth profile in the photoresist. Developing was done in AR300-35 for 1 min. Two kinds of wrinkle profiles, sinusoidal 'sin' and 'step' with a period of 40 μm, together with a flat profile for comparison were fabricated. The metallic $Cu_{0.59}Ni_{0.40}Mn_{0.01}$ alloy films with thicknesses of $d = 70$ nm or $d = 100$ nm ($\pm$5 nm) were deposited by Dr. J. Schumann on top of the wrinkled photoresist by magnetron sputtering at room temperature (source power 500 W, pre-deposition pressure $2 \cdot 10^{-4}$ Pa, sputtering pressure 0.3 Pa). The morphology of the

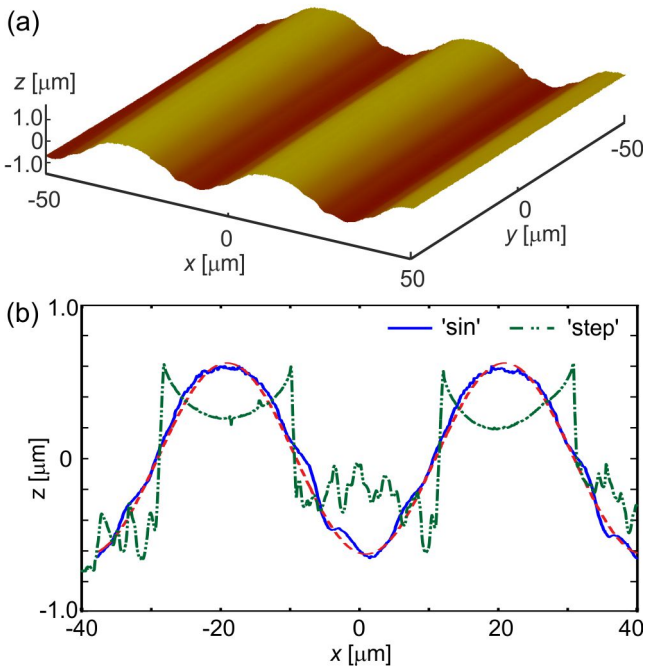

Figure 3.14: (a) Perspective view AFM image of the wrinkled film. (b) Cross-sectional AFM profiles of the 'sin' pattern (taken from the map in (a), solid blue line) and of the 'step' pattern (dash-dotted green line). The sinusoidal profile obtained from the best fit is also shown as a dashed red line.

wrinkled film is characterized by atomic force microscopy (AFM) as shown by the perspective view AFM image and cross-section profile in Fig. 3.14. The measured 'sin' profile is well fitted by a sinusoidal function with an amplitude of 600 nm. A second lithographic step was performed to fabricate rectangles of varying aspect ratios 1:1, 1:2, 1:4 and 1:5 with approximate dimensions $40\times\{40, 80, 200\}$, $100\times\{100, 200, 500\}$, $200\times\{200, 400, 800\}$ and $400\times\{400, 800\}$ μm^2.

3.3.2 Observation of rolling-up

The samples with rectangular flat and wrinkled films were covered by droplets of N-methyl-2-pyrrolidone in order to gradually remove the sacrificial photoresist layer. After putting the liquid onto the sample, the microscope objective lens were refocused within few seconds and recording of the film releasing process was started[2]. Therefore, the recording time in movies [72, 101] might be shifted 20 seconds from the start of etching process.

[2]The software program used to record movies had memory limitation and therefore most videos were recorded only after refocusing.

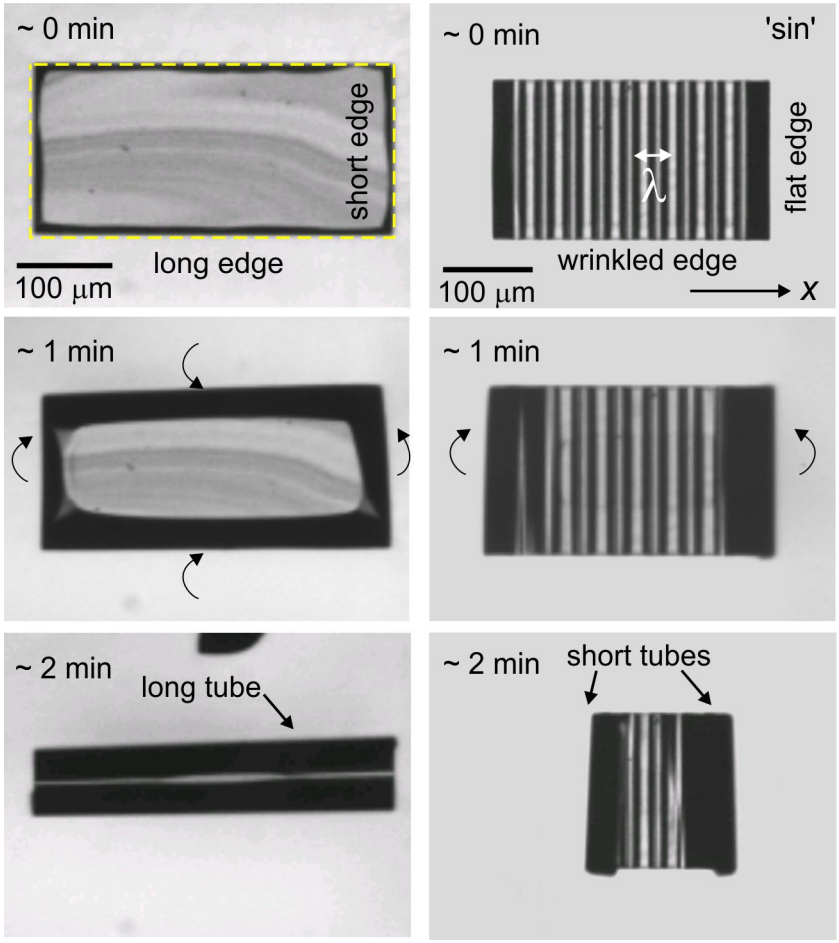

Figure 3.15: Snapshots from optical microscopy video during release of the flat film pattern (left column) and a wrinkled 'sin' film pattern (right column) with dimension 200x400 μm^2 after $\sim 0, 1, 2$ minutes etching (from top to bottom), thickness $d = 70$ nm. Bending film has dark black color, arrow in middle row indicates bending direction and pattern edge is dashed yellow. Movies of figures can be found in Supporting Information [72].

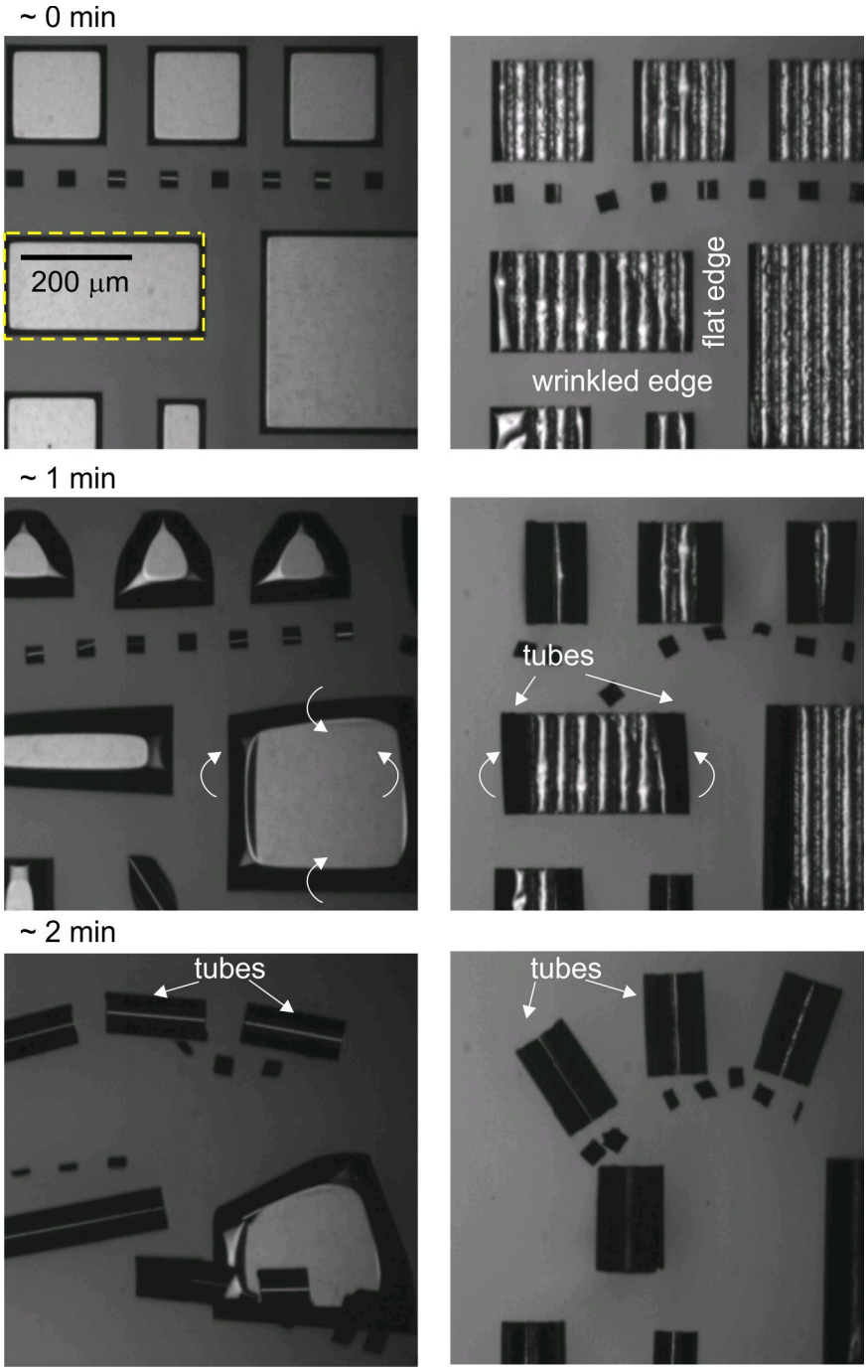

Figure 3.16: Snapshots from optical microscopy video during release of the flat pattern array (left column) and wrinkled 'step' pattern array (right column) after $\sim 0, 1, 2$ minutes etching (from top to bottom), film thickness $d = 70\,\mathrm{nm}$. Bending film has dark black color, arrow in middle row indicates bending direction and pattern edge is dashed yellow. Movies of the figures can be found in [101].

Etching of the single flat and wrinkled film pattern are shown for comparison in Fig. 3.15. The flat film initially bends at all four edges and as etching proceeds, roll-up of the longer edge prevails and single tube with axis along the long pattern edge forms. The strain gradient in the deposited film was estimated from the average radius of the tubes from the flat film measured in the etchant liquid after total release, $R_0 = 36 \pm 5\ \mu\mathrm{m}$, which directly yields $\Delta\varepsilon = -0.14 \pm 0.02\%$ from eq. (3.7). In contrast, the wrinkled film with the 'sin' profile starts to bend preferentially at the flat edges without any noticeable bending at the wrinkled edges and finally the tube is formed along the flat edge. Taking the computed strain gradient and wrinkle amplitude of 600 nm measured by AFM, Fig. 3.14, we see that the observed rolling direction is in agreement with our phase diagram in Fig. 3.8 (marked by the square). The tubes which rolled from the wrinkled film apparently experience a larger radius (51±5 μm) than the tubes rolled from the flat film (36±5 μm). We explain this observation by the inhomogeneous tube radius as predicted in eq. 3.29.

For overview of behavior on larger area, we also show rolling-up of patterns with different aspect ratios, Fig. 3.16. All flat patterns start to roll from all four edges at the beginning but continue so only for square patterns. Rolling on long edge prevails for rectangular patterns. The wrinkled patterns with 'step' profile form tubes along the flat edge of the pattern, perpendicular to the tubes from flat film and in agreement with also with Fig. 3.15. Therefore, at our experimental conditions, the functional form of the wrinkle profile can be varied without any significant effect on the control of the rolling direction. From the observed rolling of more than 100 rectangular wrinkled patterns, all roll-up from the flat edge.

3.4 Conclusion

We used anisotropic bending rigidity of wrinkled film to suppress rolling-up on wrinkled film edge and favor rolling-up on flat edge of the film. Thus rolling direction can be predefined by introducing uniform wrinkles in the film. With the theory of plates, we computed the change in elastic energy during shape transition from wrinkled film to rolled-up tube. Two scenarios for release of rectangular pattern were considered : (i) tube formed at the flat pattern edge and (ii) tube formed at wrinkled pattern edge. The relaxed structure depends on the competition between wrinkle amplitude, strain gradient, and pattern shape.

Radius of tube formed at the flat edge of wrinkled pattern oscillates along the circumference with the average of radius of tube from flat film, in agreement between

elastic energy calculations and finite-element simulations. If the tube circumference is integer multiple of wrinkle period, subsequent tube rotations will conform to each other and will form non-uniform radial superlattice.

The preferential rolling direction of wrinkled pattern was confirmed by proof-of-principle experiment. Wrinkled photoresist was prepared by multiple exposure lithography with masks of increasing width and metallic film was deposited on top. Rolling-up behavior during etching of photoresist was recorded in optical microscope and qualitatively confirmed the preference for rolling-up on flat (short) edge of the wrinkled pattern, as compared to rolling-up on long edge of the flat pattern. Systematic investigations of wrinkle amplitude, period and aspect ratio were left for future studies.

There are recent reports on the fabrication of corrugated graphene and rolling-up of graphene into carbon nanoscrolls. Therefore, we estimated amplitude of corrugated graphene needed to suppress formation of carbon nanoscrolls on corrugated graphene edge. Chirality of the nanoscrolls could be designed by relative orientation of corrugations and carbon lattice.

Bending of wrinkled films could also serve as additional way of controlling microactuators by surface-chemistry [102, 103, 104] or electric field [105, 106] and macroscale actuators by light [107, 108]. Given the abundance of fabrication methods and applications of wrinkled [93, 95] and folding [3, 108] films across length scales, from conventional thin films down to graphene [109], our opens up new possibilities to realize and control 3D tubular structures on many length scales with well-controlled geometry, position and broad application potential.

Chapter 4

Electronic and optical properties of wrinkled quantum well

In this chapter, we start by introducing band structure and optical transitions in the quantum wells (QW). Afterwards, we present our work on strain-induced lateral distribution of transition energy and lateral carrier confinement in wrinkled membrane containing asymmetric QW structure.

4.1 Basic properties

This section summarizes basic properties of unstrained and strained semiconductor band structure, quantum wells and optical transitions in quantum wells.

4.1.1 Band structure of direct-gap semiconductor

The valence and conduction band E_V^0, E_C^0 of the unstrained direct-gap semiconductor material (e.g. GaAs) near the zone center Γ can be described by dispersion relations [110]

$$E_C^0 = E_V^0 + E_g^0 + \frac{\hbar^2 K^2}{2m_e}, \tag{4.1}$$

$$E_V^0 = E_{V,av}^0 + \frac{\Delta_0}{3} - \frac{\hbar^2 K^2}{2m_{lh,hh}}, \tag{4.2}$$

where $E_{V,av}^0$ is the average position of three topmost valence bands (light hole LH, heavy hole HH and spin-orbit split-off hole), Δ_0 is the spin-orbit splitting of the

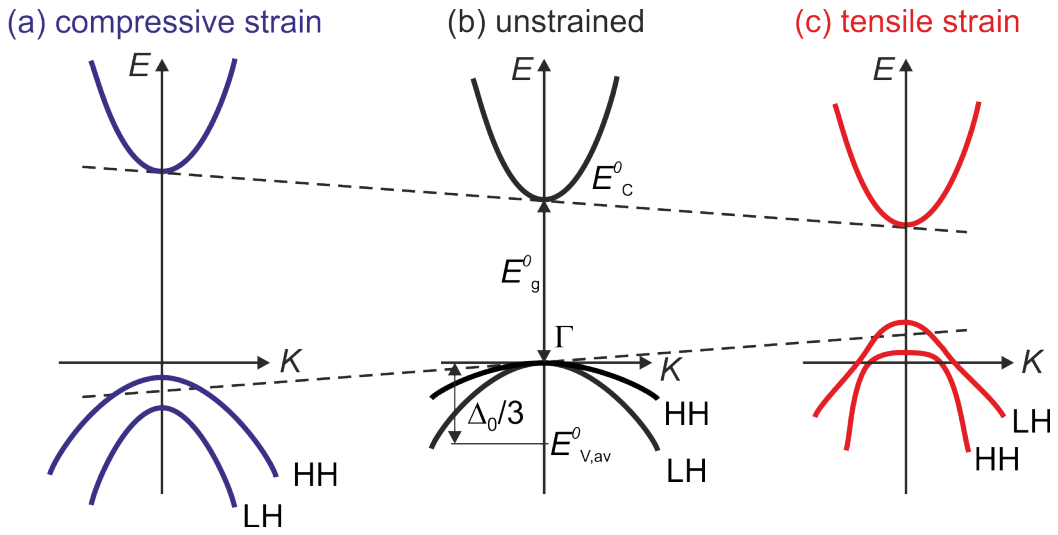

Figure 4.1: Schematic of the band structure of the (b) unstrained, (a) compressive strained, and (c) tensile strained direct-gap semiconductor. Dashed lines indicate shift of bands due to hydrostatic part of strain. LH and HH valence band at Γ point are degenerate only in unstrained material (b). Redrawn after [111, 110].

valence band, E_g^0 is the bandgap, $\hbar$ is reduced Planck constant, K indicates the wavevector of carriers, Fig. 4.1 (b). Only the two topmost valence bands LH and HH with effective masses m_{lh},m_{hh} are considered. The value of $E^0_{V,av}$ is given on absolute energy scale and therefore naturally gives relative band offsets for interface of different materials (roughly equivalent to Anderson's rule for electron affinity).

The deformation of the crystal lattice (strain) changes the distance between atoms and the band structure is therefore affected. By the linear deformation potential theory [110], for small strains (few %) the shift of bands is approximately linear. The position of the conduction and valence band of the strained with respect to the unstrained material depends on volumetric strain, eq. (1.7)

$$E_C = E_C^0 + a_C \varepsilon_{vol}, \tag{4.3}$$

$$E_V = E_V^0 + a_V \varepsilon_{vol} - b_V \left(\varepsilon_{zz} - \frac{\varepsilon_{xx} + \varepsilon_{yy}}{2} \right), \tag{4.4}$$

where a_C, a_V, b_V are corresponding deformation potentials. For compressive (tensile) strain, the conduction band is lifted up (shifted down) and HH is above (below) the LH band, Fig. 4.1(a,c). The effective mass are little affected by the presence of strain [111, 112]. The electronic properties of a $\mathrm{In_wGa_{1-w}As}$, which we used as typical material system for our calculations shown in Section 4.2 are listed in Table 4.1.

Table 4.1: Electronic parameters of $\mathrm{In_wGa_{1-w}As}$ at low temperature [113, 114]. Free electron mass is denoted m_0.

a_V (eV)	$1.00w + 1.16(1-w)$
a_C (eV)	$-5.08w - 7.17(1-w)$
b_V (eV)	$-1.8w - 1.7(1-w)$
$E^0_{V,av}$ (eV)	$-6.67w - 6.92(1-w)$
Δ_0 (eV)	$0.38w + 0.34(1-w)$
E^0_g (eV)	$0.418w + 1.52(1-w) - 0.51w(1-w)$
m_e (m_0)	$0.023w + 0.067\,(1-w)$
m_{hh} (m_0)	$0.4w + 0.5\,(1-w)$

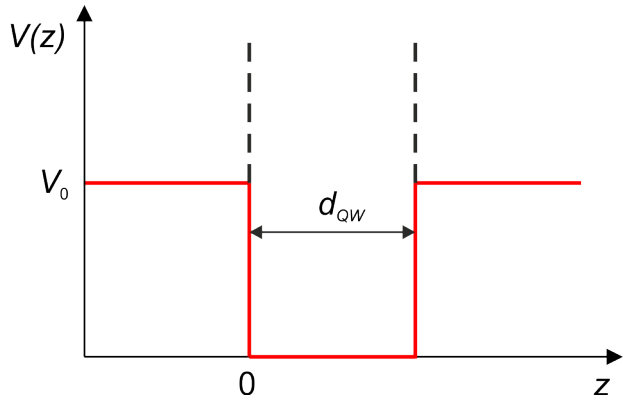

Figure 4.2: Schematic of the finite (infinite) quantum well potential $V(z)$ formed in growth (z) direction shown as red (dashed) line.

4.1.2 Infinite quantum well

It is often useful to simplify the confining potential of the heterostructure to an infinite potential well, Fig. 4.2. Within the single-band effective mass approximation, the eigenstate of the particle in the QW is assumed to have the form of the product of a periodic part of the appropriate Bloch function and the envelope function [115]. The envelope function χ is solution of the Schrödinger equation

$$-\frac{\hbar^2}{2m}\frac{\mathrm{d}^2\chi}{\mathrm{d}z^2} + V(z)\chi\,(z) = E\chi\,(z)\,, \tag{4.5}$$

with potential $V(z) = 0$ inside the well of thickness d_{QW} and ∞ otherwise and m the effective mass of particle. Dirichlet boundary conditions are imposed on edges. The quantized energies are

$$E_n = \frac{n^2\hbar^2\pi^2}{2md^2_{QW}} \tag{4.6}$$

and the corresponding envelope functions

$$\chi_n = \sqrt{\frac{2}{d_{QW}}} \sin\left(\frac{n\pi z}{d_{QW}}\right). \tag{4.7}$$

Electrons are confined in the QW in the growth direction (z), but are free to move in the plane of the layer (x, y). The energy dispersion can be written as

$$E = E_n + \frac{\hbar^2 K^2}{2m}, \tag{4.8}$$

where E_n denote quantized energies of the bound states in the QW, $n = 1, 2, 3, ...$, and K is the in-plane wavevector.

4.1.3 Finite quantum well

When a semiconductor with small bandgap is grown between a semiconductor with larger bandgap, finite QW with flat bands is formed, Fig. 4.2. The solution of the Schrödinger equation lead to the transcendent equation for the quantized energies E of the bound states

$$\tan\left[\left(\frac{m_w E d_{QW}}{2\hbar^2}\right)^{1/2}\right] = \left(\frac{m_b}{m_w}\frac{V_0 - E}{E}\right)^{1/2}, \tag{4.9}$$

where m_w and m_b are effective masses in well and barrier, V_0 is the potential height. When the bands are not flat (e.g. tilted, bent ...), mostly numerical solution of the Schrödinger equation is needed.

For a two-dimensional confinement potential $E_{conf}(x, z)$, the envelope function $\chi(x, z)$ (either for electron or hole) is solution of the Schrödinger equation [115]

$$-\frac{\hbar^2}{2}\nabla \cdot \left[\frac{1}{m(z)}\nabla\chi\left(x, z\right)\right] + E_{conf}(x, z)\chi\left(x, z\right) = E\chi\left(x, z\right), \tag{4.10}$$

where gradient is denoted $\nabla = \left(\frac{\partial}{\partial x}, \frac{\partial}{\partial z}\right)$, scalar product $\cdot$, and $m\left(z\right)$ is effective mass. The confining potential E_{conf} is set to E_C (E_V) for electrons (holes) in each layer separately. The matching conditions of envelope function at the boundaries between two materials A and B are

$$\chi(z_A) = \chi(z_B),\ \frac{1}{m(z_A)}\left.\frac{\partial\chi}{\partial z}\right|_{z=z_A} = \frac{1}{m(z_B)}\left.\frac{\partial\chi}{\partial z}\right|_{z=z_B}. \tag{4.11}$$

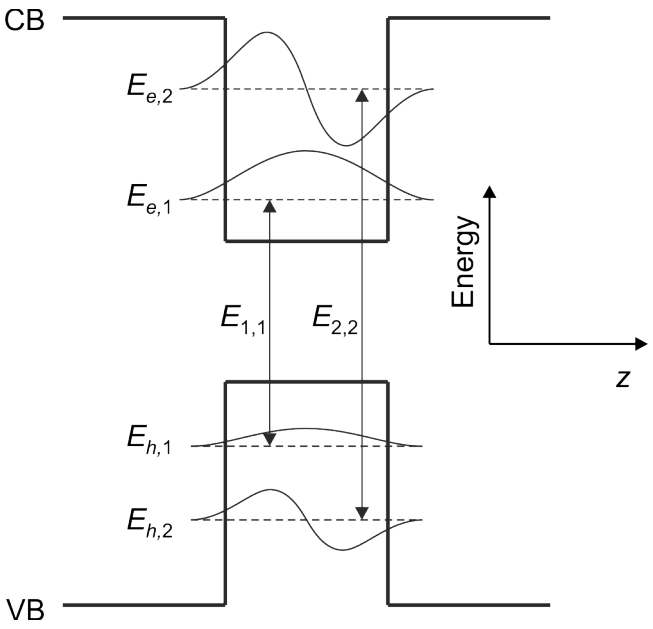

Figure 4.3: Optical interband transitions in QW between the first two bound states of the electron ($E_{e,1}$, $E_{e,2}$) and hole ($E_{h,1}$, $E_{h,2}$) with the same parity. Envelope functions are also shown at the corresponding energy levels.

We normalize envelope functions by square norm

$$\int |\chi|^2 \mathrm{d}\Omega = 1, \tag{4.12}$$

where Ω denotes the domain of the envelope function.

The Coulomb attraction between electron and hole pair (binding energy of exciton) in a quantum well is approximately constant [111] and will be neglected for simplicity. Further support for this assumption are the measurements of emission spectrum for wrinkle morphology similar to our typical system [116], which have shown no sharp exciton peaks.

4.1.4 Optical transitions

In the bulk semiconductor, excess electrons can be moved from the valence band to the conduction band by absorption of light. At the same time, holes are created in the valence band. For direct-gap semiconductor, the electrons from the conduction band can recombine with the holes in valence band and light can be emitted.

In the QW, electrons and holes confined in the QW recombine and photons with

energy $E_{n,m}$ are emitted, Fig. 4.3,

$$E_{n,m} = E_{e,n} - E_{h,m}, \tag{4.13}$$

where quantum numbers n, m correspond to energies $E_{e,n}, E_{h,m}$ of the electron and hole respectively, computed by SE eq. (4.10).

The transition rate of the radiative recombination between electron and hole in states n and m is given by Fermi's golden rule [115]

$$\frac{2\pi}{\hbar}|O_{n,m}|^2, \tag{4.14}$$

where $O_{n,m}$ is the overlap integral between electron and hole envelope functions

$$O_{n,m} = \frac{1}{|\Omega|}\int_{\Omega} \chi_{e,n}\chi^*_{h,m}\mathrm{d}\Omega, \tag{4.15}$$

and Ω denotes the domain of the envelope function. Overlap integral is non-zero only for transitions between the states with same parity. More details of quantum mechanical description of the optical transitions can be found in book by Davies [115].

4.2 Wrinkled quantum well

Flexible electronic devices have obtained substantial attention due to the possibility to stretch, compress and bend them [117, 118, 119, 120, 2] as opposed to standard electronic devices fabricated on rigid substrates. Wrinkled (or buckled) micro- and nanostructures [95, 121] have been recently investigated to provide stretchability for integrated circuits [122], photodetectors [7, 123], field-effect transistors [124], and solar cells [125] or bendability for light emitting diodes [126, 127].

Lateral modulation of the transition energy is traditionally hard to achieve. Quantum wells with modulated well thickness (quantum wires) on grooved substrates [128] or laterally epitaxially overgrown QWs [129] have shown lateral variation of transition energy ≈ 50 meV, but the fabrication process is expensive and lacks ability to dynamically control the lateral transition energy. Also lateral modulation of electrostatic field was used to create lateral distribution of the transition energy (≈ 3 meV) in QWs [130]. Recently, it was shown that incorporating QW structure into a shapable membrane can greatly modify absorption/emission properties of microtubes [131, 132, 133] and wrinkles [116].

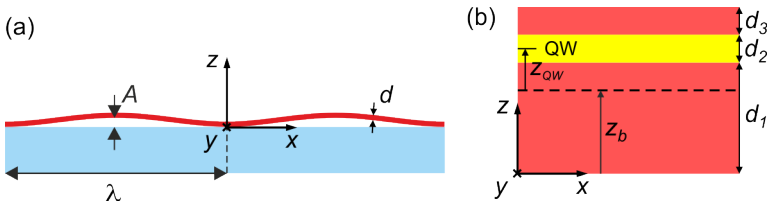

Figure 4.4: (a) Sketch of the WQW geometry with amplitude A, period λ, thickness d, and cartesian coordinate system (x, y, z). (b) Membrane layer structure with neutral plane at distance z_b (dashed), QW at distance z_{QW} from neutral plane .

In this section, we exploit the possibility to obtain lateral distribution of the transition energy by alternating curvature and strain of wrinkled nanomembrane with embedded quantum well (WQW). Large and mechanically tunable lateral transition energy modulation in wrinkled membranes is interesting for quasi-static control of QW emitters/detectors [134, 135, 136]. The lateral strain variation also creates a lateral potential well and carriers can be confined laterally in addition to vertical confinement due to the epitaxial QW [137, 138].

4.2.1 Strain distribution and scaling

We assume a wrinkled nanomembrane with the shape of its middle plane

$$\zeta(x) = \frac{A}{2}\left(1 - \cos(kx)\right), \tag{4.16}$$

where A and k are wrinkle amplitude and wavenumber ($k = 2\pi/\lambda$, λ is wrinkle period), Fig. 4.4(a). We consider small wrinkle amplitude $A \ll \lambda$, which means we can use cartesian coordinates (x, z) to describe the wrinkled membrane. The nanomembrane of total thickness d consists of barrier/QW/barrier layer stack with thicknesess d_i numbered from bottom to top $i = 1, 2, 3$, Fig. 4.4(b). For brevity, we will omit index i from symbols in the following.

Wrinkled films with micro- and nanoscale amplitudes can be fabricated by numerous approaches as reviewed in [93, 95]. We will mention two approaches of most relevance to our study. In the first approach, stiff semiconductor films [122] were fully bonded to a prestrained soft elastomeric substrate and upon release of the prestrain buckled into wrinkled shape. In the second approach, the film is only partially bonded to the substrate at certain positions defined by patterning [7], creating larger wrinkle amplitudes and thus allow for large stretchability (tens of %) and more control over wrinkle periodicity.

Table 4.2: Material parameters of GaAs and InAs [114, 113], a denotes lattice constant.

	ν	Y (GPa)	a (Å)
GaAs	0.31	85.3	5.6533
InAs	0.35	51.4	6.0584

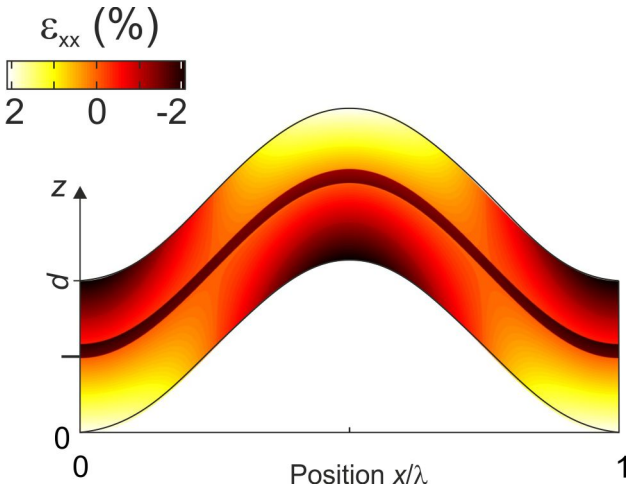

Figure 4.5: Lateral strain ε_{xx} in typical WQW shown in the domain of wrinkled membrane. Position of the neutral plane ($z_{QW} = 2\,\mathrm{nm}$) is shown as black tick on left side of the membrane.

Our typical WQW structure consists of GaAs barriers with initial (misfit) strain $\varepsilon_0 = 0$, $In_{0.22}Ga_{0.78}As$ QW layer ($\varepsilon_0 = -1.5\%$) and $d = 44\,\mathrm{nm}$. The GaAs barrier thickness is always kept larger than 10 nm in order to ensure good carrier confinement in the QW layer [139]. We assume $A = 50\,\mathrm{nm}$ and $\lambda = 1\,\mu\mathrm{m}$, which is realistic to fabricate, [7] since minimum feature size $\lambda \approx 300\,\mathrm{nm}$ of the lithography process has been reported [140]. Mechanical properties of the layers are interpolated by Vegard's law from values listed in Table 4.2. Electronic constants are listed in Table 4.1.

Additional strains arise after deformation of the membrane, as we discussed in Section 1. The lateral strain ε_x in the wrinkled membrane on Fig. 4.5 also consists of the epitaxial and bending strains

$$\varepsilon_{xx} = \varepsilon_0 + \varepsilon^b_{xx}, \tag{4.17}$$

$$\varepsilon^b_{xx} = -\left(z - z_b\right)\kappa_{xx}, \tag{4.18}$$

where curvature can be approximated from eq. (1.2) as $\kappa_{xx} \approx \frac{Ak^2}{2}\cos(kx)$ for $A \ll \lambda$ and position of neutral plane z_b is defined in eq. (1.3). The membrane

strain after buckling is negligible compared to bending strain for most of the buckled microstructures [5, 122, 141], because buckling of the membrane relaxes much of the initial membrane strain. We do not consider relaxation of the strain in y direction $\varepsilon_y = \varepsilon_0$. Transverse strain in the film is given by eq. (1.6).

The position of middle plane of QW layer with respect to the neutral plane is denoted z_{QW} (asymmetry of the QW), Fig. 4.4(b), and it holds

$$z_{QW} = d_1 - \frac{d}{2} + \frac{d_2}{2}. \tag{4.19}$$

QW is called symmetric for $z_{QW} = 0$ and asymmetric for $z_{QW} > 0$. The bending strain in the middle of the QW can be written as

$$\varepsilon^b_{QW} = -2\pi^2 z_{QW} \frac{A}{\lambda^2} \cos\left(\frac{2\pi x}{\lambda}\right). \tag{4.20}$$

Since always $z_{QW} < d/2$ it is natural to normalize A, λ, and z_{QW} by membrane thickness d

$$z'_{QW} = \frac{z_{QW}}{d},\ A' = \frac{A}{d},\ \lambda' = \frac{\lambda}{d}. \tag{4.21}$$

It will later turn out how important is the normalized value of z'_{QW}, because it quantifies the relative position of QW with respect to the thickness of the membrane. Hence, in normalized variables, bending strain in QW is

$$\varepsilon^b_{QW} = -2\pi^2 z'_{QW} \frac{A'}{\lambda'^2} \cos\left(\frac{2\pi x}{\lambda}\right). \tag{4.22}$$

Important aspect for the practical application of the wrinkled membrane is the extent of stretch/compression without mechanical fracture. Fracture will destroy the crystal structure of the membrane in certain points where dislocations will appear [142]. The membrane fractures when the bending strain at membrane surface reaches fracture limit ε_{frac} (e.g. $\approx 2\%$ for GaAs [7, 143])

$$\varepsilon_{surf} = \frac{d}{2}\kappa_{max} = \pi^2 \frac{A'_{max}}{\lambda'^2} = \varepsilon_{frac}, \tag{4.23}$$

where the maximum wrinkle amplitude (for fixed period) before fracture

$$A'_{max} = \varepsilon_{frac} \frac{\lambda'^2}{\pi^2}. \tag{4.24}$$

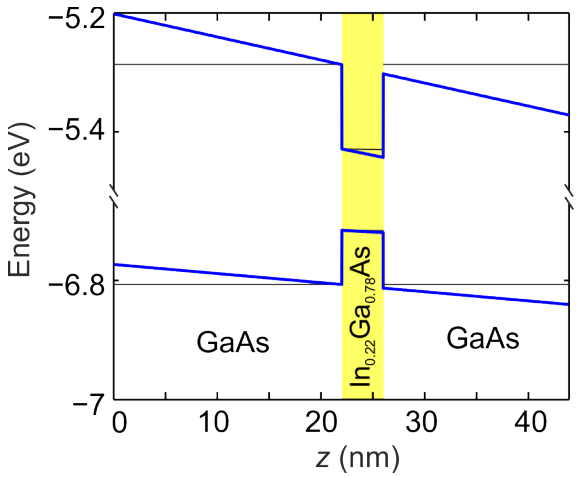

Figure 4.6: Conduction (top) and valence (bottom) band profile through the thickness of the typical WQW with $z_{QW} = 2\,\mathrm{nm}$ at the top of wrinkle ($x = \lambda/2$, line P_1 in Fig. 4.7(a)). Solid lines show bands of flat membrane for comparison.

4.2.2 Band diagram

The QW created in the growth (thickness) direction by stacking materials with different bandgap has flat band alignment, Fig. 4.6. For the typical system we consider in this work, the depth of the vertical potential well is $V_{e,ver} \approx 140\,\mathrm{meV}$. Along the wrinkled membrane, band profile through the thickness will be tilted due to bending strain in different ways according to position on the wrinkle, Fig. 4.6.

In addition to the vertical quantum well formed in the growth direction, variation of the lateral bending strain along the wrinkled membrane ε_x alters the band with opposite sign at convex and concave WQW regions, creating a lateral potential well in the QW layer, Fig. 4.7. The depth of the lateral potential well in the QW layer is for electron

$$V_{e,lat} = E_C(0,z) - E_C(\lambda/2,z) = -2a_C\varepsilon_{xx}^{b,max}\frac{1-2\nu}{1-\nu}, \tag{4.25}$$

where $\varepsilon_{xx}^{b,max} = 2\pi^2\left(z - z_b\right)A/\lambda^2$ is the bending strain at the top of wrinkle ($x = \lambda/2$). Note that the initial strain ε_0 dissappears because of the subtraction. Similarly, for hole

$$V_{h,lat} = E_V(0,z) - E_V(\lambda/2,z) = -2c_V\varepsilon_{xx}^{b,max}, \tag{4.26}$$

$$c_V = a_V\frac{1-2\nu}{1-\nu} - b_V\frac{1+\nu}{2\left(1-\nu\right)}. \tag{4.27}$$

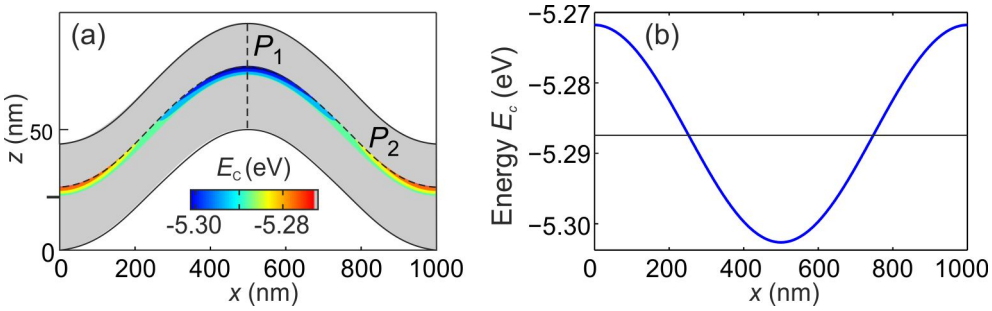

Figure 4.7: (a) Relative variation of the conduction band E_C showing lateral potential well in blue contours and barriers as grey color. Position of the neutral plane ($z_{QW} = 2\text{nm}$) is shown as black tick on left side of the membrane. (b) Conduction band energy E_C along the top contour of QW layer P_2 shown in (a), $z = 26\,\text{nm}$, $\varepsilon_{xx}^{b,max} = 0.4\%$. Solid line denotes energy of flat strained QW, $E_{C,str}$.

From Table 4.1 we see $a_C < 0$ and $c_V > 0$. Consequently the potential minimum for electron (hole) is in the concave (convex) region corresponding to $x = \lambda/2$ ($x = 0$). The magnitude of the lateral potential well ($V_{e,lat} \approx 30\,\text{meV}$) for electron and typical parameters on Fig. 4.7 is one order smaller compared with the magnitude of the "growth" vertical potential well ($V_{e,ver} \approx 140\,\text{meV}$), Fig. 4.6.

We further estimate the maximum depth of the lateral potential well $V_{e,lat}^{max}$. Note that for our typical QW system, we can place QW not less than 10 nm below the membrane surface, implying $z'_{QW} = 23\%$ and $\varepsilon_{QW} = 1.0\%$. If we increase the total thickness of the membrane, we can approach the limiting values $z'^{max}_{QW} \to 50\%$ (QW almost at the membrane surface) and $\varepsilon_{QW}^{max} \to 2.0\%$ (strain in the QW approaches fracture strain at the membrane surface, Section 4.2.1). These limiting values give $V_{e,lat}^{max} = 150\,\text{meV}$ which is similar in magnitude to vertical potential well $V_{e,ver} \approx 140\,\text{meV}$. The depth of our lateral potential well can compare with the strain-induced lateral confinement in QWs by patterned stressors [144, 137]. In these works, the lateral potential well for electrons (≈ 20 meV) was created by strain gradients and electron confinement was demonstrated to effective width of 35 nm. The lateral confinement energy was measured (2.6 meV) and agreed well with calculated value based on strain-induced bandedge shift. It therefore seems feasible to measure the lateral confinement in the wrinkled nanomembrane by spectroscopic techniques.

There has been a lot of theoretical work on quantum confinement of carriers to curved surfaces [145, 146, 147], where the description is simplified to the curved surface with additional "geometric potential" proportional to the square of curvature. This is in contrast to the deformation potential due to strain, which scales linearly with curvature. In fact, Ortix et al. [148] recently included the strain deformation

potential into the theoretical framework and found that it rescales the pure geometric potential by several orders of magnitude. Therefore, we neglect effects of the pure geometric potential in our system.

4.2.3 Transition energies

Having derived the band profile in the wrinkled membrane, we can study its influence on eigenenergies of the carriers. The simplest approach is to solve one-dimensional (1D) Schrödinger equation (4.10) through the membrane thickness (z) at fixed position along wrinkle (x). We implemented mass discontinuous finite-difference method [149] in Mathematica® [45]. Quantized energies of electron and hole are computed separately and the transition energy between their ground states is given by difference of their quantized energies, eq. (4.13).

For maximum value of $z_{QW} = 10\,\mathrm{nm}$ we have the maximum bending strain in the QW $\varepsilon_{QW}^{b,max} = \pm 1.0\%$. Since typical initial strain in the QW is $\varepsilon_0 = -1.5\%$, the strain in QW eq. (4.17) is always compressive, $\varepsilon_{xx} < 0$. The ground state for compressed material is heavy hole, Fig. 4.1(a) [150]. In the following, we will work with $z_{QW} > 0$ and thus the heavy hole ground state. For different layer properties, the light hole might be as well the ground state. If the QW is positioned on the opposite side of the neutral plane, $z_{QW} < 0$, the results can be obtained by switching convex and concave regions.

We illustrate the shift of the transition energies in a schematic manner on Fig. 4.8. At the concave (convex) region of the wrinkle, QW is more stretched (compressed) compared to the flat strained QW, shifting the transition energy down (up) in energy. The calculated transition energy of flat strained QW is $E_0 = 1.3761\,\mathrm{eV}$ and the corresponding wavelength $901.0\,\mathrm{nm}$. The shift in the transition energy E relative to the energy of planar strained QW E_0 is defined as

$$\Delta E' = \frac{E - E_0}{E_0}. \tag{4.28}$$

We calculated first the shift of transition energy $\Delta E'$ for typical parameters at the wrinkle valley, $x = 0$. The ground states of electron and hole are mostly localized in the QW layer and give reasonable radiative recombination, Fig. 4.9. The exception and thus no radiative recombination is the bottom right case ($A = 70\,\mathrm{nm}$) where the epitaxial QW was not minimum of energy anymore (due to the tilt of the confining potential shown blue in Fig. 4.9) and electron leaked to the GaAs barrier layer, where

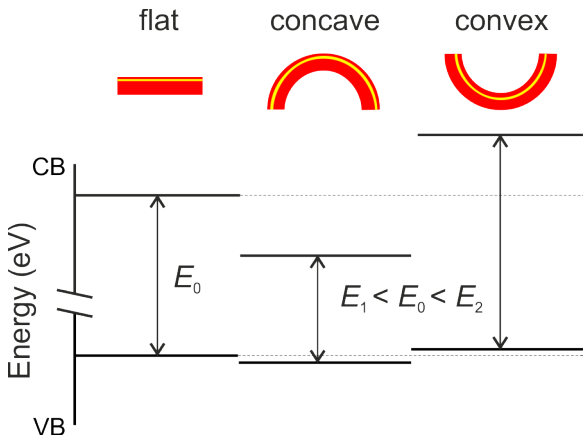

Figure 4.8: Sketch of the relative values of transition energies for flat, concave and convex region of wrinkled nanomembrane. Flat region has transition energy E_0 and the concave (convex) region has smaller (larger) transition energy E_1 (E_2) than E_0. Most of the transition energy shift comes from the conduction band. Typical parameters and $z_{QW} > 0$ is assumed (yellow layer).

it will decay to the surface state[1]. However, in this case the surface bending strain ($\varepsilon_{surf} = 3.0\%$) will be much larger than fracture strain of the GaAs ($\varepsilon_{frac} \approx 2\%$). We observed localization of electron in the barrier layer for convex regions, but the electron and hole were both in the QW layer for concave regions. This means that radiative recombination will be possible only in concave regions.

We have calculated the transition energy shift $\Delta E'$ at different positions x/λ along the wrinkled membrane and for range of QW asymmetries z'_{QW} in Fig. 4.10. We remind that asymmetry of QW z_{QW} is limited by the condition of good carrier confinement in the QW layer [139] and therefore has to be smaller than 10 nm for our typical parameters, implying $z'_{QW} \leq 23\%$. For symmetric QW, small bending strain creates only little lateral variation of $\Delta E'$. Increase of bending strain in asymmetric QW causes blue and red shift of the transition energy $\Delta E'$ for convex and concave region, respectively, which both increase in magnitude for increasing z'_{QW}. In the nearly flat region, the transition shift is almost zero as there's no bending strain present. For the typical parameters used, the transition energy shift laterally varies between $\pm 1.9\%$ ($\pm 26\,\mathrm{meV}$ or $\pm 17\,\mathrm{nm}$).

Since the WQW has broad range of transition energies, it is natural to characterize its spectrum by the difference of the transition energies at most convex ($x = 0$) and concave ($x = \lambda/2$) points, bandwidth B. In Fig. 4.10 the maximum bandwidth is

[1]The effect of leaking state through tilted potential is well known as Fowler-Nordheim tunneling, but usually is caused by electric field induced tilting of the confining potential [115].

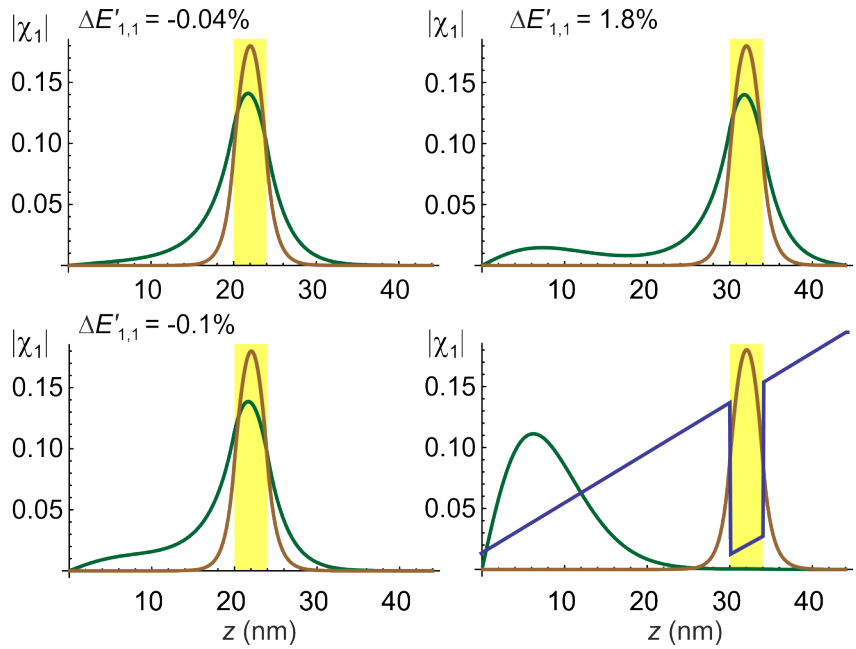

Figure 4.9: Localization of electron ($\chi_{e,1}$, green) and hole ($\chi_{h,1}$,brown) ground state for symmetric ($z'_{QW} = 0\%$, first column) and asymmetric QW ($z'_{QW} = 23\%$, second column) and $A = 50\,\mathrm{nm}$ (first row), $A = 70\,\mathrm{nm}$ (second row). In the bottom right figure, the ground state electron is not localized in the QW while the hole is still localized. The confinement potential for electron is also shown in blue. Typical parameters are assumed and region of the QW layer is shown in yellow.

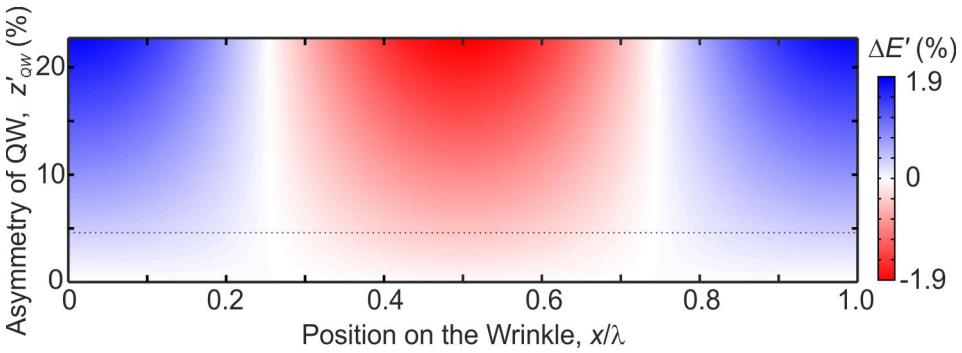

Figure 4.10: Transition energy shift $\Delta E'$ as a function of x/λ (only half period is shown) and z'_{QW}, for typical parameters mentioned in text. Dotted line marks $z'_{QW} = 4.6\%$, corresponding to Fig. 4.13(b,c).

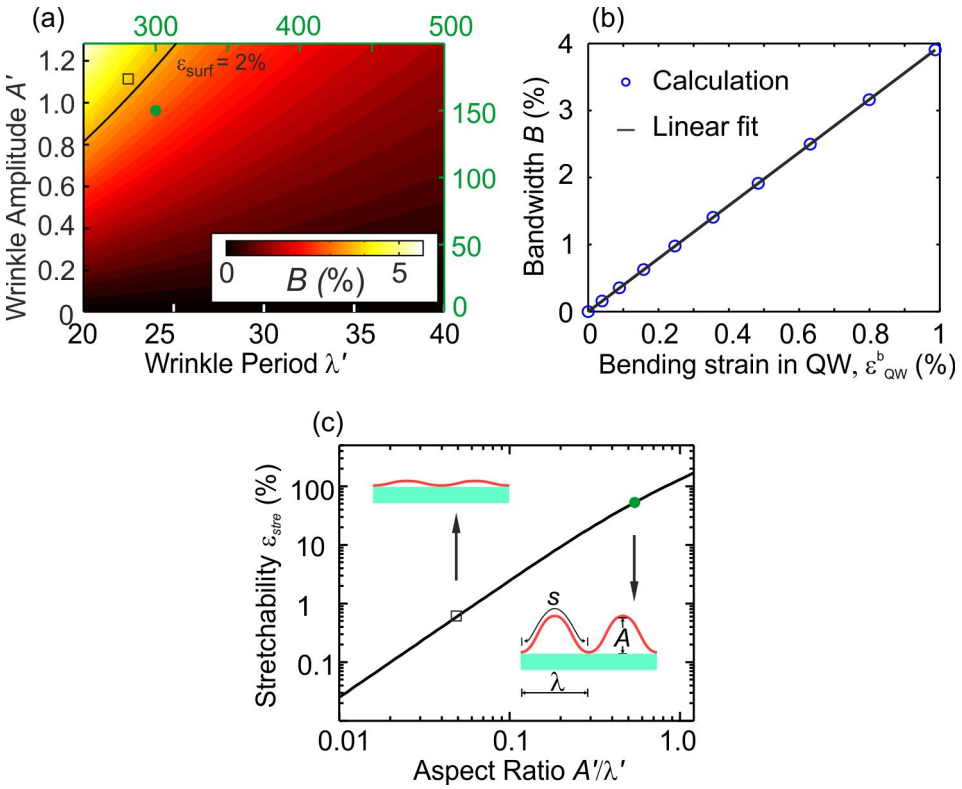

Figure 4.11: (a) Transition bandwidth B as a function of normalized wrinkle period λ' and amplitude A' for $z'_{QW} = 23\%$. Left and bottom axes are for typical WQW (square), top and right green axis are for scaled-up WQW (green circle), described in the main text. The condition of maximum ε_{surf} of 2% for GaAs is labeled. (b) Calculated bandwidth B (blue circles) from few points in (a) as a function of bending strain in the QW, ε^b_{QW}. Linear fit is shown as black line. (c) Stretchability ε_{stre} of wrinkled membrane as a function of A/λ with black square and green circle for typical and scaled-up wrinkle parameters as in (a).

$B = 3.8\%$ for $z'_{QW} = 23\%$.

Another interesting question is how bandwidth changes for different amplitude and period of the wrinkle. First we varied the typical wrinkle parameters in the range $A' = (0, 1.28)$ and $\lambda' = (20, 40)$ shown as black axes in Fig. 4.11(a). With increasing λ' or decreasing A', the effect of curvature is weaker and B decreases. Fracture of the membrane (due to bending) will occur for $A' > A'_{max}$ from eq. (4.24), which is shown for $\varepsilon_{surf} \approx 2\%$ [7]. For $A > 70$ nm and $\lambda = 1\ \mu$m, electrons localize in the potential well formed in the barrier layers and leak to the surface states (not shown, similar to Fig. 4.9). In general, fracture strain ε_{frac} depends on strain rate and temperature [151]. For example, fracture strain of GaN can be as large as 5% [152] at room temperature and 7% at 1280 K [153], thus potentially enabling larger

bandwidth.

From the linear dependence of lateral potential on strain in eq. (4.25) we expect that the bandwidth B will be also linearly dependent on strain ε^b_{QW}. Indeed, the calculated bandwidth B increases linearly with ε^b_{QW}, Fig. 4.11(b). We obtained the proportionality constant $B \approx 4\varepsilon^b_{QW}$ by fitting the calculated values with goodness of fit ≈ 1.

A highly stretchable WQW with large bandwidth is proposed. The stretchability of the wrinkled membrane is defined as

$$\varepsilon_{stre} = \frac{s - \lambda}{\lambda}, \tag{4.29}$$

where s is arclength of one wrinkle period, inset of Fig. 4.11(c). We assume wrinkled membrane is fabricated on a flexible substrate as in Sun et al. [7] and can be stretched till the flat state. The final length of the wrinkle will be $\lambda(1 + \varepsilon_{stre})$ and amplitude $A = 0$. For shallow wrinkles ($A \ll \lambda$), arclength can be approximated by

$$s \approx \lambda \left(1 + \frac{\pi^2 A^2}{4\lambda^2}\right). \tag{4.30}$$

Since bandwidth D scales with ε^b_{QW} (which depends on A', λ' and z'_{QW}, eq. (4.22)) and stretchability scales with aspect ratio A/λ, they can be tuned independently. For example, if we scale up wrinkle dimensions to $A' = 150$, $\lambda' = 300$, and keep $d = 44$ nm, we will obtain stretchability $\varepsilon_{stre} = 60\%$. This is about two orders of magnitude larger than $\varepsilon_{stre} = 0.5\%$ for typical wrinkle parameters used before, Fig. 4.11(c). We varied the scaled up wrinkle parameters in the range $A' = (0, 200)$ and $\lambda' = (250, 500)$, green axes in Fig. 4.11(a), to give the same bending strain ($\varepsilon^b_{QW} \sim A'/\lambda'^2$) and thus bandwidth as typical parameters $A' = (0, 1.28)$ and $\lambda' = (20, 40)$ shown in black axes. To be more precise, the arclength for wrinkle amplitude comparable to period ($A > \lambda$) is given by

$$s = \frac{2\lambda}{\pi} \mathrm{E}\left(\frac{i\pi A}{\lambda}\right), \tag{4.31}$$

where $\mathrm{E}(.)$ denotes complete elliptic integral of the second kind [154]. Therefore, the corrected stretchability gives smaller values than the approximate expression (4.30).

Maximum bandwidth of the WQW B_{max} can be estimated by recalling that B scales linearly with strain ε^b_{QW}, Fig. 4.11(b). Up to here we have considered typical parameters $d = 44$ nm and $z'_{QW} = 23\%$, as compared to its maximum value $z'_{QW} =$

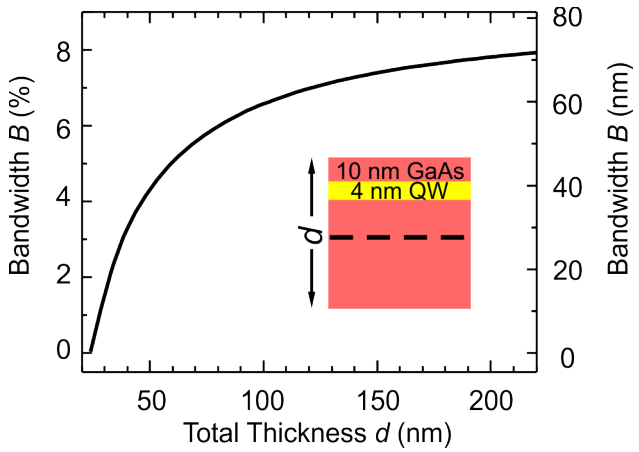

Figure 4.12: Bandwidth B in relative units (left axis) and wavelength units (right axis) as a function of total membrane thickness d for $\varepsilon_{surf} = 2\%$.

50% for large d. By increasing the total thickness and decreasing the amplitude to satisfy fracture limit according to eq. (4.24), the calculated bandwidth increases to $B \approx 8\%$ for $d = 224\,\mathrm{nm}$, which corresponds to $\approx 70\,\mathrm{nm}$ in the wavelength scale, Fig. 4.12. The limiting value $B_{max} \approx 9\%$ is approached for very large d.

4.2.4 Lateral carrier localization

Up to here, we have considered the vertical confinement along the wrinkled membrane separately and determined the transition energies. However, as we have seen in Fig. 4.7, a lateral potential well is created along the WQW and it can confine carriers also laterally, in addition to the confinement by the epitaxial vertical QW. Therefore, we studied the lateral confinement in the two-dimensional (2D) cross-section of the WQW by numerically solving the Schrödinger equation in x, z by finite-element method [88]. The cross-section of one wrinkle period was approximated as rectangular calculation domain (justified by shallow wrinkle slope) and the strain was calculated by eq. (4.17). Rectangular mesh with 800 horizontal nodes and 10 nodes in every layer was used. Periodic boundary condition was used to connect left and right boundary of the WQW and Dirichlet condition was applied on top and bottom surfaces of the WQW. Envelope functions were mapped to the wrinkled domain during postprocessing of calculation results, Fig. 4.13.

For symmetric WQW, the electron and hole envelope functions are both localized laterally in the convex and concave regions of WQW because these are equivalent with respect to the potential, Fig. 4.13(a). For asymmetric WQW, ground state of

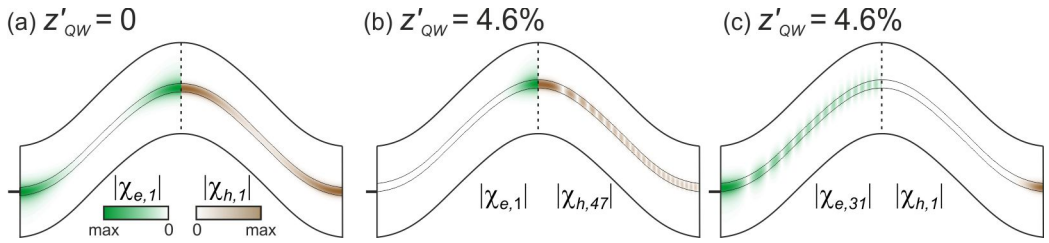

Figure 4.13: Localization of electron (green) and hole (brown) envelope functions for (a) symmetric and (b,c) asymmetric WQW. The value $z'_{QW} = 4.6\%$ resulted from choosing the position $z_{QW} = 2\,\mathrm{nm}$. Due to mirror symmetry, we plot only on half of the period. Positions of the neutral plane are shown as black ticks on left side of membranes, whose thicknesses were enlarged for clarity.

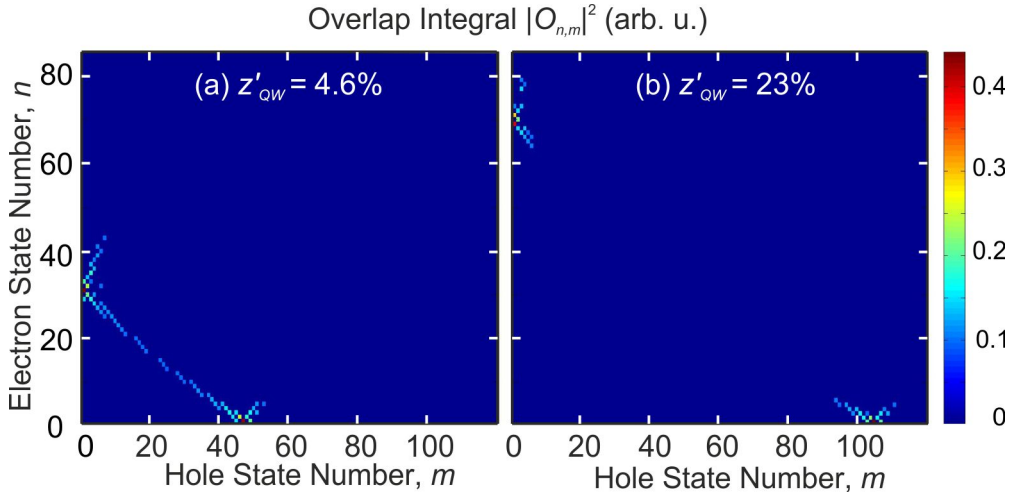

Figure 4.14: Overlap integral $|O_{n,m}|^2$ for transition between various electron and hole states for (a) $z'_{QW} = 4.6\%$ and (b) $z'_{QW} = 23\%$. Only transitions $n < 85$, $m < 120$ and $|O_{n,m}|^2 > 0.1$ are shown.

electron $\chi_{e,1}$ localizes in concave and ground state of hole $\chi_{h,1}$ localizes in convex region, Figs. 4.13 (b,c), because the potential well is created in the concave (convex) region for electron (hole), eq. (4.25). Lateral confinement energy of electron (hole) is $0.3\ \mathrm{meV}$ $(0.1\ \mathrm{meV})$, which is comparable to thermal energy at low temperature ($\sim$1 meV at 10 K) but small with respect to QW luminescence linewidth $(4\ \mathrm{meV})$ and vertical confinement energy due to epitaxial QW (110 meV).

We estimate the limiting value of the lateral confinement energy by expanding the sinusoidal lateral potential (Fig. 4.7) around its minimum ($x = \lambda/2$)

$$\frac{V_{e,lat}}{2}\left[1+\cos(kx)\right] \approx \frac{V_{e,lat}}{2}\frac{k^2\left(x-\lambda/2\right)^2}{2}, \tag{4.32}$$

which is a parabolic well with equidistant energy levels

$$\left(n+\frac{1}{2}\right)\frac{2\pi\hbar}{\lambda}\sqrt{\frac{V_{e,lat}}{2m}}. \tag{4.33}$$

By using eq. (4.25) the lateral confinement energy is proportional to

$$\frac{\hbar}{\lambda}\sqrt{\frac{a_C\varepsilon^b_{QW}}{m}}. \tag{4.34}$$

and gives maximum of $\approx 6\mathrm{meV}$ for minimum feasible wrinkle period $\lambda = 300\mathrm{nm}$ [140] and maximum bending strain $\varepsilon^b_{QW} \approx \varepsilon_{frac} = 2\%$. This lateral confinement energy is comparable with stressor-induced confinement energy in QWs, which is $\approx 3\ \mathrm{meV}$ as previously reported in [144, 137].

The radiative recombination is not probable due to the separation of electron and hole ground state for asymmetric QW. However, the excited states of hole increasingly overlap with electron ground state, Fig. 4.13(b). Excited electron states also overlap with ground hole state, Fig. 4.13(c). We computed the overlap integrals $O_{n,m}$ between different states of electron and hole to quantify the strength of radiative recombinations using eq. (4.15), Fig. 4.14. For $z'_{QW} = 4.6\%$, the maximum overlap is between $\chi_{e,1}$-$\chi_{h,47}$ and $\chi_{e,31}$-$\chi_{h,1}$. For $z'_{QW} = 23\%$, the maximum overlap is between even higher states $\chi_{e,1}$-$\chi_{h,105}$ and $\chi_{e,69}$-$\chi_{h,1}$.

We further calculated the overlap integral for electron-hole transitions as function of transition energy shift $\Delta E'$ for increasing asymmetry z'_{QW}, Fig. 4.15. For $z'_{QW} = 0$, the maximum overlap is mainly for $n = m$ and transitions are blueshifted because excited states have higher energy. Two groups of transitions that we have seen in Fig. 4.14 make up two transition peaks, Fig. 4.15(b) :

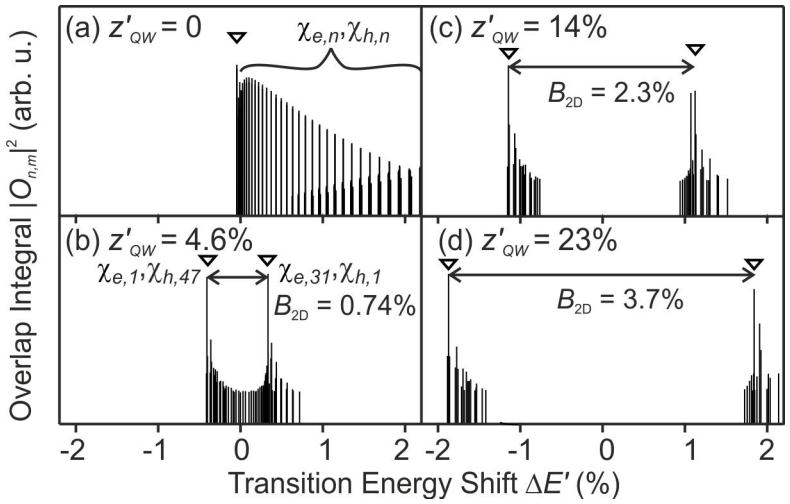

Figure 4.15: Bar plots of the overlap integrals versus $\Delta E'$ for increasing asymmetry z'_{QW} of the QW from (a) to (d). The transition bandwidth B_{2D} is labeled. Only transitions $n < 85$, $m < 120$ and $|O_{n,m}|^2 > 0.1$ are shown.

1. high $\chi_{h,m}$ and first few $\chi_{e,n}$ overlap in the concave region (peak with redshift) in Fig. 4.13(b) .

2. high $\chi_{e,n}$ and first few $\chi_{h,m}$ overlap in the convex region (peak with blueshift) in Fig. 4.13(c)

The distance of these two transition peaks also defines the bandwidth B_{2D} between convex and concave region in analogy to the 1D bandwidth B from the previous section. The magnitude of B_{2D} agrees well with the magnitude of B from Fig. 4.10 (e.g. $B_{2D} = 3.7\%$ and $B = 3.8\%$ for $z'_{QW} = 23\%$). This can be understood in the following way. In the convex (concave) region, there is potential well for the electron (hole) and therefore electron (hole) is in the ground state. However, no potential well for the hole (electron) is created in the convex (concave) region, and it has to be in the excited state to be in the convex (concave) region and overlap with electron (hole) ground state. Therefore, the 1D calculation at convex (concave) region has given the same transition energy as 2D calculation with excited states.

4.2.5 Strain in bonded-back wrinkled membranes

As one application of our theory, we looked at the photoluminescence measurements from wrinkled nanomembrane with embedded quantum well by Mei et al. [116]. Even though the morphology is slightly different with nanomembrane partially bonded-back to the substrate, Fig. 4.16, the common part is that wrinkled shape changes the

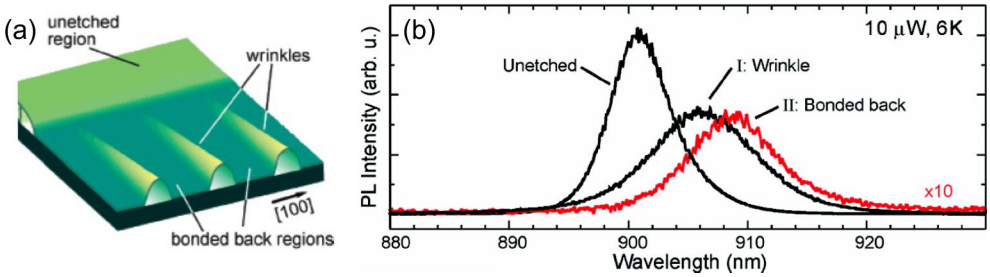

Figure 4.16: (a) The morphology of wrinkled membrane with bonded back regions. (b) Photoluminescence measurement of unetched, wrinkled (concave) and bonded back region. Taken from [116].

optical emission of QW. To prevent misunderstandings, we remind that the theory of small deflections of thin plates defines neutral plane as a plane where there is neither compression nor tension during small bending (compared to film thickness) [12]. For homogeneous plate the neutral plane lies clearly in the middle of the plate. However, Mei et al. [116] have taken the position of "neutral plane" as a fitting parameter. In that case, the plane should be rather denoted "plane of equilibrium lattice constant", because it denotes position where lattice constant is planar relaxed. The position of neutral plane of the multilayer in the sense of the established plate theory is not changed.

For simplicity, we assume the strain in the wrinkled region of the membrane consists only of the initial mismatch strain in the layers is ε_0 and additional bending strain $\varepsilon^b_{xx} = -(z - z_b)\kappa$ as in eq. (4.17). The measured averaged curvature of concave wrinkle region from atomic-force microscope is $\kappa = 1.33\,\mu\mathrm{m}^{-1}$ [116]. With this value of curvature, we then solved for the energies of electron and hole in 1D similarly as in section 4.2.3, resulting in the emission shift $+5.0\,\mathrm{nm}$ with respect to the unetched QW, which agrees well with the measured shift $+5.1\mathrm{nm}$ on Fig. 4.16(b) without any fitting parameter and also with the correct sign (blue shift). Thus, the nanomembrane did not relax the initial strains significantly and they are only altered by the bending of the nanomembrane.

4.2.6 Conclusion

We have used alternating bending strain along wrinkled nanomembrane to laterally engineer the band diagram of the embedded quantum well. Bending strain naturally scales with amplitude, period and asymmetry of the QW, all normalized to membrane thickness. The simplest 1D calculation of optical transition energies at different

points along the membrane has shown lateral variation of transition energy (up to 2%) dependent on the position of QW (asymmetry) inside the membrane relative to the neutral mechanical plane. The difference of the transition energy at the most convex and concave point along wrinkle is called bandwidth as it gives spectral width of emitted radiation when measured by a probe large compared to wrinkle period. Dependence of bandwidth on wrinkle amplitude and period is calculated and linear scaling of bandwidth with bending strain in the QW is observed.

The practical limitation of shape of wrinkled membrane is that bending strain at the membrane surface cannot overcome the fracture strain of the semiconductor material (few %). For given fracture strain of the membrane material (2% for GaAs), large membrane thickness and QW close to membrane surface, the limiting bandwidth is estimated to be 70 nm for $In_{0.22}Ga_{0.78}As$ in thick GaAs membrane, being of interest for detectors and emitters.

We investigated how much stretching can be applied to WQW placed on flexible substrate until it is completely flattened. This stretchability scales only with amplitude and period of the wrinkle and therefore can be tuned independently of the bandwidth (which scales also with thicknesess of the membrane). We showed that large stretchability (tens of %) of the WQW is possible to combine with large bandwidth.

Carrier localization in lateral potential well created by strain is studied by 2D numerical calculations. For symmetric WQW, both electron and hole are confined in convex and concave region. For asymmetric WQW, electron (hole) weakly localizes (confinement energy 0.5 meV) in concave (convex) region thus diminishing overlap of their wavefunctions and radiative recombination. However, the excited states of hole extend increasingly in the concave region and eventually overlap with electron ground state. Transition energy of this recombination agrees with the 1D calculation at the concave region.

4.3 Outlook

Wrinkled QW can be utilized for a design of broad bandwidth emitters or detectors. These devices can allow for large extent of mechanical deformation (stretching) impossible with the traditional rigid substrates. The deformation can be also used to tune the bandwidth at the same time. Different material systems, e. g. AlGaAs/GaAs for emission in visible range or InGaAsP/InP for telecommunication wavelengths might be exploited. By considering intersubband transitions in the QW (in addition to

interband transitions considered in this work), far-infrared light might be also emitted/detected. For practical applications, the light propagation and interference from the WQW should be studied in more detail. For example, it was already shown that enhanced light emission from wrinkled regions can be explained by interference contrast theory [116].

Interestingly, the effect of curvature on potential profile, eq. (4.25), written in the simplified form as

$$V(z) = a_{C,V}\kappa z, \tag{4.35}$$

is very similar to applying the electric field perpendicular to the plane of the well known as quantum-confined Stark effect (QCSE)

$$V(z) = eFz, \tag{4.36}$$

where $e = 1.6 \cdot 10^{-19}\,\mathrm{C}$ is the electronic charge and F is the electric field. We will call this analogy curvature QCSE. The difference is that slope of the band tilting due to curvature is different for electron and hole due to the different deformation potentials, whereas the slope of electron and hole bandedges is the same in the case of QCSE (with electric field F). The scale of possible potential shift per QW thickness can be compared easily; maximum electric field used in experiments $100\,\mathrm{kV/cm}$ [155] gives $eF = 10\mathrm{meV/nm}$; deformation potential $a_C = 7\mathrm{eV}$ and typical curvature of wrinkled membrane [116] or rolled-up tube [33] $\kappa = 1\ \mu\mathrm{m}^{-1}$ give $a_C\kappa = 7\ \mathrm{meV/nm}$. The similar magnitude of potential shift by electric field and curvature shows its promise for future investigations.

However, the development and handling of semiconductor membranes and their shape is rather recent advance [156, 2] and curvature QCSE was not yet exploited from application perspectives. For example, nanomechanical beam oscillators [157] provide two states with different curvature. If the beam has incorporated QW structure, its transport properties could be switched by states with different curvature similar to mechanical switching with piezoelectric nanowires [158, 159]. Further, also optical modulators and electro-optic devices could be driven by membrane curvature instead (or in addition) to the electric field. We are aware of speed and robustness of electric field control, but the low frequency curvature control might be advantageous for human interaction and ambient environment [159] or nanoelectromechanical systems (NEMS) [160].

Nomenclature

α_γ	Contribution of wrinkle shape to bending rigidity during attenuation
$\boldsymbol{\Delta\kappa_{FE}}$	Change in total curvature during rolling-up of wrinkled film on flat edge
$\boldsymbol{\Delta\kappa_{WE}}$	Change in total curvature during rolling-up of wrinkled film on wrinkled edge
χ_e, χ_h	Electron and hole envelope function
Δ	Laplacian operator in two dimensions
δ, ρ	Ratio of layer thickness and plane strain Young's modulus
$\Delta\varepsilon, \bar{\varepsilon}$	Strain gradient and average strain
Δ_0	Spin-orbit splitting of valence band
γ	Attenuation parameter
$\hbar$	Reduced Planck's constant $6.582{\cdot}10^{-16}\,\mathrm{eV}\cdot\mathrm{s}$
$\kappa, \boldsymbol{\kappa}$	Curvature and curvature vector
λ, λ_0	General and equilibrium wrinkle period
ν	Poisson's ratio
Ω	Domain of the envelope function
$\overline{Y}$	Plane strain Young's modulus
σ^m	Membrane stress
$\sigma_{xx}, \sigma_{yy}, \sigma_{zz}$	Stresses in the film

ε	Strain
ε^b	Bending strain
ε^b_{QW}	Bending strain in the middle of the QW
ε^m	Membrane strain
ε_0, σ_0	Initial strain and stress - negative (compressive), positive (tensile)
ε_{const}	Constant strain
ε_{frac}	Fracture strain
ε_r	Radial strain
ε_{stre}	Wrinkle stretchability
ε_{surf}	Bending strain at film surface
ε_t	Tangential strain
ε_{vol}	Volumetric strain
$\varepsilon_{xx}, \varepsilon_{yy}, \varepsilon_{zz}$	Strain in x, y, z direction
φ	Airy stress function
ζ, ζ_0	Out-of-plane deflection (displacement)
a	Lattice constant
A', λ'	Normalized wrinkle amplitude and period
A'_{max}	Maximum normalized wrinkle amplitude before fracture
A, A_0	General and equilibrium wrinkle amplitude
a_1, a_2, a_3	Expressions to simplify notation
a_C	Conduction band hydrostatic deformation potential
a_V	Valence band hydrostatic deformation potential
B	Bandwidth of the WQW

b_V	Valence band shear deformation potential
c, c_0	General and initial local curvature
d	Film (layer) thickness
$D, \boldsymbol{D}$	Bending rigidity of the film and bending rigidity matrix
D_{12}	Bending (flexural) rigidity of the bilayer
E	Energy
e	Elementary charge $1.602{\cdot}10^{-19}$ C
E_C^0, E_C	Conduction bandedge energy of unstrained and strained material
E_g^0	Bandgap energy of unstrained material
E_V^0, E_V	Valence bandedge energy of unstrained and strained material
$E_{V,av}^0$	Average energy of 3 topmost valence bands of unstrained material
E_n	Quantized energy of state number n
$E_{e,n}, E_{h,m}$	Quantized energy of electron state n and hole state m
F	Electric field
f	Ansatz function connecting wrinkled and flat film
g, g_0	General and equilibrium global curvature
g_{WE}, g_{FE}	Global curvature of rolling-up film on wrinkled or flat edge
h, H	Etching distance
h_{cw}	Critical etching length for wrinkle formation
K	Wavevector of carriers
k, k_0	General and equilibrium wrinkle wavenumber
l	Integer number
L_x, L_y	Lateral plate dimensions

$M_0, \boldsymbol{M_0}$	Bending moment per unit width from initial strain gradient and its vector form
m_b, m_w	Effective masses of barrier and well layer
m_e, m_{hh}	Effective masses of electron and heavy hole
$M_{xx}, M_{yy}, \boldsymbol{M}$	Bending moment per unit width in x, y direction and its vector form
N	Number of tube rotations
n, m	Index of electron and hole state
N_{max}, R_{max}	Maximum number of tube rotations and corresponding bending radius of last rotation
$O_{n,m}$	Overlap integral between electron and hole states n, m
q, q_0	General and equilibrium strain relaxation parameter
R, R_0	Radius of rolled-up tube in general and equilibrium configuration
r, t	Normal and tangential coordinate
R_N	Radius of N-th tube rotation
R_{FE}	Tube radius from flat edge
R_{St}	Stoney bending radius for thick substrate
R_{Ti}	Timoshenko bending radius of bilayer
R_{WE}	Tube radius from wrinkled edge
s	Arclength of one wrinkle period
U	Elastic energy
U_0	Initial elastic energy of the bilayer film
U_b	Bending elastic energy
u_b	Bending energy density
U_s	Stretching elastic energy

u_x, u_y	In-plane displacements
U_{bent}, U_{b0}	Elastic energy of the bent film in general and equilibrium configuration
U_{bw}, U_{sw}	Bending and stretching elastic energy of the wrinkled film
U_{FE}	Change of total elastic energy for tube formed on flat edge
u_{FE}	Change of elastic energy density of wrinkled film on flat edge
U_{planar}	Elastic energy of planar relaxed film
U_{WE}	Change of total elastic energy for tube formed on wrinkled edge
$u_{WE}, \bar{u}_{WE}$	Change of elastic energy density of wrinkled film on wrinkled edge and its average over wrinkle period
U_w, U_{w0}	Total elastic energy of the wrinkled film in general and equilibrium configuration
V	Potential
$V_{e,lat}, V_{h,lat}$	Depth of the lateral potential well for electron and hole
$V_{e,ver}$	Depth of the vertical potential well for electron
x, y, z	Cartesian coordinates
Y	Young's modulus
z_b, r_b	Position of neutral plane
z_i, z_{i+1}	Position of bottom and top surface of i-th layer
z_{QW}	Distance of QW from the neutral plane of the film

List of abbreviations

AFM	Atomic force microscope
FE	Flat edge
TWE	Tube on wrinkled edge

TFE	Tube on flat edge
QW	Quantum well
TB	Tube boundary
WE	Wrinkled edge
WQW	Wrinkled quantum well
Eq	Equilibrium

Bibliography

[1] B. Bhushan, *Handbook of nanotechnology* (Springer, 2007) ISBN 9783540298557.

[2] F. Cavallo and M. G. Lagally, Soft Matter **6**, 439 (2010), ISSN 1744-683X, http://pubs.rsc.org/en/Content/ArticleLanding/2010/SM/b916582g.

[3] T. G. Leong, A. M. Zarafshar, and D. H. Gracias, Small **6**, 792 (Apr. 2010), ISSN 1613-6829, http://onlinelibrary.wiley.com/doi/10.1002/smll.200901704/abstract.

[4] B. Audoly and Y. Pomeau, *Elasticity and geometry: from hair curls to the nonlinear response of shells* (Oxford University Press, 2010).

[5] N. Bowden, S. Brittain, A. G. Evans, J. W. Hutchinson, and G. M. Whitesides, Nature **393**, 146 (May 1998), ISSN 0028-0836, http://www.nature.com/nature/journal/v393/n6681/abs/393146a0.html.

[6] O. G. Schmidt and K. Eberl, Nature **410**, 168 (Mar. 2001), ISSN 0028-0836, http://dx.doi.org/10.1038/35065525.

[7] Y. Sun, W. M. Choi, H. Jiang, Y. Y. Huang, and J. A. Rogers, Nature Nanotechnology **1**, 201 (Dec. 2006), ISSN 1748-3387.

[8] V. Y. Prinz, V. A. Seleznev, A. K. Gutakovsky, A. V. Chehovskiy, V. V. Preobrazhenskii, M. A. Putyato, and T. A. Gavrilova, Physica E: Low-dimensional Systems and Nanostructures **6**, 828 (Feb. 2000), ISSN 1386-9477, http://www.sciencedirect.com/science/article/B6VMT-3YSY07V-70/2/64d79d338fd8344816bdc8c0d38d6b2a.

[9] O. G. Schmidt, N. Schmarje, C. Deneke, C. Müller, and N. Y. Jin-Phillipp, Advanced Materials **13**, 756–759 (2001), ISSN 1521-4095, http://dx.doi.org/10.1002/1521-4095(200105)13:10<756::AID-ADMA756>3.0.CO;2-F.

[10] A. I. Fedorchenko, A. Wang, V. I. Mashanov, W. Huang, and H. H. Cheng, Applied Physics Letters **89**, 043119 (2006), http://link.aip.org/link/?APL/89/043119/1.

[11] V. Luchnikov, K. Kumar, and M. Stamm, Journal of Micromechanics and Microengineering **18**, 035041 (Mar. 2008), ISSN 0960-1317, http://iopscience.iop.org/0960-1317/18/3/035041.

[12] L. D. Landau and E. M. Lifshitz, *Theory of elasticity* (Elsevier, 1986) ISBN 9780750626330.

[13] S. R. Choi, J. W. Hutchinson, and A. G. Evans, Mechanics of Materials **31**, 431 (1999), ISSN 0167-6636, http://www.sciencedirect.com/science/article/B6TX6-48CPFV5-N/2/fc077f0e1646800e396aafcedad1639a.

[14] B. Audoly, Physical Review Letters **83**, 4124 (Nov. 1999), http://link.aps.org/doi/10.1103/PhysRevLett.83.4124.

[15] K. Bisshopp and D. Drucker, Quarterly of applied mathematics **3**, 272 (1945), ISSN 0033-569X, http://apps.isiknowledge.com/full_record.do?product=WOS&search_mode=GeneralSearch&qid=1&SID=Z1jPgF4LHDA5a8DIH7I&page=1&doc=1.

[16] G. G. Stoney, Proceedings of the Royal Society of London. Series A **82**, 172 (May 1909), http://rspa.royalsocietypublishing.org/content/82/553/172.short.

[17] L. B. Freund and S. Suresh, *Thin Film Materials: Stress, Defect Formation, and Surface Evolution* (Cambridge University Press, 2003).

[18] S. Timoshenko, Journal of the Optical Society of America **11**, 233 (1925), http://www.opticsinfobase.org/abstract.cfm?URI=josa-11-3-233.

[19] T. Zhang, X. Zhang, and Y. Zohar, Journal of Micromechanics and Microengineering **8**, 243 (Sep. 1998), ISSN 0960-1317, temp, http://iopscience.iop.org/0960-1317/8/3/011.

[20] W. Huang, H. H. Cheng, A. I. Fedorchenko, and A. Wang, Applied Physics Letters **91**, 053103 (2007), http://link.aip.org/link/?APL/91/053103/1.

[21] T. Kipp, H. Welsch, C. Strelow, C. Heyn, and D. Heitmann, Physical Review Letters **96**, 077403 (Feb. 2006), http://link.aps.org/doi/10.1103/PhysRevLett.96.077403.

[22] J. Zang, M. Huang, and F. Liu, Physical Review Letters **98**, 146102 (2007), http://link.aps.org/abstract/PRL/v98/e146102.

[23] D. Yu and F. Liu, Nano Letters **7**, 3046 (2007), http://pubs.acs.org/doi/abs/10.1021/nl071511n.

[24] T. Mora and A. Boudaoud, The European Physical Journal E **20**, 119 (Jun. 2006), ISSN 1292-8941, temp, http://www.springerlink.com/content/v446j5073h3417l0/.

[25] Y. Mei, D. J. Thurmer, F. Cavallo, S. Kiravittaya, and O. G. Schmidt, Advanced Materials **19**, 2124 (Aug. 2007), ISSN 1521-4095, temp, http://onlinelibrary.wiley.com/doi/10.1002/adma.200601622/abstract.

[26] C. Deneke, U. Zschieschang, H. Klauk, and O. G. Schmidt, Applied Physics Letters **89**, 263110 (2006), ISSN 00036951, http://link.aip.org/link/APPLAB/v89/i26/p263110/s1&Agg=doi.

[27] A. Bernardi, S. Kiravittaya, A. Rastelli, R. Songmuang, D. J. Thurmer, M. Benyoucef, and O. G. Schmidt, Applied Physics Letters **93**, 094106 (2008), ISSN 00036951, http://link.aip.org/link/APPLAB/v93/i9/p094106/s1&Agg=doi.

[28] A. A. Solovev, S. Sanchez, M. Pumera, Y. F. Mei, and O. G. Schmidt, Advanced Functional Materials **20**, 2430 (2010), ISSN 1616301X, http://onlinelibrary.wiley.com/doi/10.1002/adfm.200902376/abstract.

[29] C. C. Bof Bufon, J. D. Cojal Gonzalez, D. J. Thurmer, D. Grimm, M. Bauer, and O. G. Schmidt, Nano Letters **10**, 2506 (Jul. 2010), http://dx.doi.org/10.1021/nl1010367.

[30] E. Klokholm and B. S. Berry, Journal of The Electrochemical Society **115**, 823 (1968), http://link.aip.org/link/?JES/115/823/1.

[31] H. Windischmann, Critical Reviews in Solid State and Materials Sciences **17**, 547–596 (1992).

[32] R. Koch, Journal of Physics Condensed Matter **6**, 9519 (Nov. 1994).

[33] Y. Mei, G. Huang, A. A. Solovev, E. B. Ureña, I. Mönch, F. Ding, T. Reindl, R. K. Y. Fu, P. K. Chu, and O. G. Schmidt, Advanced Materials **20**, 4085 (Nov. 2008), ISSN 1521-4095, http://onlinelibrary.wiley.com/doi/10.1002/adma.200801589/abstract.

[34] X. Xie, L. Ju, X. Feng, Y. Sun, R. Zhou, K. Liu, S. Fan, Q. Li, and K. Jiang, Nano Letters **9**, 2565 (2009), PMID: 19499895, http://pubs.acs.org/doi/abs/10.1021/nl900677y.

[35] J. Zang and F. Liu, Applied Physics Letters **92**, 021905 (2008), ISSN 00036951, http://link.aip.org/link/APPLAB/v92/i2/p021905/s1&Agg=doi.

[36] M. Grundmann, Applied Physics Letters **83**, 2444 (2003), http://link.aip.org/link/?APL/83/2444/1.

[37] G. P. Nikishkov, Journal of Applied Physics **94**, 5333 (2003), http://link.aip.org/link/?JAP/94/5333/1.

[38] B. Krause, C. Mocuta, T. H. Metzger, C. Deneke, and O. G. Schmidt, Physical Review Letters **96**, 165502 (Apr. 2006), http://link.aps.org/doi/10.1103/PhysRevLett.96.165502.

[39] C. Deneke, C. Mueller, N. Y. Jin-Phillipp, and O. G. Schmidt, Semiconductor Science and Technology **17**, 1278 (Dec. 2002), ISSN 0268-1242, http://iopscience.iop.org/0268-1242/17/12/312.

[40] E. Sharon, B. Roman, M. Marder, G. Shin, and H. L. Swinney, Nature **419**, 579 (Oct. 2002), ISSN 0028-0836, http://dx.doi.org/10.1038/419579a.

[41] E. Sharon, B. Roman, and H. L. Swinney, Physical Review E **75**, 046211 (Apr. 2007), http://link.aps.org/doi/10.1103/PhysRevE.75.046211.

[42] H. Liang and L. Mahadevan, Proceedings of the National Academy of Science **106**, 22049 (Dec. 2009).

[43] R. Huang and Z. Suo, Journal of Applied Physics **91**, 1135 (2002), ISSN 00218979, http://link.aip.org/link/JAPIAU/v91/i3/p1135/s1&Agg=doi.

[44] C. Hsueh and P. Miranda, Journal of Materials Research **18**, 1275 (2003), http://journals.cambridge.org/action/displayAbstract?fromPage=online&aid=7985041.

[45] "Mathematica," www.wolfram.com (2010), www.wolfram.com.

[46] E. Cerda and L. Mahadevan, Physical Review Letters **90**, 074302 (2003), http://link.aps.org/abstract/PRL/v90/e074302.

[47] R. Songmuang, C. Deneke, and O. G. Schmidt, Applied Physics Letters **89**, 223109 (2006), ISSN 00036951, http://link.aip.org/link/APPLAB/v89/i22/p223109/s1&Agg=doi.

[48] C. Deneke and O. G. Schmidt, Applied Physics Letters **89**, 123121 (2006), http://link.aip.org/link/?APL/89/123121/1.

[49] L. Zhang, L. Dong, and B. J. Nelson, Applied Physics Letters **92**, 243102 (2008), ISSN 00036951, http://link.aip.org/link/APPLAB/v92/i24/p243102/s1&Agg=doi.

[50] D. J. Thurmer, C. Deneke, and O. G. Schmidt, Journal of Physics D: Applied Physics **41**, 205419 (Oct. 2008), ISSN 0022-3727, http://iopscience.iop.org/0022-3727/41/20/205419/.

[51] H. Vandeparre, M. Piñeirua, F. Brau, B. Roman, J. Bico, C. Gay, W. Bao, C. N. Lau, P. M. Reis, and P. Damman, Physical Review Letters **106**, 224301 (Jun. 2011), http://link.aps.org/doi/10.1103/PhysRevLett.106.224301.

[52] O. G. Schmidt, C. Deneke, S. Kiravittaya, R. Songmuang, H. Heidemeyer, Y. Nakamura, R. Zapf-Gottwick, C. Muller, and N. Y. Jin-Phillipp, IEEE Journal of Selected Topics in Quantum Electronics **8**, 1025 (Oct. 2002), ISSN 1077-260X.

[53] X. Li, Journal of Physics D: Applied Physics **41**, 193001 (Oct. 2008), ISSN 0022-3727, http://iopscience.iop.org/0022-3727/41/19/193001.

[54] O. G. Schmidt and N. Y. Jin-Phillipp, Applied Physics Letters **78**, 3310 (2001), http://link.aip.org/link/?APL/78/3310/1.

[55] E. J. Smith, Z. Liu, Y. Mei, and O. G. Schmidt, Nano Letters **10**, 1 (Jan. 2010), http://dx.doi.org/10.1021/nl900550j.

[56] L. M. Viculis, J. J. Mack, and R. B. Kaner, Science **299**, 1361 (Feb. 2003), http://www.sciencemag.org.

[57] A. Sidorov, D. Mudd, G. Sumanasekera, P. J. Ouseph, C. S. Jayanthi, and S. Wu, Nanotechnology **20**, 055611 (Feb. 2009), ISSN 0957-4484, 1361-6528, http://iopscience.iop.org/0957-4484/20/5/055611.

[58] Y. Chen, J. Lu, and Z. Gao, The Journal of Physical Chemistry C **111**, 1625 (Feb. 2007), http://dx.doi.org/10.1021/jp066030r.

[59] H. Pan, Y. Feng, and J. Lin, Physical Review B **72**, 085415 (2005), http://link.aps.org/doi/10.1103/PhysRevB.72.085415.

[60] S. F. Braga, V. R. Coluci, S. B. Legoas, R. Giro, D. S. G. ao, and R. H. Baughman, Nano Letters **4**, 881 (May 2004).

[61] G. Mpourmpakis, E. Tylianakis, and G. E. Froudakis, Nano Letters **7**, 1893 (Jul. 2007).

[62] I. Chun, V. Verma, V. Elarde, S. Kim, J. Zuo, J. Coleman, and X. Li, Journal of Crystal Growth **310**, 2353 (Apr. 2008), ISSN 0022-0248, http://www.sciencedirect.com/science/article/pii/S0022024807009645.

[63] J. Cho, T. James, and D. H. Gracias, Advanced Materials **22**, 2320 (Jun. 2010), ISSN 1521-4095, http://onlinelibrary.wiley.com/doi/10.1002/adma.200904410/abstract.

[64] I. S. Chun, A. Challa, B. Derickson, K. J. Hsia, and X. Li, Nano Letters **10**, 3927 (Oct. 2010), http://dx.doi.org/10.1021/nl101669u.

[65] S. Alben, B. Balakrisnan, and E. Smela, Nano Letters **11**, 2280 (Jun. 2011), http://dx.doi.org/10.1021/nl200473p.

[66] A. B. Vorob'ev and V. Y. Prinz, Semiconductor Science and Technology **17**, 614 (2002), ISSN 0268-1242, http://iopscience.iop.org/0268-1242/17/6/319.

[67] S. Golod, V. Prinz, and V. Mashanov, Thin Solid Films **489**, 169 (Oct. 2005), ISSN 0040-6090, http://www.sciencedirect.com/science/article/B6TW0-4GFCPNC-3/2/de692a6f85d0f1e5661bb591375bf444.

[68] L. Zhang, E. Deckardt, A. Weber, C. Schoenenberger, and D. Gruetzmacher, Microelectronic Engineering **83**, 1233 (Apr.), ISSN 0167-9317, http://www.sciencedirect.com/science/article/pii/S0167931706001845.

[69] C. Deneke and O. G. Schmidt, Applied Physics Letters **85**, 2914 (2004), ISSN 00036951, http://link.aip.org/link/APPLAB/v85/i14/p2914/s1&Agg=doi.

[70] N. Bassik, G. M. Stern, M. Jamal, and D. H. Gracias, Advanced Materials **20**, 4760 (Dec. 2008), ISSN 1521-4095, http://onlinelibrary.wiley.com/doi/10.1002/adma.200801759/abstract.

[71] N. Bassik, G. M. Stern, and D. H. Gracias, Applied Physics Letters **95**, 091901 (2009), ISSN 00036951, http://link.aip.org/link/APPLAB/v95/i9/p091901/s1&Agg=doi.

[72] P. Cendula, S. Kiravittaya, I. Monch, J. Schumann, and O. G. Schmidt, Nano Letters **11**, 236 (Jan. 2011), ISSN 1530-6992, PMID: 21117702, http://pubs.acs.org/doi/abs/10.1021/nl103623e.

[73] Y. Tsui and T. Clyne, Thin Solid Films **306**, 23 (Aug. 1997), ISSN 0040-6090, http://www.sciencedirect.com/science/article/B6TW0-3SP7VN7-5/2/2c8d1c89ce8b7851685c6dadc329b2b7.

[74] A. Norman, K. Seffen, and S. Guest, Proceedings of the Royal Society A: Mathematical, Physical and Engineering Science **464**, 1653 (Jul. 2008), http://rspa.royalsocietypublishing.org/content/464/2095/1653.abstract.

[75] D. Briassoulis, Computers & Structures **23**, 129 (1986), ISSN 0045-7949, http://www.sciencedirect.com/science/article/B6V28-47X765D-FX/2/a68a6eb0702d16eb2d1b007e9faeb54c.

[76] F. Macionczyk, W. Bruckner, W. Pitschke, and G. Reiss, Journal of Materials Research **13**, 2852 (1998), http://journals.cambridge.org/action/displayAbstract?fromPage=online&aid=7985339.

[77] J. C. Meyer, A. K. Geim, M. I. Katsnelson, K. S. Novoselov, T. J. Booth, and S. Roth, Nature **446**, 60 (Mar. 2007), ISSN 0028-0836, http://dx.doi.org/10.1038/nature05545.

[78] S. Scharfenberg, D. Z. Rocklin, C. Chialvo, R. L. Weaver, P. M. Goldbart, and N. Mason, Applied Physics Letters **98**, 091908 (2011), ISSN 00036951, http://link.aip.org/link/APPLAB/v98/i9/p091908/s1&Agg=doi.

[79] T. Li and Z. Zhang, Nanoscale Research Letters **5**, 169 (Oct. 2009), ISSN 1931-7573, http://www.springerlink.com/content/36531x27858n5n06/.

[80] T. Li and Z. Zhang, Journal of Physics D: Applied Physics **43**, 075303 (Feb. 2010), ISSN 0022-3727, http://iopscience.iop.org/0022-3727/43/7/075303/.

[81] Z. H. Aitken and R. Huang, Journal of Applied Physics **107**, 123531 (2010), ISSN 00218979, http://link.aip.org/link/JAPIAU/v107/i12/p123531/s1&Agg=doi.

[82] T. Li, Modelling and Simulation in Materials Science and Engineering **19**, 054005 (Jul. 2011), ISSN 0965-0393, http://iopscience.iop.org/0965-0393/19/5/054005/.

[83] M. V. Savoskin, V. N. Mochalin, A. P. Yaroshenko, N. I. Lazareva, T. E. Konstantinova, I. V. Barsukov, and I. G. Prokofiev, Carbon **45**, 2797 (Nov. 2007), ISSN 0008-6223, http://www.sciencedirect.com/science/article/pii/S0008622307004861.

[84] C. Lee, X. Wei, J. W. Kysar, and J. Hone, Science **321**, 385 (Jul. 2008), http://www.sciencemag.org/content/321/5887/385.abstract.

[85] E. Cadelano, P. L. Palla, S. Giordano, and L. Colombo, Physical Review Letters **102**, 235502 (Jun. 2009), http://link.aps.org/doi/10.1103/PhysRevLett.102.235502.

[86] R. Saito, G. Dresselhaus, M. S. Dresselhaus, *et al.*, *Physical properties of carbon nanotubes*, Vol. 3 (Imperial College Press London, 1998).

[87] A. L. Chuvilin, V. L. Kuznetsov, and A. N. Obraztsov, Carbon **47**, 3099 (Nov. 2009), ISSN 0008-6223, http://www.sciencedirect.com/science/article/pii/S0008622309004485.

[88] "COMSOL multiphysics," www.comsol.com (2010), www.comsol.com.

[89] R. K. Annabattula, J. M. Veenstra, Y. F. Mei, O. G. Schmidt, and P. R. Onck, Physical Review B **81**, 224114 (Jun. 2010), http://link.aps.org/doi/10.1103/PhysRevB.81.224114.

[90] C. Deneke, W. Sigle, U. Eigenthaler, P. A. van Aken, G. Schutz, and O. G. Schmidt, Applied Physics Letters **90**, 263107 (2007), http://link.aip.org/link/?APL/90/263107/1.

[91] V. A. Bolanos Quinones, G. Huang, J. D. Plumhof, S. Kiravittaya, A. Rastelli, Y. Mei, and O. G. Schmidt, Optics Letters **34**, 2345 (2009), http://ol.osa.org/abstract.cfm?URI=ol-34-15-2345.

[92] G. S. Huang, S. Kiravittaya, V. A. Bolanos Quinones, F. Ding, M. Benyoucef, A. Rastelli, Y. F. Mei, and O. G. Schmidt, Applied Physics Letters **94**, 141901 (2009), ISSN 00036951, http://link.aip.org/link/APPLAB/v94/i14/p141901/s1&Agg=doi.

[93] J. Genzer and J. Groenewold, Soft Matter **2**, 310 (2006), ISSN 1744-683X, http://pubs.rsc.org/en/Content/ArticleLanding/2006/SM/b516741h.

[94] A. Schweikart and A. Fery, Microchimica Acta **165**, 249 (Apr. 2009), ISSN 0026-3672, http://www.springerlink.com/content/9u0252x33w415623/.

[95] Y. Mei, S. Kiravittaya, S. Harazim, and O. G. Schmidt, Materials Science and Engineering: R: Reports **70**, 209 (Nov. 2010), ISSN 0927-796X, http://www.sciencedirect.com/science/article/B6TXH-50DNKPP-2/2/74e1bec2d150f6d831195dea681d9946.

[96] W. Bao, F. Miao, Z. Chen, H. Zhang, W. Jang, C. Dames, and C. N. Lau, Nature Nanotechnology **4**, 562 (Sep. 2009), ISSN 1748-3395, PMID: 19734927, http://www.ncbi.nlm.nih.gov/pubmed/19734927.

[97] H. Vandeparre, J. Léopoldès, C. Poulard, S. Desprez, G. Derue, C. Gay, and P. Damman, Physical Review Letters **99**, 188302 (Oct. 2007), http://link.aps.org/doi/10.1103/PhysRevLett.99.188302.

[98] W. M. Choi, J. Song, D. Khang, H. Jiang, Y. Y. Huang, and J. A. Rogers, Nano Letters **7**, 1655 (Jun. 2007), http://dx.doi.org/10.1021/nl0706244.

[99] T. Maruyama, H. Hirakata, A. Yonezu, and K. Minoshima, Applied Physics Letters **98**, 041908 (2011), ISSN 00036951, http://link.aip.org/link/APPLAB/v98/i4/p041908/s1&Agg=doi.

[100] D. C. O'Shea, *Diffractive optics: design, fabrication, and test*, Tutorial texts in optical engineering (SPIE Press, 2004) ISBN 9780819451712, http://books.google.com/books?id=NFrG-zFrIDYC.

[101] P. Cendula, "Supporting video files," http://nanohub.org/resources/11764, http://nanohub.org/resources/11764.

[102] J. S. Randhawa, T. G. Leong, N. Bassik, B. R. Benson, M. T. Jochmans, and D. H. Gracias, Journal of the American Chemical Society **130**, 17238 (Dec. 2008), http://dx.doi.org/10.1021/ja806961p.

[103] J. S. Randhawa, M. D. Keung, P. Tyagi, and D. H. Gracias, Advanced Materials **22**, 407 (Jan. 2010), ISSN 1521-4095, temp, http://onlinelibrary.wiley.com/doi/10.1002/adma.200902337/abstract.

[104] T. G. Leong, B. R. Benson, E. K. Call, and D. H. Gracias, Small **4**, 1605 (Oct. 2008), ISSN 1613-6829, http://onlinelibrary.wiley.com/doi/10.1002/smll.200800280/abstract.

[105] E. W. H. Jager, E. Smela, and O. Inganäs, Science **290**, 1540 (Nov. 2000), http://www.sciencemag.org/content/290/5496/1540.abstract.

[106] E. Smela, Advanced Materials **15**, 481 (Mar. 2003), ISSN 1521-4095, http://onlinelibrary.wiley.com/doi/10.1002/adma.200390113/abstract.

[107] Y. Yu, M. Nakano, and T. Ikeda, Nature **425**, 145 (2003), ISSN 0028-0836, http://dx.doi.org/10.1038/425145a.

[108] Y. Yu and T. Ikeda, Macromolecular Chemistry and Physics **206**, 1705 (Sep. 2005), ISSN 1521-3935, temp, http://onlinelibrary.wiley.com/doi/10.1002/macp.200500318/abstract.

[109] D. Xia, Q. Xue, J. Xie, H. Chen, C. Lv, F. Besenbacher, and M. Dong, Small **6**, 2010 (Sep. 2010), ISSN 1613-6829, http://onlinelibrary.wiley.com/doi/10.1002/smll.201000646/abstract.

[110] C. G. Van de Walle, Physical Review B **39**, 1871 (Jan. 1989), http://link.aps.org/doi/10.1103/PhysRevB.39.1871.

[111] M. Grundmann, *The Physics of Semiconductors* (Springer, 2006) ISBN 9783642138836.

[112] Y. Sun, S. Thompson, and T. Nishida, *Strain Effect in Semiconductors: Theory and Device Applications* (Springer, 2009) ISBN 9781441905512.

[113] E. H. Li, Physica E: Low-dimensional Systems and Nanostructures **5**, 215 (Mar. 2000), ISSN 1386-9477, temp, http://www.sciencedirect.com/science/article/pii/S1386947799002623.

[114] S. L. Chuang, *Physics of Optoelectronic Devices* (Wiley-Interscience, 1995) ISBN 0471109398.

[115] J. H. Davies, *The physics of low-dimensional semiconductors: an introduction* (Cambridge University Press, 1998) ISBN 9780521484916.

[116] Y. Mei, S. Kiravittaya, M. Benyoucef, D. J. Thurmer, T. Zander, C. Deneke, F. Cavallo, A. Rastelli, and O. G. Schmidt, Nano Letters **7**, 1676 (Jun. 2007), http://dx.doi.org/10.1021/nl070653e.

[117] W. S. Wong and A. Salleo, *Flexible electronics: materials and applications* (Springer, 2009).

[118] D. Kim and J. A. Rogers, Advanced Materials **20**, 4887 (Dec. 2008), ISSN 1521-4095, http://onlinelibrary.wiley.com/doi/10.1002/adma.200801788/abstract.

[119] J. A. Rogers, T. Someya, and Y. Huang, Science **327**, 1603 (2010), http://www.sciencemag.org/cgi/content/abstract/327/5973/1603.

[120] D. Kim, J. Xiao, J. Song, Y. Huang, and J. A. Rogers, Advanced Materials **22**, 2108 (Jan. 2010), ISSN 09359648, http://onlinelibrary.wiley.com/doi/10.1002/adma.200902927/abstract.

[121] J. A. Rogers, M. G. Lagally, and R. G. Nuzzo, Nature **477**, 45 (2011), ISSN 0028-0836, http://dx.doi.org/10.1038/nature10381.

[122] D. Khang, H. Jiang, Y. Huang, and J. A. Rogers, Science **311**, 208 (Jan. 2006), http://www.sciencemag.org/content/311/5758/208.abstract.

[123] X. Lu and Y. Xia, Nature Nanotechnology **1**, 163 (Dec. 2006), ISSN 1748-3395, PMID: 18654175, http://www.ncbi.nlm.nih.gov/pubmed/18654175.

[124] Y. Sun, V. Kumar, I. Adesida, and J. A. Rogers, Advanced Materials **18**, 2857 (Nov. 2006), ISSN 1521-4095, http://onlinelibrary.wiley.com/doi/10.1002/adma.200600646/abstract.

[125] J. Lee, J. Wu, M. Shi, J. Yoon, S. Park, M. Li, Z. Liu, Y. Huang, and J. A. Rogers, Advanced Materials **23**, 986 (Feb. 2011), ISSN 1521-4095, http://onlinelibrary.wiley.com/doi/10.1002/adma.201003961/abstract.

[126] S. Park, Y. Xiong, R. Kim, P. Elvikis, M. Meitl, D. Kim, J. Wu, J. Yoon, C. Yu, Z. Liu, Y. Huang, K. chih Hwang, P. Ferreira, X. Li, K. Choquette, and J. A. Rogers, Science **325**, 977 (2009), http://www.sciencemag.org/cgi/content/abstract/325/5943/977.

[127] S. Park, A. Le, J. Wu, Y. Huang, X. Li, and J. A. Rogers, Advanced Materials **22**, 3062 (May 2010), ISSN 09359648, http://onlinelibrary.wiley.com/doi/10.1002/adma.201000591/abstract;jsessionid=2A693BB72B1182E1D1BF4F018F6A1E0A.d01t01.

[128] M. Grundmann, J. Christen, M. Joschko, O. Stier, D. Bimberg, and E. Kapon, Semiconductor Science and Technology **9**, 1939 (Nov. 1994), ISSN 0268-1242, http://iopscience.iop.org/0268-1242/9/11S/014.

[129] S. Khatsevich, Journal of Applied Physics **95**, 1832 (2004), ISSN 00218979, http://link.aip.org/link/?JAP/95/1832/1&Agg=doi.

[130] M. Remeika, J. C. Graves, A. T. Hammack, A. D. Meyertholen, M. M. Fogler, L. V. Butov, M. Hanson, and A. C. Gossard, Physical Review Letters **102**, 186803 (May 2009), http://link.aps.org/doi/10.1103/PhysRevLett.102.186803.

[131] K. Kubota, P. O. Vaccaro, N. Ohtani, Y. Hirose, M. Hosoda, and T. Aida, Physica E: Low-dimensional Systems and Nanostructures **13**, 313 (Mar. 2002), ISSN 1386-9477, http://www.sciencedirect.com/science/article/B6VMT-44Y0YTW-2/2/68e5d658f1be464ebea89326ec284c9c.

[132] M. Hosoda, Y. Kishimoto, M. Sato, S. Nashima, K. Kubota, S. Saravanan, P. O. Vaccaro, T. Aida, and N. Ohtani, Applied Physics Letters **83**,

1017 (2003), ISSN 00036951, http://link.aip.org/link/APPLAB/v83/i5/p1017/s1&Agg=doi.

[133] C. Deneke, A. Malachias, S. Kiravittaya, M. Benyoucef, T. H. Metzger, and O. G. Schmidt, Applied Physics Letters **96**, 143101 (2010), http://link.aip.org/link/?APL/96/143101/1.

[134] S. R. Parihar, S. A. Lyon, M. Santos, and M. Shayegan, Applied Physics Letters **55**, 2417 (1989), ISSN 00036951, http://link.aip.org/link/APPLAB/v55/i23/p2417/s1&Agg=doi.

[135] H. C. Liu, J. Li, J. R. Thompson, Z. R. Wasilewski, M. Buchanan, and J. G. Simmons, IEEE Electron Device Letters **14**, 566 (Dec. 1993), ISSN 0741-3106.

[136] H. Schneider and H. C. Liu, *Quantum well infrared photodetectors: physics and applications* (Springer, 2007) ISBN 9783540363231.

[137] K. Kash, B. P. V. der Gaag, D. D. Mahoney, A. S. Gozdz, L. T. Florez, J. P. Harbison, and M. D. Sturge, Physical Review Letters **67**, 1326 (1991), http://link.aps.org/doi/10.1103/PhysRevLett.67.1326.

[138] M. Sopanen, H. Lipsanen, and J. Ahopelto, Applied Physics Letters **66**, 2364 (1995), ISSN 00036951, http://link.aip.org/link/APPLAB/v66/i18/p2364/s1&Agg=doi.

[139] C. F. Wang, A. Badolato, I. Wilson-Rae, P. M. Petroff, E. Hu, J. Urayama, and A. Imamoglu, Applied Physics Letters **85**, 3423 (2004), ISSN 00036951, http://link.aip.org/link/APPLAB/v85/i16/p3423/s1&Agg=doi.

[140] W. R. Childs, M. J. Motala, K. J. Lee, and R. G. Nuzzo, Langmuir **21**, 10096 (Oct. 2005), http://dx.doi.org/10.1021/la050011b.

[141] H. Jiang, Y. Sun, J. A. Rogers, and Y. Huang, Applied Physics Letters **90**, 133119 (2007), ISSN 00036951, http://link.aip.org/link/APPLAB/v90/i13/p133119/s1&Agg=doi.

[142] J. Weertman, *Dislocation based fracture mechanics* (World Scientific, 1996) ISBN 9789810226206.

[143] D. Khang, J. A. Rogers, and H. H. Lee, Advanced Functional Materials **19**, 1526 (May 2009), ISSN 1616-3028, http://onlinelibrary.wiley.com/doi/10.1002/adfm.200801065/abstract.

[144] K. Kash, R. Bhat, D. D. Mahoney, P. S. D. Lin, A. Scherer, J. M. Worlock, B. P. Van der Gaag, M. Koza, and P. Grabbe, Applied Physics Letters **55**, 681 (1989), ISSN 00036951, http://link.aip.org/link/APPLAB/v55/i7/p681/s1&Agg=doi.

[145] R. C. T. da Costa, Physical Review A **23**, 1982 (Apr. 1981), http://link.aps.org/doi/10.1103/PhysRevA.23.1982.

[146] S. Ono and H. Shima, Physical Review B **79**, 235407 (Jun. 2009), http://link.aps.org/doi/10.1103/PhysRevB.79.235407.

[147] C. Ortix and J. van den Brink, Physical Review B **81**, 165419 (Apr. 2010), http://link.aps.org/doi/10.1103/PhysRevB.81.165419.

[148] C. Ortix, S. Kiravittaya, O. G. Schmidt, and J. van den Brink, Physical Review B **84**, 045438 (Jul. 2011), http://link.aps.org/doi/10.1103/PhysRevB.84.045438.

[149] T. L. Li and K. J. Kuhn, Journal of Computational Physics **110**, 292 (Feb. 1994), ISSN 0021-9991, http://www.sciencedirect.com/science/article/B6WHY-45PTPT7-9/2/0941f27385acfdcdbf5a123063ae5606.

[150] E. P. O'Reilly, Semiconductor Science and Technology **4**, 121 (Mar. 1989), ISSN 0268-1242, http://iopscience.iop.org/0268-1242/4/3/001.

[151] S. Wang and P. Pirouz, Acta Materialia **55**, 5500 (Sep. 2007), ISSN 1359-6454, http://www.sciencedirect.com/science/article/B6TW8-4P9K99D-3/2/2990ea91386d385036604ebe4649b897.

[152] R. Nowak, M. Pessa, M. Suganuma, M. Leszczynski, I. Grzegory, S. Porowski, and F. Yoshida, Applied Physics Letters **75**, 2070 (1999), ISSN 00036951, http://link.aip.org/link/APPLAB/v75/i14/p2070/s1&Agg=doi.

[153] I. Yonenaga and K. Motoki, Journal of Applied Physics **90**, 6539 (2001), ISSN 00218979, http://link.aip.org/link/JAPIAU/v90/i12/p6539/s1&Agg=doi.

[154] M. Abramowitz and I. A. Stegun, *Handbook of mathematical functions with formulas, graphs, and mathematical tables* (Courier Dover Publications, 1964) ISBN 9780486612720.

[155] Y. Kuo, Y. K. Lee, Y. Ge, S. Ren, J. E. Roth, T. I. Kamins, D. A. B. Miller, and J. S. Harris, Nature **437**, 1334 (Oct. 2005), ISSN 0028-0836, http://dx.doi.org/10.1038/nature04204.

[156] M. Huang, F. Cavallo, F. Liu, and M. G. Lagally, Nanoscale **3**, 96 (2011), ISSN 2040-3364, http://pubs.rsc.org/en/Content/ArticleLanding/2011/NR/C0NR00648C.

[157] R. L. Badzey and P. Mohanty, Nature **437**, 995 (Oct. 2005), ISSN 0028-0836, http://dx.doi.org/10.1038/nature04124.

[158] J. Zhou, P. Fei, Y. Gu, W. Mai, Y. Gao, R. Yang, G. Bao, and Z. L. Wang, Nano Letters **8**, 3973 (Nov. 2008), http://dx.doi.org/10.1021/nl802497e.

[159] W. Wu, Y. Wei, and Z. L. Wang, Advanced Materials **22**, 4711 (Nov. 2010), ISSN 1521-4095, http://onlinelibrary.wiley.com/doi/10.1002/adma.201001925/abstract.

[160] B. Lassagne, Y. Tarakanov, J. Kinaret, D. Garcia-Sanchez, and A. Bachtold, Science **325**, 1107 (2009), http://www.sciencemag.org/content/325/5944/1107.abstract.

Acknowledgements

I am grateful to my supervisors, Prof. Oliver G. Schmidt and Prof. Vaclav Holy, for giving me the opportunity to work on exciting topics, encouragement and motivation, guidance in scientific progress and teaching me what to look for in research work. Many thanks also to Dr. S. Kiravittaya for being my invaluable day-to-day advisor, for his patience, letting me to work very independent and treating me as a colleague.

I'm thankful to B. Eichler for AFM images, J. Schumann for magnetron sputtering, I. Monch for multiple exposure lithography, E. Coric and S. Baunack for SEM images, J. Gabel for initial rolling experiments, U. Nitzsche for Mathematica support, J. Hayton for thesis writing tips.

A. D. Norman, D. Bourne, E. J. Smith, D. J. Thurmer, J. D. A. Espinoza, D. Grimm, C. C. Bof Bufon, V. Bolanos, E. B. Urena, Ch. Deneke, A. Malachias and Y. F. Mei, M. Bendova, B. Schmidt, F. Cavallo, R. Costescu, A. Rastelli, K.A. Seffen, V. Krapek, V. M. Fomin, R. Rezaev, C. Ortix, B. Audoly, A. I. Fedorchenko, J. W. Hutchinson : thank you for illuminating discussions and help!

Thanks to all members of Institute for Integrative Nanosciences in Dresden and Department of Condensed Matter Physics in Prague for support and nice working environment.

This work was supported by the Volkswagen Foundation (I/84 072), BMBF (03N8711), and the U.S. Air Force Office of Scientific Research MURI program under Grant FA9550-09-1-0550.

Ďakujem mojim rodičom za stálu podporu pri mojej práci a Janke, že ma ľúbi.

Publications

First-author publications

1. P. Cendula, S. Kiravittaya, and O. G. Schmidt, "Electronic and optical properties of quantum wells embedded in wrinkled nanomembranes", submitted to Journal of Applied Physics (2011).

2. P. Cendula, S. Kiravittaya, I. Monch, J. Schumann, and O. G. Schmidt, "Directional Roll-up of Nanomembranes Mediated by Wrinkling", Nano Lett. 11, 236 (2011).

3. P. Cendula, S. Kiravittaya, Y. Mei, Ch. Deneke and O.G. Schmidt, "Bending and wrinkling as competing relaxation pathways for strained free-hanging films", Phys. Rev. B 79, 085429 (2009).

Co-authored publications

1. Ch. Deneke, E. Wild, K. Boldyreva, S. Baunack, P. Cendula, I. Mönch, M. Simon, A. Malachias, K. Dörr and O. G. Schmidt, "Rolled-up tubes and cantilevers from magnetic $SrRuO_3$-$Pr_{0.7}Ca_{0.3}MnO_3$ films", accepted in Nanoscale Research Letters (2011).

Conference proceedings

1. P. Cendula, S. Kiravittaya, J. Gabel and O. G. Schmidt, "Control of Rolling Direction for Released Strained Wrinkled Nanomembrane", COMSOL Conference 2009 Milan.

2. S. Kiravittaya, P. Cendula, A. Rastelli and O. G. Schmidt, "Effect of local deformation on the emission energy of quantum dots in a flexible tube", COMSOL

Conference 2008 Hannover.